

# **Field Line Resonance in Two and a Half Dimensions**

**DRAFT VERSION CREATED ON APRIL 7, 2016**

© Charles A. McEachern 2016



The text of this work is licensed under a Creative Commons Attribution-ShareAlike 4.0 International license.

# <sup>5</sup> Acknowledgements

<sup>6</sup> Acknowledgement placeholder.

# <sup>7</sup> Dedication

<sup>8</sup> Dedication placeholder.

**Abstract**

<sup>10</sup> Abstract placeholder.

# **Contents**

<sup>11</sup>	<b>Acknowledgements</b>	i
<sup>13</sup>	<b>Dedication</b>	ii
<sup>14</sup>	<b>Abstract</b>	iii
<sup>15</sup>	<b>List of Tables</b>	vii
<sup>16</sup>	<b>List of Figures</b>	viii
<sup>17</sup>	<b>1 Introduction</b>	1
<sup>18</sup>	1.1 Structure of the Present Work . . . . .	2
<sup>19</sup>	<b>2 The Near-Earth Environment</b>	4
<sup>20</sup>	2.1 The Outer Magnetosphere . . . . .	4
<sup>21</sup>	2.2 The Inner Magnetosphere . . . . .	6
<sup>22</sup>	2.3 The Ionosphere . . . . .	8
<sup>23</sup>	2.4 Geomagnetic Storms and Substorms . . . . .	9
<sup>24</sup>	<b>3 Field Line Resonance</b>	11
<sup>25</sup>	3.1 Harmonic Structure . . . . .	14
<sup>26</sup>	3.2 Azimuthal Modenumber . . . . .	17
<sup>27</sup>	3.3 Poloidal and Toroidal Polarizations . . . . .	18
<sup>28</sup>	3.4 Giant Pulsations . . . . .	20
<sup>29</sup>	3.5 Motivations for the Present Work . . . . .	21

30	<b>4 Waves in Cold Resistive Plasma</b>	<b>24</b>
31	4.1 Guided Propagation . . . . .	26
32	4.2 Compressional Propagation . . . . .	27
33	4.3 High Altitude Limit . . . . .	29
34	4.4 Implications to the Present Work . . . . .	30
35	<b>5 “Tuna Half” Dimensional Model</b>	<b>32</b>
36	5.1 Coordinate System . . . . .	33
37	5.2 Physical Parameter Profiles . . . . .	37
38	5.3 Driving . . . . .	40
39	5.4 Maxwell’s Equations . . . . .	43
40	5.5 Boundary Conditions . . . . .	47
41	<b>6 Electron Inertial Effects</b>	<b>52</b>
42	6.1 The Boris Factor . . . . .	53
43	6.2 Parallel Currents and Electric Fields . . . . .	55
44	6.3 Inertial Length Scales . . . . .	61
45	6.4 Discussion . . . . .	62
46	<b>7 Numerical Results</b>	<b>64</b>
47	7.1 Modenumber and Compression . . . . .	64
48	7.2 Resonance and Rotation on the Dayside . . . . .	70
49	7.3 Resonance and Rotation on the Nightside . . . . .	77
50	7.4 Ground Signatures and Giant Pulsations . . . . .	82
51	7.5 Discussion . . . . .	86
52	<b>8 Observations</b>	<b>88</b>
53	8.1 Sampling Bias and Event Selection . . . . .	89
54	8.2 Rate of Pc4 Events . . . . .	92
55	8.3 Rate of Pc4 Events by Amplitude . . . . .	95
56	8.4 Rate of Pc4 Events by Frequency . . . . .	98
57	8.5 Rate of Pc4 Events by Phase . . . . .	99
58	8.6 Rate of Pc4 Events by Spectral Width . . . . .	102

59	8.7 Discussion . . . . .	103
60	<b>9 Conclusion</b>	<b>104</b>
61	9.1 Summary of Results . . . . .	104
62	9.2 Future Work . . . . .	104
63	<b>References</b>	<b>106</b>

# <sup>64</sup> List of Tables

<sup>65</sup>	3.1 IAGA Magnetic Pulsation Frequency Bands . . . . .	12
<sup>66</sup>	5.1 Typical Parameters for the Tuna Density Profile . . . . .	38
<sup>67</sup>	5.2 Integrated Atmospheric Conductivity . . . . .	48

# List of Figures

69	2.1	Outer Magnetosphere Cutaway . . . . .	5
70	2.2	Inner Magnetosphere Cutaway . . . . .	7
71	3.1	Alfvén Bounce Frequencies . . . . .	13
72	3.2	First and Second Harmonic Resonances . . . . .	15
73	3.3	Large and Small Azimuthal Modenumbers . . . . .	17
74	3.4	Poloidal Mode Structure . . . . .	19
75	3.5	Toroidal Mode Structure . . . . .	20
76	4.1	Compressional Alfvén Wave Cutoff Frequencies . . . . .	31
77	5.1	Nonorthogonal Dipole Grid . . . . .	37
78	5.2	Alfvén Speed Profiles . . . . .	39
79	5.3	Ionospheric Conductivity Profiles . . . . .	40
80	5.4	Decreasing Penetration with Increasing Modenumber . . . . .	42
81	5.5	Sym-H for June 2013 Storm . . . . .	43
82	6.1	Plasma Frequency Profile . . . . .	54
83	6.2	Electric Field Snapshots . . . . .	56
84	6.3	Current and Poynting Flux at 100 km . . . . .	57
85	6.4	Current and Poynting Flux at 1000 km . . . . .	59
86	6.5	Power Density at the Ionosphere . . . . .	60
87	6.6	Parallel Electric Fields by Perpendicular Grid Resolution . . . . .	62
88	7.1	Magnetic Field Snapshots from a Small- $m$ Run . . . . .	67
89	7.2	Magnetic Field Snapshots from a Large- $m$ Run . . . . .	68
90	7.3	Compressional Coupling to the Poloidal Mode . . . . .	69
91	7.4	Dayside Poloidal and Toroidal Energy . . . . .	74

92	7.5 Dayside Poloidal Energy Distribution . . . . .	75
93	7.6 Dayside Toroidal Energy Distribution . . . . .	76
94	7.7 Nightside Poloidal and Toroidal Energy . . . . .	78
95	7.8 Nightside Poloidal Energy Distribution . . . . .	79
96	7.9 Nightside Toroidal Energy Distribution . . . . .	80
97	7.10 Dayside Ground Magnetic Fields . . . . .	84
98	7.11 Nightside Ground Magnetic Fields . . . . .	85
99	8.1 Distribution of Usable Van Allen Probe Data . . . . .	91
100	8.2 Observation Rate of Pc4 Events . . . . .	93
101	8.3 Observation Rate of Pc4 Events by Mode . . . . .	95
102	8.4 TEST FIGURE . . . . .	96
103	8.5 TEST FIGURE . . . . .	97
104	8.6 TEST FIGURE . . . . .	98
105	8.7 TEST FIGURE . . . . .	99
106	8.8 TEST FIGURE . . . . .	100
107	8.9 TEST FIGURE . . . . .	101
108	8.10 TEST FIGURE . . . . .	102
109	8.11 TEST FIGURE . . . . .	103

<sub>110</sub> **Chapter 1**

<sub>111</sub> **Introduction**

<sub>112</sub> 1859 was a pivotal year in human history. The United States moved steadily toward  
<sub>113</sub> the American Civil War, which would abolish slavery and consolidate the power of  
<sub>114</sub> the federal government. A slew of conflicts in Southern Europe, such as the Austro-  
<sub>115</sub> Sardinian War, set the stage for the unification of Italy. The Taiping Civil War — one  
<sub>116</sub> of the bloodiest conflicts of all time — is considered by many to mark the beginning  
<sub>117</sub> of modern Chinese history. *Origin of Species* was published. The first transatlantic  
<sub>118</sub> telegraph cable was laid.

<sub>119</sub> Meanwhile, ambivalent to humanity, the Sun belched an intense burst of charged parti-  
<sub>120</sub> cles and magnetic energy directly at Earth. The resulting geomagnetic storm<sup>1</sup> caused  
<sub>121</sub> telegraph systems to fail across the Western hemisphere, electrocuting operators and  
<sub>122</sub> starting fires[35, 96]. Displays of the northern lights were visible as far south as Cuba.

<sub>123</sub> The Solar Storm of 1859 was perhaps the most powerful in recorded history, but by no  
<sub>124</sub> means was it a one-time event. The Sun discharges hundreds of coronal mass ejections  
<sub>125</sub> (CMEs) per year, of all sizes, in all directions. In fact, a comparably large CME narrowly  
<sub>126</sub> missed Earth in 2012[72]. Had it not, it's estimated it would have caused widespread,  
<sub>127</sub> long-term electrical outages, with a damage toll on the order of  $10^{12}$  dollars[66].

---

<sup>1</sup>The Solar Storm of 1859 is also called the Carrington Event, after English astronomer Richard Carrington. He drew a connection between the storm's geomagnetic activity and the sunspots he had observed the day before.

128 The Sun’s extreme — and temperamental — effect on Earth’s magnetic environment  
129 makes a compelling case for the ongoing study of space weather. Such research has  
130 evolved over the past century from sunspot counts and compass readings to multi-  
131 satellite missions and supercomputer simulations. Modern methods have dramatically  
132 increased humanity’s understanding of the relationship between the Sun and the Earth;  
133 however, significant uncertainty continues to surround geomagnetic storms, substorms,  
134 and the various energy transport mechanisms that make them up.

135 The present work focuses in particular on the phenomenon of field line resonance: Alfvén  
136 waves bouncing between the northern and southern hemispheres. Such waves play an  
137 important part in the energization of magnetospheric particles, the transport of energy  
138 from high to low altitude, and the driving of currents at the top of the atmosphere.

139 **TODO:** More is needed before we can jump into a description of the present work.  
140 Introduce what we’re working on a bit ore specifically. Talk about how space is a  
141 laboratory that teaches us about plasma in a way that’s relevant to both astrophysics  
142 and fusion reactors, which are hard to measure. Fishbone instability.

## 143 1.1 Structure of the Present Work

144 Chapter 2 surveys the near-Earth environment. Prominent features of the magneto-  
145 sphere are defined. The response of the magnetosphere to transient solar wind events  
146 is summarized.

147 Chapter 3 introduces the field line resonance phenomenon, in terms of both the under-  
148 lying physics and notable work on the topic. Jargon is introduced to clarify important  
149 elements of wave structure. Several open questions about field line resonances (FLRs)  
150 are offered as motivations for the present work.

151 Chapter 4 lays the groundwork for a numerical model by exploring the fundamental  
152 equations of waves in a cold, resistive plasma — such as Earth’s magnetosphere. Char-  
153 acteristic scales are gleaned from the resulting dispersion relations.

- 154 Chapter 5 presents Tuna, a new two and a half dimensional simulation designed specif-  
155 ically for the realistic modeling of FLRs. Tuna’s non-orthogonal geometry, height-  
156 resolved ionosphere, novel driving mechanism, and coupling to the atmosphere are ex-  
157 plained.
- 158 Chapter 6 considers the addition of electron inertial effects to Tuna, touches on what  
159 can be learned from them, and shows that they incur an unreasonable computational  
160 cost. (Electron inertia is neglected in the results presented in other chapters.)
- 161 Chapter 7 describes the core numerical results of the work, unifying several of the  
162 questions posed in Chapter 3. Significant depth is added to past work on finite poloidal  
163 lifetimes[64, 78]. Interplay between poloidal-toroidal coupling, shear-compressional cou-  
164 pling, and Joule dissipation is considered from several angles.
- 165 Chapter 8 puts the numerical results in physical context through the analysis of data  
166 from the Van Allen Probes mission. FLR occurrence rates are considered in terms of  
167 location, mode structure, and polarization – parameters which have been only partially  
168 addressed by other recent FLR surveys[17, 70].
- 169 Chapter 9 briefly summarizes the results shown in the above chapters — the code  
170 development, analysis of numerical results, and satellite observation — and suggests  
171 further directions.

<sup>172</sup> **Chapter 2**

<sup>173</sup> **The Near-Earth Environment**

<sup>174</sup> From Earth’s surface to a height of a hundred kilometers or so, the atmosphere is a  
<sup>175</sup> well-behaved fluid: a collisional ensemble of neutral atoms. Higher up, its behavior  
<sup>176</sup> changes dramatically. As altitude increases, solar ultraviolet radiation becomes more  
<sup>177</sup> intense, which ionizes atmospheric atoms. Density also decreases, slowing collisional  
<sup>178</sup> recombination. Whereas the neutral atmosphere is held against Earth’s surface by  
<sup>179</sup> gravity, the motion of charged particles is dominated by Earth’s geomagnetic field, as  
<sup>180</sup> well as the electromagnetic disturbances created as that field is hammered by the solar  
<sup>181</sup> wind.

<sup>182</sup> The present section outlines the structure of the magnetosphere; that is, the region of  
<sup>183</sup> space governed primarily by Earth’s magnetic field. Particular emphasis is placed on  
<sup>184</sup> structures which relate closely to field line resonance.

<sup>185</sup> **2.1 The Outer Magnetosphere**

<sup>186</sup> Plasma behavior within Earth’s magnetosphere is ultimately driven by the solar wind: a  
<sup>187</sup> hot ( $\sim 100$  eV), fast-moving ( $\sim 100$  km/s) plasma threaded by the interplanetary magnetic  
<sup>188</sup> field ( $\sim 1$  nT)<sup>1</sup>. The density of the solar wind is on the order of  $10^6$  /cm<sup>3</sup>; in a laboratory

---

<sup>1</sup>Listed values correspond to the solar wind at Earth’s orbit.

<sup>189</sup> setting, this would constitute an ultra-high vacuum (atmospheric density at sea level is  
<sup>190</sup>  $\sim 10^{19} / \text{cm}^3$ ), but compared to much of the magnetopause it's quite dense.



Figure 2.1: TODO: The outer magnetosphere...

<sup>191</sup> The magnetosphere's outer boundary represents a balance between the solar wind dy-  
<sup>192</sup> namic pressure and the magnetic pressure of Earth's dipole field. On the dayside, the  
<sup>193</sup> dipole is compressed, pushing this boundary to within about  $10 R_E$  of Earth<sup>2</sup>. The  
<sup>194</sup> nightside magnetosphere is stretched into a long tail which may exceed  $50 R_E$  in width  
<sup>195</sup> and  $100 R_E$  in length.

<sup>196</sup> When the interplanetary magnetic field opposes the geomagnetic field at the nose of  
<sup>197</sup> the magnetosphere, magnetic reconnection occurs. Closed magnetospheric field lines  
<sup>198</sup> "break," opening up to the interplanetary magnetic field<sup>3</sup>. They then move tailward

<sup>2</sup>Distances in the magnetosphere are typically measured in units of Earth radii:  $1 R_E \equiv 6378 \text{ km}$ .

<sup>3</sup>Closed field lines connect at both ends to the magnetic dynamo at Earth's core. Open field lines meet Earth at only one end; the other connects to the interplanetary magnetic field. The distinction is important because charged particle motion is guided by magnetic field lines, as discussed in Chapter 3.

199 across the poles, dragging their frozen-in plasma with them<sup>4</sup>. Reconnection in the tail  
200 allows magnetic field lines to convect back to the day side, across the flanks. This  
201 process is called the Dungey cycle[22].

202 Viewed from the north, the Dungey cycle involves a clockwise flow of flux and plasma on  
203 the dusk side and a counterclockwise flow on the dawn side. The motion is accompanied  
204 by a convection electric field, per Ohm's law<sup>5</sup>.

205 **TODO:** Jets from magnetic reconnection... release of magnetic tension!

206 Consistent with Ampère's law, the interplanetary magnetic field is separated from the  
207 magnetosphere by a current sheet: the magnetopause. On the dayside, the magne-  
208 topause current flows duskward; on the nightside, it flows downward around the mag-  
209 netail.

210 Plasma within the tail is cool ( $\sim 100 \text{ eV}$ ) and rarefied ( $\sim 10^{-2} / \text{cm}^3$ ). Earth's dipole is  
211 significantly deformed in the magnetotail; field lines in the northern lobe of the tail  
212 points more or less Earthward, and vice versa. The two lobes are divided by the plasma  
213 sheet, which is comparably hot ( $\sim 10^3 \text{ eV}$ ) and dense ( $\sim 1 / \text{cm}^3$ ). The plasma sheet  
214 carries a duskward current which connects to the magnetopause current.

## 215 2.2 The Inner Magnetosphere

216 Within about **TODO:**  $L \sim 10$  (where  $L$  is the McIlwain parameter<sup>6</sup>), the dipole  
217 magnetic field is not appreciably deformed by the solar wind. As a result, the structures  
218 in the inner magnetosphere follow closely from the motion of charged particles in an  
219 ideal dipole field.

---

<sup>4</sup>In the outer magnetosphere (as well as most of the inner magnetosphere), collisions are so infrequent that magnetic flux is said to be “frozen in” to the plasma. Charged particles move freely along magnetic field lines, but cannot cross from one line to another. Compression of the magnetic field is synonymous with compression of the ambient plasma.

<sup>5</sup>In the case of an ideal plasma, Ohm's law takes the form  $\underline{E} + \underline{U} \times \underline{B} = 0$ .

<sup>6</sup>The McIlwain parameter  $L$  is used to index field lines in Earth's dipole geometry:  $L \equiv \frac{r}{\sin^2 \theta}$  for colatitude  $\theta$  and radius  $r$  in Earth radii. For example, the  $L = 5$  field line passes through the equatorial plane at a geocentric radius of  $5 R_E$ , then meets the Earth at a colatitude of  $\arcsin \sqrt{\frac{1}{5}} \sim 27^\circ$  (equally, a latitude of  $\arccos \sqrt{\frac{1}{5}} \sim 63^\circ$ ).

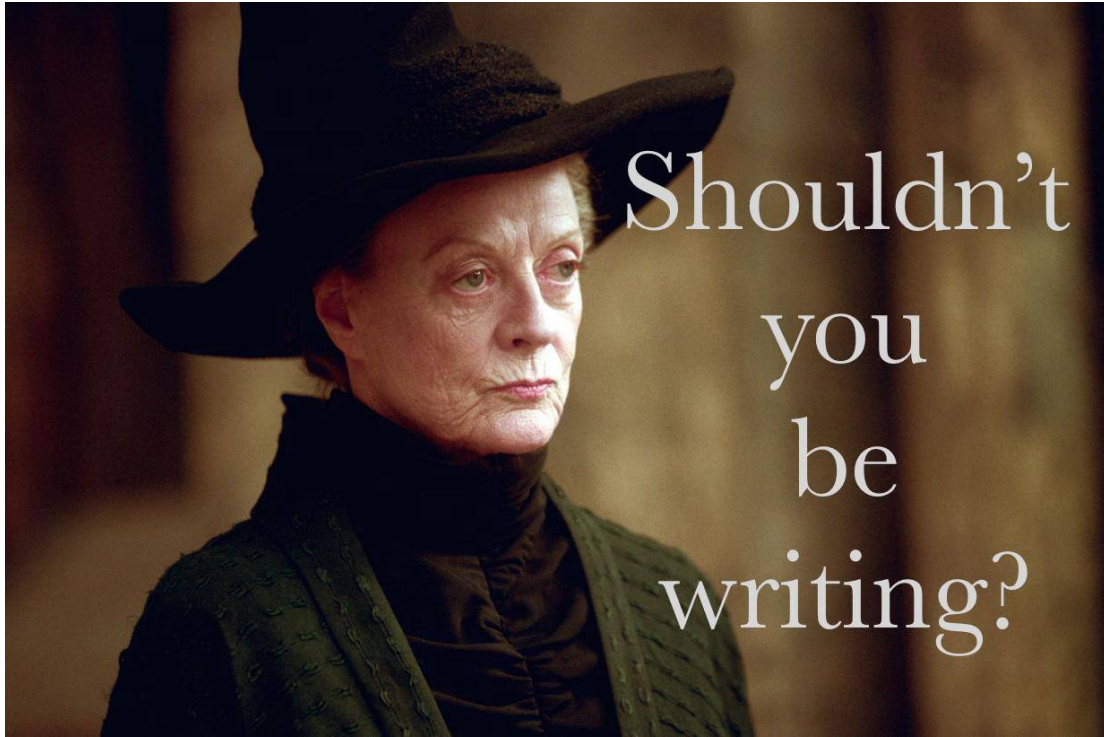


Figure 2.2: TODO: The inner magnetosphere...

- 220 The plasmasphere — a cold ( $\sim 1$  eV), dense ( $10^2 / \text{cm}^3$  to  $10^4 / \text{cm}^3$ ) torus of corotating  
221 plasma — is formed by the outward drift of atmospheric ions along magnetic closed  
222 field lines. Its outer boundary, is thought to represent a balance between the corotation  
223 electric field (per the rotation of Earth's magnetic dipole) and the convection electric  
224 field (associated with the convection of magnetic flux during the Dungey cycle). Particle  
225 density drops sharply at the edge of the plasmasphere; the boundary is called the  
226 plasmapause. The plasmapause typically falls around  $L = 4$ , though during prolonged  
227 quiet times it can extend to  $L = 6$  or larger.
- 228 Energetic particles trapped within the inner magnetosphere are divided into two popu-  
229 lations.
- 230 The Van Allen radiation belts are made up of particles with energy above  $10^5$  eV or  
231 so. The inner belt ( $L \lesssim 2$ ) is primarily composed of protons, the decay remnants of

232 neutrons freed from the atmosphere by cosmic rays. The outer belt ( $L \gtrsim 4$ ) is primarily  
233 composed of high-energy electrons.

234 Particles with energies of  $10^3$  eV to  $10^5$  eV make up the ring current, which extends  
235 from  $L \sim 3$  to  $L \sim 5$ . Gradient-curvature drift carries ions and electrons in opposite  
236 directions; the net result is a westward current. During quiet times, the ring current  
237 causes magnetic a southward magnetic field on the order of 1 nT at Earth's equator<sup>7</sup>.

## 238 2.3 The Ionosphere

239 Earth's neutral atmosphere is an excellent insulator. Collisions are so frequent that  
240 charged particles quickly thermalize and recombine. The breakdown of air molecules  
241 into a conductive plasma (as happens during a lightning strike, for example) requires  
242 electric fields on the order of  $10^9$  mV/m.

243 Currents are also suppressed by the magnetosphere. In the absence of collisions, elec-  
244 trons and ions drift alongside one another in response to an electric field, creating no  
245 net current perpendicular to the magnetic field<sup>8</sup>. Magnetic field lines are (to a good  
246 approximation) equipotential contours; electric fields do not form along them to drive  
247 parallel currents.

248 The ionosphere is a sweet spot between the two regimes. Collisions are frequent enough  
249 to disrupt the drift of ions, but not frequent enough to immobilize the electrons. The  
250 result is nonzero Pedersen and Hall conductivity, corresponding to current along the  
251 electric field and in the  $\underline{B} \times \underline{E}$  direction respectively. Collisions in the ionosphere  
252 also give rise to a finite parallel conductivity, allowing for the formation of potential  
253 structures along the magnetic field line.

254 **TODO: Field-aligned currents depend on the level of geomagnetic activity... but do**  
255 **they ever completely go away?**

---

<sup>7</sup>For comparison, Earth's dipole field points north at the equator with a magnitude over  $10^4$  nT.

<sup>8</sup>The so-called  $E$ -cross- $B$  drift is associated with a velocity of  $\underline{U} = \frac{1}{B^2} \underline{E} \times \underline{B}$ , independent of a charged particle's mass or sign.

256 The convection electric field (associated with the Dungey cycle, Section 2.1) drives Ped-  
257 ersen currents in the ionosphere. It is these currents that give rise to the strongest mag-  
258 netic fields on the ground. Pedersen currents flow downward on the flanks and duskward  
259 across the poles. The currents remain divergence-free by connecting to field-aligned cur-  
260 rents at the edges of the polar cap. The field-aligned currents, in turn, connect to the  
261 magnetopause current, the cross-tail current, and the (partial) ring current.  
  
262 When electron density is low, thermal velocities may be unable to carry enough current  
263 to satisfy  $\nabla \cdot \underline{J} = 0$ . This leads to the formation of potential structures along geomagnetic  
264 field lines in the ionosphere. Such structures accelerate particles along magnetic field  
265 lines, leading to the precipitation of energetic particles into the atmosphere. As the  
266 particles thermalize, they excite atmospheric atoms. The resulting spontaneous emission  
267 is often in the visible spectrum, giving rise to the aurora.

268 **TODO:** Particles can also be excited by Alfvén waves... this probably goes in Chapter 3.  
269

## 270 **2.4 Geomagnetic Storms and Substorms**

271 The quiet geomagnetic behavior described above is periodically disturbed by transient  
272 solar phenomena such as corotating interaction regions (CIRs) and coronal mass ejec-  
273 tions (CMEs). CMEs, as noted in Chapter 1, are bursts of unusually dense solar wind  
274 which are ejected from regions of high magnetic activity on the Sun; they are most  
275 common at the height of the eleven-year solar cycle. CIRs, on the other hand, occur  
276 when a relatively fast region of the solar wind catches up to an earlier and slower-moving  
277 pocket of solar wind, resulting in a pair of shockwaves.

278 During a storm, increased solar wind intensity results in enhanced magnetic reconnection  
279 on the dayside. As the newly-opened field lines are swept tailward, the convection  
280 electric field is strengthened. The plasmasphere — the outer boundary of which is  
281 set by a balance between the convection electric field and the (more or less constant)  
282 corotation electric field — sheds its outer layers. A large number of energetic particles  
283 are also injected into the ring current[68].

284 The strength of the storm is gauged by the size of the magnetic perturbation created  
285 by the ring current<sup>9</sup>. A small storm has a magnitude of 50 nT to 100 nT. Large storms  
286 may reach 250 nT to 500 nT. The Carrington Event, mentioned in Chapter 1, is thought  
287 to have exceeded 1700 nT[96].

288 The main phase of a storm typically lasts for several hours. Storm recovery — the grad-  
289 ual return of the storm index to zero — typically lasts several days. The plasmapause  
290 refilling occurs on timescales of **TODO: ???**. Geomagnetic storms occur tens of times  
291 per year at the height of the solar cycle, and just a few times per year otherwise.

292 Whereas storms are prompted by large solar wind events on the dayside, geomagnetic  
293 substorms are primarily a nightside occurrence. As flux accumulates in the tail, mag-  
294 netic tension builds in the stretched field lines. A substorm is an impulsive release of  
295 that tension.

296 **TODO: Phases of a substorm.** Definition of a substorm comes from [1]. Revised by [69].  
297

298 At substorm onset, a burst of reconnection occurs in the tail. A jet of plasma is launched  
299 Earthward from the reconnection site (and another is launched tailward, and lost to the  
300 solar wind). The Earthward plasma injection injects particles into the ring current.  
301 The outer radiation belt is depleted, then repopulated. Energetic particles precipitate  
302 into the atmosphere, giving rise to a distinctive **TODO: hour-long** sequence of auroral  
303 signatures.

304 Concurrent with substorm onset, impulsive Alfvén waves are observed with periods of  
305 a minute or two. The precise ordering of events — whether reconnection causes the  
306 waves, or vice versa, or if they share a common cause — remains controversial.

307 Each substorm lasts several hours, including the time it takes for the ring current to  
308 return to pre-substorm levels. Several substorms may occur per day during quiet times.  
309 During a storm, substorms become far more frequent; by the time one has ended,  
310 another may have already begun.

---

<sup>9</sup>The most commonly used storm index is Dst, which is computed hourly using measurements from several ground magnetometers near the equator. The Sym-H index, used in Section 5.3, is computed once per minute.

# 311 Chapter 3

## 312 Field Line Resonance

- 313 The motion of a charged particle in a dipole field can be described in terms of three  
314 fundamental motions. The first is cyclotron motion: a particle orbits around a magnetic  
315 field line in accordance with the Lorentz force. The second is bounce motion: while  
316 orbiting, the particle moves along the field line like a bead on a wire, back and forth  
317 between the northern and southern hemispheres<sup>1</sup>. The third is drift motion: as particles  
318 orbit and bounce, they also move azimuthally around Earth per the gradient-curvature  
319 drift.
- 320 Characteristic timescales for each of the above motions depend on particle energy. Elec-  
321 tron cyclotron motion is on the order of TODO: ... in the ionosphere, and closer to  
322 TODO: ... in the tail; ions gyrate slower by three orders of magnitude due to their  
323 larger mass. TODO: Bounce... Drift...
- 324 Wave-particle resonance arises when a particle's periodic motion matches with the fre-  
325 quency of a coincident electromagnetic wave[24, 63, 74, 85]. In the particle's rest frame,  
326 the wave then appears as a net electric field. This allows a net movement of energy

---

<sup>1</sup>As a particle approaches Earth, it experiences an ever-stronger magnetic field. The particle's perpendicular kinetic energy increases in proportion with the magnetic field in order to conserve its first adiabatic invariant. When the perpendicular kinetic energy can no longer increase — that is, when the parallel kinetic energy is zero — the particle bounces back. (If the parallel kinetic energy is sufficiently large, the particle doesn't bounce; it precipitates into the atmosphere.)

327 between the wave and the particle. The interaction is analogous to a surfer moving  
 328 along with — and being accelerated by — a wave in the ocean.

329 In the present work, the waves in question are field line resonances (FLRs). An FLR  
 330 is a standing harmonic on a geomagnetic field line. It can also be envisioned as a  
 331 superposition of traveling waves, reflecting back and forth between its northern and  
 332 southern foot points at the conducting ionosphere. These waves travel at the Alfvén  
 333 speed<sup>2</sup>. The fundamental equations of field line resonance were presented by Dungey in  
 334 1954[21]; since then, they have remained a topic of active study.

335 So-called ultra low frequency waves — of which FLRs are a subset — are categorized  
 336 by morphology. Continuous (long-lived) pulsations are termed Pc, while irregular pul-  
 337 sations are called Pi. Within each are a number of frequency bands; see Table 3.1[45].

Table 3.1: IAGA Magnetic Pulsation Frequency Bands

	Pc1	Pc2	Pc3	Pc4	Pc5	Pi1	Pi2
Period (s)	0.2–5	5–10	10–45	45–150	150–600	1–40	40–150
Frequency (mHz)	200–5000	100–200	22–100	7–22	2–7	25–1000	7–25

338 **TODO:** Boundaries between wave bands are, in practice, not strict. They are sometimes  
 339 fudged to better match phenomenological boundaries.

340 FLRs fall into the Pc3, Pc4, and Pc5 ranges. The present work focuses specifically  
 341 on the Pc4 band: waves with periods of a minute or two. Frequencies in the Pc4  
 342 range typically coincide with Alfvén bounce times<sup>3</sup> near the plasmapause:  $L \sim 4$  to  
 343  $L \sim 6$ [3, 17, 25, 56]<sup>4</sup>. In fact, the large radial gradients in the Alfvén speed near the  
 344 plasmapause act as an effective potential well, trapping FLRs[16, 50, 53, 54, 62, 88].

<sup>2</sup>The Alfvén speed is given by  $v_A$  is given by  $v_A^2 \equiv \frac{B^2}{\mu_0 \rho}$ , where  $B$  is the magnitude of the magnetic field,  $\mu_0$  is the magnetic constant, and  $\rho$  is the mass density of the ambient plasma. It can vary by several orders of magnitude over the length of a magnetic field line.

<sup>3</sup>The Alfvén frequency is the inverse of the Alfvén bounce time:  $\frac{2\pi}{\omega_A} \equiv \oint \frac{dz}{v_A}$ .

<sup>4</sup>Not coincidentally, these are the same  $L$ -shells where the Van Allen Probes spend most of their time; see Chapter 8.

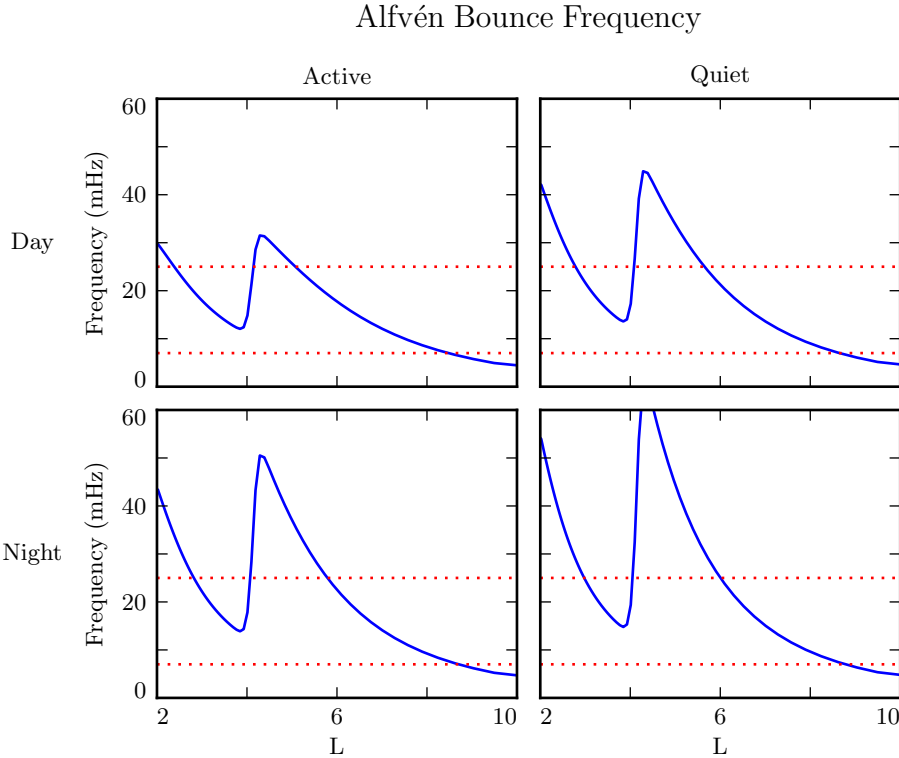


Figure 3.1: The above are bounce frequencies for an Alfvén wave moving back and forth along a geomagnetic field line. Alfvén speeds are computed based on profiles from Kelley[48], as discussed in Section 5.2. Notably, the bounce frequency depends significantly on the position of the plasmasphere, taken here to be at  $L = 4$ . Dotted lines indicate the Pc4 frequency range: 7 mHz to 25 mHz.

- 345 In addition to being radially localized, FLRs in the Pc4 frequency band (also called Pc4
- 346 pulsations, or just Pc4s) are localized in magnetic local time (MLT<sup>5</sup>). They have also
- 347 been shown to occur preferentially on the dayside, during storms or storm recovery[3,
- 348 17, 25, 52, 56, 97].
- 349 In the inner magnetosphere, the Alfvén frequency — and thus the frequency of FLRs
- 350 — often coincides with integer or half-integer<sup>6</sup> multiples of particle drift frequencies[18].

<sup>5</sup>Noon points toward the Sun and midnight away from it, with 06:00 and 18:00 at the respective dawn and dusk flanks.

<sup>6</sup>See Section 3.1.

351 The resulting wave-particle interactions can give rise to significant energization and  
352 radial diffusion of the particles. In some cases, the waves also include an electric field  
353 parallel to the background magnetic field, contributing to the precipitation of energetic  
354 particles into the neutral atmosphere[32, 33, 93, 103].

355 The present chapter introduces the structural characteristics of FLRs, how those charac-  
356 teristics affect wave behavior, and several unresolved questions related to that behavior.

357 **TODO:** The polarization of long-period Alfven waves is rotated by  $\sim 90^\circ$  when passing  
358 through the ionosphere[41]. A wave that is azimuthally polarized in space is polarized  
359 north-south on the ground, and vice versa. It has been noted specifically that Pgs  
360 exhibit east-west polarized ground signatures[92].

361 **TODO:** Other planets[31]? Seems exciting but maybe not relevant.

### 362 3.1 Harmonic Structure

363 Wave structure along a geomagnetic field line is indicated by harmonic number. The  
364 first (or fundamental) harmonic has a wavelength twice as long as the field line. It  
365 exhibits an antinode in the perpendicular electric field at the equator, along with a  
366 node in the perpendicular magnetic field. The second harmonic is a single wavelength  
367 along the field line. Its perpendicular magnetic perturbation has an antinode at the  
368 equator, while its perpendicular electric field has a node. Figure 3.2 shows a qualitative  
369 sketch of each: a series of snapshots in time, in the rest frame of the wave. Perpendicular  
370 electric and magnetic field perturbations are shown in blue and red respectively.

371 A first-harmonic FLR that is periodic or localized in the azimuthal direction is conducive  
372 to drift-resonant wave-particle interactions[18, 75]. The particle is like a child on a swing:  
373 whenever the path of the particle (or child) gets close to the wave (parent), it gets a  
374 push, and always in the same direction. The wave fields spend half its time pointing  
375 the other direction, just as the parent must shift their weight backward to get ready for  
376 the next push, but at that point the particle (child) is far away.

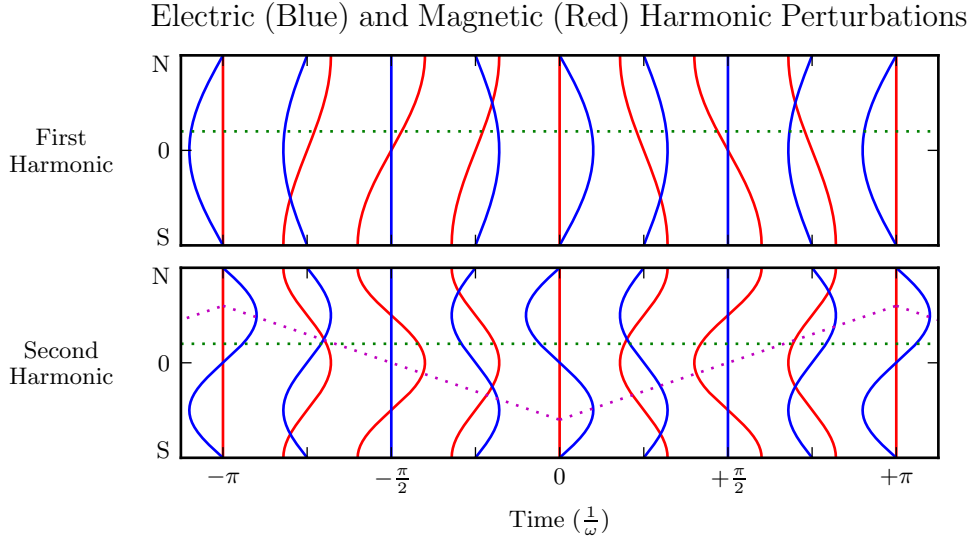


Figure 3.2: The first (or fundamental) harmonic has an antinode in its perpendicular electric field (blue) at the equator, along with a node in its perpendicular magnetic field perturbation (red). A single satellite can identify the first harmonic by the relative phase of the electric and magnetic field perturbations: an observer north of the equator (green) will see the magnetic field perturbation lead the electric field by  $90^\circ$ . The second harmonic is the opposite: it has an electric field node at the equator, and an observer north of the equator will see the magnetic field perturbation lag the electric field by  $90^\circ$ . The purple line sketches the path of a particle in drift-bounce resonance; in the particle’s rest frame, the electric field is always to the right. **TODO:** Actually, toroidal waves are flipped — Faraday’s law gives  $\frac{\partial}{\partial t} B_x \sim \frac{\partial}{\partial z} E_y$  but  $\frac{\partial}{\partial t} B_y \sim -\frac{\partial}{\partial z} E_x$ .

377 Second-harmonic FLRs interact with particles through the drift-bounce resonance, which  
 378 is slightly more complicated. As the particle drifts azimuthally, it also zig-zags north-  
 379 south. The combination of those two periodic motions must align with the phase of  
 380 the wave electric field. An example path is shown by the purple line in Figure 3.2: the  
 381 particle experiences a rightward electric field throughout the wave’s oscillation.

The drift and drift-bounce resonance conditions are written, respectively[89]:

$$\omega - m\omega_D = 0 \quad \text{and} \quad \omega - m\omega_D = \omega_B \quad (3.1)$$

382 Where  $\omega$  is the frequency of the wave,  $\omega_D$  and  $\omega_B$  are the particle's drift and bounce  
383 frequencies respectively, and  $m$  is the wave's azimuthal modenumber, as discussed in  
384 Section 3.2.

385 In principle, the first and second harmonics can be distinguished by their frequencies,  
386 even from a single-point observation[15, 34]. In practice, however, this is not a reliable  
387 approach[90]. There are significant uncertainties surrounding the number density profile  
388 — and thus the Alfvén speed profile — along a geomagnetic field line.

389 Harmonic structure can also be deduced by noting the phase offset between the wave  
390 magnetic field and its electric field (or the plasma velocity)[17, 92]. In Figure 3.2,  
391 the green line indicates an observer just north of the magnetic equator. For the first  
392 harmonic, the observer sees the electric field waveform lead the magnetic field by a  
393 phase of  $90^\circ$ ; for the second harmonic, the electric field waveform lags by  $90^\circ$ . (South  
394 of the equator, the signs are reversed.) Notably, this approach has only become viable  
395 with the advent of satellites carrying both electric and magnetic field instrumentation,  
396 such as THEMIS in 2007[4] and the Van Allen Probes<sup>7</sup> in 2012[86].

397 Strictly speaking, the the phase offset of the electric and magnetic fields does not provide  
398 the harmonic number — only its parity. It's reasonably safe to assume that an even mode  
399 is the second harmonic; the second harmonic is by far the most commonly observed[44,  
400 83, 91], due in part to its excitement by the antisymmetric balloon instability[9, 11,  
401 13, 85]. However, the distinction between the first and third harmonics is not always  
402 clear; this issue is discussed further in Chapter 8. Higher harmonics than that are not  
403 expected in the Pc4 frequency band.

404 **TODO:** Second-harmonic FLRs are unlikely to cause ground signatures[92].

405 **TODO:** Dai found a nice event[18] that was unambiguously determined to be a fundamental-  
406 mode Pc4 in drift-resonant interaction with  $\sim 10^5$  eV ions. Consistent with [94]. Other  
407 observations of odd harmonics: [104, 26].

---

<sup>7</sup>The Van Allen Probes were previously called RBSP, for Radiation Belt Storm Probes.

408 **3.2 Azimuthal Modenumber**

409 The wavelength of an FLR in the azimuthal direction is indicated by its azimuthal  
410 wavelength. A wave with modenumber  $m$  has an azimuthal wavelength that spans  $\frac{24}{m}$   
411 hours in MLT.

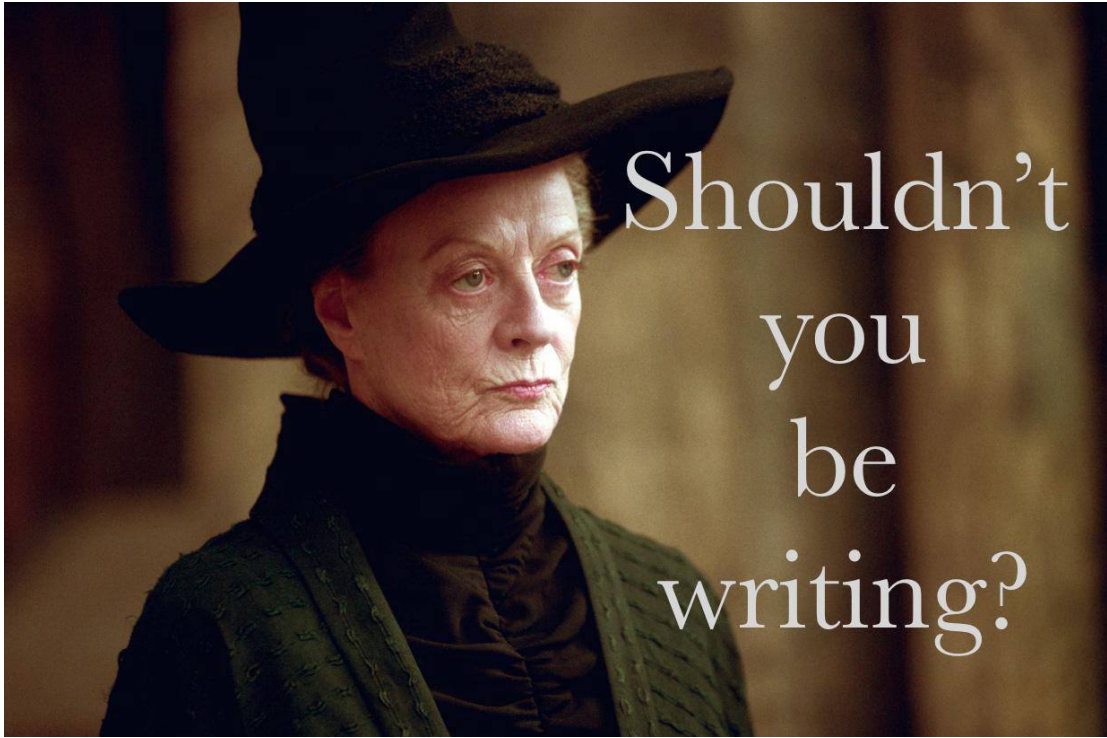


Figure 3.3: TODO: Large and small azimuthal modenumbers.

412 Waves with small azimuthal modenumbers ( $0 < m < 10$ ) are typically driven by broad-  
413 band energy sources at the magnetosphere's boundary, such as variations in the so-  
414 lar wind pressure[19, 38, 49, 107, 108], sporadic magnetic reconnection[42], or Kelvin-  
415 Helmholtz waves on the magnetopause[10, 57, 84]. In the low- $m$  regime, the shear and  
416 compressional Alfvén waves are coupled, which allows energy to move across field lines  
417 until the driving frequency lines up with the local Alfvén frequency[59]. Because of their  
418 broadband energy source, low- $m$  FLRs often have a mishmash of frequencies present in  
419 their spectra[17].

- 420 When the azimuthal modenumber is large (or, equally, when the azimuthal wavelength  
 421 is small), the shear and compressional Alfvén waves are decoupled[15, 78]<sup>8</sup>. As a result,  
 422 FLRs must be driven from within the magnetosphere. Proposed energy sources include  
 423 phase space gradients near the plasmapause[18], particularly as the plasmasphere refills  
 424 after a storm or substorm[25, 55].
- 425 The ionosphere is known to attenuate waves with small spatial extent in the perpendic-  
 426 ular direction[43, 102, 106]. As a result, FLRs may create no signature on the ground if  
 427 their azimuthal modenumber is large. For example, a recent paper by Takahashi shows  
 428 a strong (2 nT at  $L \sim 10$ ), clear resonance with  $|m| \gtrsim 70$  and no corresponding ground  
 429 signature[90].

Southwood[85] and Glassmeier[29] show that a low frequency wave passing through the ionosphere on its way to Earth will be attenuated per

$$\frac{B_E}{B_I} = \frac{\Sigma_H}{\Sigma_P} \exp\left(-m \frac{R_I - R_E}{R_E \sin \theta}\right) \quad (3.2)$$

- 430 Where  $B_E$  and  $B_I$  are the magnetic field strengths at  $R_E$  (Earth's surface, 6783 km  
 431 geocentric) and  $R_I$  (the ionosphere,  $\sim$ 6900 km geocentric) respectively. The integrated  
 432 ionospheric Pedersen and Hall conductivities,  $\Sigma_P$  and  $\Sigma_H$ , are typically within a factor  
 433 of two of one another. Field lines near the plasmapause can be traced to Earth at  
 434  $\sin \theta \sim 0.4$ . That is, by the time it reaches the ground, the magnetic field from an FLR  
 435 with  $m = 10$  is weaker by a factor of two; at  $m = 100$ , the factor is closer to 100.

### 436 3.3 Poloidal and Toroidal Polarizations

- 437 Based on polarization, each FLR can be classified as either poloidal or toroidal. The  
 438 poloidal mode is a field line displacement in the meridional plane, as shown in Figure 3.4,  
 439 with an accompanying electric field in the azimuthal direction. The toroidal mode's  
 440 magnetic displacement is azimuthal, per Figure 3.5; the associated electric field is in the  
 441 meridional plane.

---

<sup>8</sup>Equally, the strength of a wave's parallel component hint at its modenumber, a point which is revisited in Chapter 8.

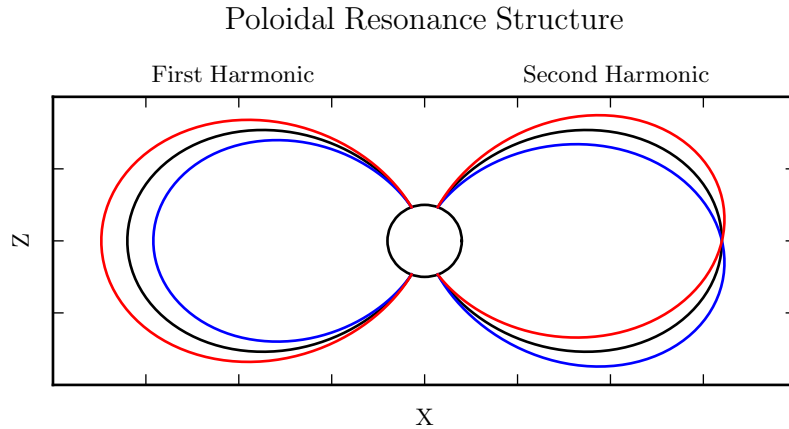


Figure 3.4: The poloidal resonance is a magnetic field in the meridional plane. The displacement is radial near the equator, and can be accompanied by enhancement in the parallel magnetic field near the ionosphere. The first harmonic is shown on the left, and the second harmonic on the right. Lines are colored red and blue only to contrast with the unperturbed black field line.

442 Both poloidal and toroidal waves are noted for their ability to contribute to the energiza-  
 443 tion and radial diffusion of trapped particles. The poloidal mode interacts more strongly,  
 444 since its electric field is aligned with the trapped particles’ drift motion. Poloidally-  
 445 polarized waves are also more prone to creating magnetic signatures on the ground, due  
 446 to ducting in the ionosphere[27, 36].

447 Toroidal modes have been shown to far outnumber poloidal modes[3]. Perhaps not  
 448 coincidentally, poloidally-polarized waves rotate asymptotically to the toroidal mode[64,  
 449 65, 78]. Poloidal waves with low azimuthal modenumber — such as those driven by  
 450 broadband sources at the magnetopause — rotate on timescales comparable to their  
 451 oscillation periods.

452 **TODO:** Fishbone instability[12, 67]. Like the poloidal mode, but for lab plasmas.

453 **TODO:** Poloidal and toroidal modes are coupled by the ionospheric Hall conductivity[47].  
 454 The Hall conductivity also increases the “ringtime” of these resonances, allowing them

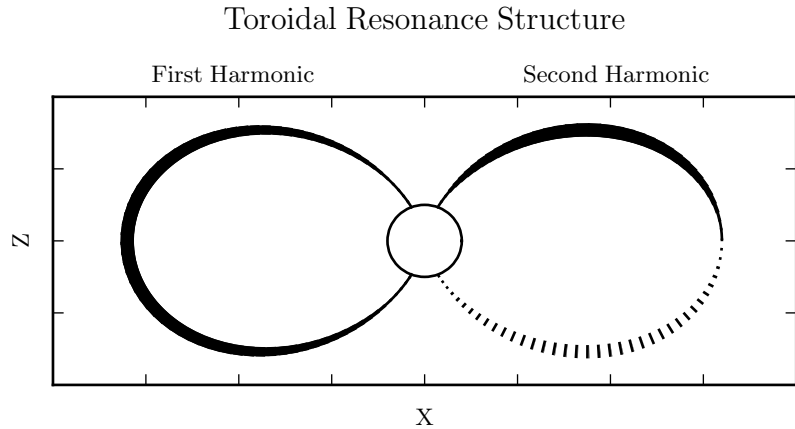


Figure 3.5: A toroidally-polarized FLR has a magnetic perturbation in the azimuthal direction, as shown. Bold lines are taken to be above the page, and dotted lines below the page, with the displacement indicated by the line's width. The first harmonic — where the entire field line oscillates in and out of the page — is shown on the left. The second harmonic is on the right, with northern and southern halves perturbed in opposite directions.

455 to oscillate through the inductive process rather than be dissipated as Joule heating[100].

456

457 TODO: Toroidal modes show a clear frequency dependence with  $L$ . Poloidal modes less  
458 so. Citation...?

### 459 3.4 Giant Pulsations

460 The study of geomagnetic pulsations long predates satellites, sounding rockets, or even  
461 the word “magnetohydrodynamics”<sup>9</sup>. Large, regular oscillations in the magnetic field  
462 were noted as early as 1901[5]. Eventually, the term “giant pulsation,” or Pg, arose to  
463 describe such pulsations.

---

<sup>9</sup>The term was first used by Alfvén in the 1940s[2].

464 On the ground, Pgs are notable for their strikingly sinusoidal waveforms, their eastward  
465 drifts, and their specific occurrence pattern: Pgs are typically seen pre-dawn, at latitudes  
466 of  $60^\circ$  to  $70^\circ$ . Pgs generally fall into the Pc4 frequency band<sup>10</sup>. Their harmonic structure  
467 was a source of controversy for decades, but recent multisatellite observations seem to be  
468 in agreement that they are odd harmonics, probably fundamental[30, 40, 51, 52, 89, 92].  
469 They are poloidally polarized, with modenumbers  $10 \lesssim m \lesssim 40$ [28, 40, 75, 81, 92].

470 Whereas FLRs are waves in space which may produce ground signatures, “giant pul-  
471 sation” refers to the ground signature specifically<sup>11</sup>. That is, Takahashi’s satellite ob-  
472 servation of a sinusoidal, morningside, high- $m$ , fundamental poloidal resonance was not  
473 classified as a Pg because it did not produce a signal on the ground[90].

474 **TODO: Pgs are localized to within  $2^\circ$  to  $5^\circ$  in latitude[70, 89, 98].**

475 Due to their remarkably clear waveforms, Pgs are typically found by “visual inspection  
476 of magnetometer data”[70]. Over the course of the past century, a number of multi-year  
477 (sometimes multi-decade[7]) surveys have totaled nearly one thousand Pg events. On  
478 average, a ground magnetometer near  $66^\circ$  magnetic latitude observes  $\sim 10$  Pg events per  
479 year[7, 39, 80, 87]. Observations are not distributed uniformly; rather, giant pulsations  
480 become more common near the equinox and during times of low solar activity.

481 Unlike Pc4 pulsations in general, Pgs show no particular correlation with storm phase[70].  
482 However, they do often occur as the magnetosphere recovers from a substorn[70, 81].

### 483 3.5 Motivations for the Present Work

484 A great deal has been learned — and continues to be learned — through observations of  
485 field line resonance. However, the cost-to-benefit ratio is climbing. As summarized in the  
486 sections above, FLR behavior depends significantly on harmonic structure, azimuthal  
487 modenumber, and polarization — not to mention frequency, spectral width, and so

<sup>10</sup>The Pc4 range is periods of 45 s to 140 s, while Pgs are often said to range from 60 s to 200 s[7].

<sup>11</sup>Historically, the wave designations shown in Table 3.1 all referred to ground phenomena. Over time,  
they have come to describe satellite observations as well, including those without corresponding sig-  
natures on the ground.

488 on. With each degree of freedom comes the necessity for an additional simultaneous  
489 observation.

490 Similarly, as FLRs have been shown to depend on ever-more-specific magnetospheric  
491 conditions, analytical techniques have fallen out of favor. The height-resolved iono-  
492 sphere, the multidimensional Alfvén speed profile, and the inconvenient geometry com-  
493 bine to create a problem beyond the reasonable purview of pencil and paper.

494 That is, the topic of field line resonance is ripe for numerical modeling.

495 Past models of the magnetosphere have been ill-suited for the consideration of FLRs.  
496 Reasons include overly-simplified treatment of the ionospheric boundary, no consider-  
497 ation of the plasmapause, limited range in  $m$ , and the inability to compute ground  
498 signatures. Chapter 5 presents a model which addresses these issues, allowing the com-  
499 putation of field line resonance with unparalleled attention to realism.

500 The model allows a bird’s-eye view of the structure and evolution of FLRs. As such,  
501 not only can several open questions be addressed, but their answers serve to unify a  
502 number of seemingly-disparate properties described in the sections above.

503 The rotation of poloidally-polarized waves to the toroidal mode is investigated. Par-  
504 ticular attention is paid to the importance of azimuthal modenumber and ionospheric  
505 conductivity. The interplay between said rotation and the transport of energy across  
506 field lines — which also depends on azimuthal modenumber — is considered as well.

507 By their nature, drifting particles have the potential to spur wave-particle interactions  
508 at all MLT. However, Pc4 observations are strongly peaked on the dayside. In a 2015  
509 paper, Dai notes, “It is not clear why noncompressional [high- $m$ ] Pc4 poloidal waves,  
510 which are presumably driven by instability within the magnetosphere, preferentially  
511 occur on the dayside”[17]. Motoba, later that year, echoes, “It is unclear whether other  
512 generation mechanisms of fundamental standing waves ... can explain the localization  
513 of Pgs in local time”[70]. This, too, is considered numerically: to what degree is field  
514 line resonance affected by the (day-night asymmetric) conditions of the ionosphere?

515 **TODO:** Transition... With the above in mind, what data would be super helpful?

516 It's been shown that a ground magnetometer 66° north of the magnetic equator observes  
517  $\sim$ 10 Pg events per year. It's also been shown that poloidal Pc4s are rare compared to  
518 toroidal ones, and that most poloidal Pc4s are even harmonics. However, little attention  
519 has been paid to how these rates line up with one another. Given the relative occurrence  
520 rate of poloidal and toroidal waves, of odd and even harmonics, and of diffuse and sharp  
521 spectral peaks, just how unusual are giant pulsations?

522 **Chapter 4**

523 **Waves in Cold Resistive Plasma**

524 Before delving into the implementation of the numerical model, it's instructive to consider the fundamental equations of waves in a cold, resistive plasma.

The evolution of electric and magnetic fields is governed by Ampère's law and Faraday's law. Notably, the present work takes the linearized versions of Maxwell's equations; the vectors  $\underline{E}$  and  $\underline{B}$  indicate perturbations above the zeroth-order magnetic field.

$$\underline{\epsilon} \cdot \frac{\partial}{\partial t} \underline{E} = \frac{1}{\mu_0} \nabla \times \underline{B} - \underline{J} \quad \frac{\partial}{\partial t} \underline{B} = -\nabla \times \underline{E} \quad (4.1)$$

Current follows Ohm's law. For currents perpendicular to the background magnetic field, Kirchhoff's formulation is sufficient. Conductivity is much higher along the magnetic field lines<sup>1</sup>, so it's appropriate to also include the electron inertial term<sup>2</sup>.

$$0 = \underline{\sigma}_{\perp} \cdot \underline{E}_{\perp} - \underline{J}_{\perp} \quad \frac{1}{\nu} \frac{\partial}{\partial t} J_z = \sigma_0 E_z - J_z \quad (4.2)$$

---

<sup>1</sup>The dipole coordinate system is defined rigorously in Section 5.1; at present, it's sufficient to take  $\hat{z}$  parallel to the zeroth-order magnetic field, and  $\hat{x}$  and  $\hat{y}$  perpendicular to  $\hat{z}$  (and to each other).

<sup>2</sup>Electron inertial effects are not included in the model described in Chapter 5, or in the results in Chapter 7; however, their implementation and impact are explored in Chapter 6.

Derivatives in Equations (4.1) and (4.2) can be evaluated by performing a Fourier transform. They can then be combined, eliminating the magnetic field and current terms.

$$\begin{aligned} 0 &= \underline{\underline{E}}_{\perp} + \frac{v_A^2}{\omega^2} (\underline{k} \times \underline{k} \times \underline{E})_{\perp} + \frac{i}{\epsilon_{\perp}\omega} \underline{\sigma}_{\perp} \cdot \underline{\underline{E}}_{\perp} \\ 0 &= E_z + \frac{c^2}{\omega^2} (\underline{k} \times \underline{k} \times \underline{E})_z + \frac{i\omega_P^2}{\omega(\nu - i\omega)} E_z \end{aligned} \quad (4.3)$$

The speed of light, Alfvén speed (including the displacement current correction), plasma frequency, and parallel conductivity are defined in the usual way:

$$c^2 \equiv \frac{1}{\mu_0\epsilon_0} \quad v_A^2 \equiv \frac{1}{\mu_0\epsilon_{\perp}} \quad \omega_P^2 \equiv \frac{ne^2}{m_e\epsilon_0} \quad \sigma_0 \equiv \frac{ne^2}{m_e\nu} \quad (4.4)$$

Using the vector identity  $\underline{k} \times \underline{k} \times \underline{E} = \underline{k} \underline{k} \cdot \underline{E} - k^2 \underline{E}$ , Equation (4.3) can be reassembled into a single expression,

$$0 = \left( \underline{\underline{\mathbb{I}}} + \frac{1}{\omega^2} \underline{\underline{V}}^2 \cdot \underline{k} \underline{k} - \frac{k^2}{\omega^2} \underline{\underline{V}}^2 + \frac{i}{\omega} \underline{\underline{\Omega}} \right) \cdot \underline{E} \quad (4.5)$$

Where  $\underline{\underline{\mathbb{I}}}$  is the identity tensor and in  $x$ - $y$ - $z$  coordinates,

$$\underline{\underline{V}}^2 \equiv \begin{bmatrix} v_A^2 & 0 & 0 \\ 0 & v_A^2 & 0 \\ 0 & 0 & c^2 \end{bmatrix} \quad \text{and} \quad \underline{\underline{\Omega}} \equiv \begin{bmatrix} \frac{\sigma_P}{\epsilon_{\perp}} & \frac{-\sigma_H}{\epsilon_{\perp}} & 0 \\ \frac{\sigma_H}{\epsilon_{\perp}} & \frac{\sigma_P}{\epsilon_{\perp}} & 0 \\ 0 & 0 & \frac{\omega_P^2}{(\nu - i\omega)} \end{bmatrix} \quad (4.6)$$

526 In Equation (4.5), the expression in parentheses is the dispersion tensor. Nontrivial  
527 solutions exist only when its determinant is zero. This gives rise to a seventh-order  
528 polynomial in  $\omega$ , so rather than a direct solution it's necessary to consider limits of  
529 specific interest.

530 Without loss of generality, the wave vector  $\underline{k}$  may be taken to lie in the  $x$ - $z$  plane — that  
531 is, with  $k_y = 0$ . The distinction between the two perpendicular directions is discussed  
532 in Section 4.4.

533 **4.1 Guided Propagation**

534 The wave vector of a field line resonance aligns closely to the background magnetic  
535 field. By supposing that the two align exactly (that is, taking  $k_x = 0$ ), the parallel and  
536 perpendicular components of the dispersion relation are decoupled.

The parallel-polarized component — that is, the solution when  $E_x = E_y = 0$  — is quadratic, and thus can be solved directly.

$$0 = \omega^2 + i\nu\omega - \omega_P^2 \quad \text{so} \quad \omega = -\frac{i\nu}{2} \pm \sqrt{\omega_P^2 - \frac{\nu^2}{4}} \quad (4.7)$$

537 It bears noting that the plasma frequency is large — not just compared to  $\text{Pc4}$  frequencies,  
538 but even compared to the collision frequencies in the ionosphere<sup>3</sup>.

Expanding Equation (4.7) with respect to large  $\omega_P$ , the dispersion relation becomes

$$\omega^2 = \omega_P^2 \pm i\nu\omega_P + \dots \quad (4.8)$$

539 Equation (4.8) can hardly be called a wave, as it does not depend on the wave vector  
540  $\underline{k}$ . Rather, it is the plasma oscillation<sup>4</sup>: electrons vibrating in response to a charge  
541 separation along the background magnetic field.

542 The plasma oscillation is not specifically relevant to the study of field line resonance.  
543 The two phenomena are separated by six orders of magnitude in frequency. The topic  
544 is revisited in Chapter 6 insomuch as it is inseparable from the electron inertial effects  
545 in Ohm's law.

---

<sup>3</sup>The collision frequency may match or exceed the plasma frequency for a thin slice at the bottom of the ionosphere, where the density of neutral atoms is large; however, it falls off quickly. Above an altitude of 200 km, conservatively[73], the plasma frequency exceeds the collision frequency by an order of magnitude or more.

<sup>4</sup>The plasma oscillation is also called the Langmuir wave, after Irving Langmuir.

The perpendicular ( $E_z = 0$ ) components of the dispersion relation give an expression quartic in  $\omega$ .

$$0 = \omega^4 + 2i\frac{\sigma_P}{\epsilon_\perp}\omega^3 - \left(2k_z^2v_A^2 + \frac{\sigma_P^2 + \sigma_H^2}{\epsilon_\perp^2}\right)\omega^2 - 2ik_z^2v_A^2\frac{\sigma_P}{\epsilon_\perp}\omega + k_z^4v_A^4 \quad (4.9)$$

Like the parallel-polarized component above, Equation (4.9) can be solved directly. Noting that  $\pm$  and  $\oplus$  are independent,

$$\omega = \left(\frac{\pm\sigma_H - i\sigma_P}{2\epsilon_\perp}\right) \oplus \sqrt{k_z^2v_A^2 + \left(\frac{\pm\sigma_H - i\sigma_P}{2\epsilon_\perp}\right)^2} \quad (4.10)$$

Also like the parallel-polarized component, the exact solution is less useful than its Taylor expansion. The Pedersen and Hall conductivities are large near the ionospheric boundary, but fall off quickly; for the vast majority of the field line, the ratios  $\frac{\sigma_P}{\epsilon_\perp}$  and  $\frac{\sigma_H}{\epsilon_\perp}$  are small compared to field line resonance frequencies. Expanding with respect to small conductivity gives

$$\omega^2 = k_z^2v_A^2 \oplus k_zv_A\frac{\sigma_H \pm i\sigma_P}{\epsilon_\perp} + \dots \quad (4.11)$$

546 This is the shear Alfvén wave, with a shift to its frequency due to the conductivity of  
 547 the ionosphere. It travels along the background magnetic field like a bead on a string,  
 548 with electric and magnetic field perturbations perpendicular to the magnetic field line  
 549 (and to one another).

## 550 4.2 Compressional Propagation

551 The partner to guided motion is compressional motion; in order for energy to move  
 552 across field lines, the wave vector must have a component perpendicular to  $\hat{z}$ . If the  
 553 wave vector is completely perpendicular to the magnetic field line ( $k_z = 0$ ), the parallel  
 554 and perpendicular components of the dispersion relation decouple, as in Section 4.1.

The parallel-polarized ( $E_x = E_y = 0$ ) component of the dispersion relation is

$$0 = \omega^3 + i\nu\omega^2 - (k_x^2 c^2 + \omega_P^2) \omega - ik_x^2 c^2 \nu \quad (4.12)$$

Equation (4.12) can be solved directly, though its solution (as a cubic) is far too long to be useful. Expanding with respect to the large plasma frequency, gives

$$\omega^2 = k^2 c^2 + \omega_P^2 - i\nu\omega_P + \dots \quad (4.13)$$

555 This is the O mode, a compressional wave with an electric field perturbation along  
 556 the background magnetic field. Like the plasma oscillation discussed in Section 4.1, its  
 557 frequency is very large compared to that of a field line resonance.

The perpendicular-polarized ( $E_z = 0$ ) component of the compressional dispersion relation is also cubic.

$$0 = \omega^3 + 2i\frac{\sigma_P}{\epsilon_\perp}\omega^2 - \left(2k_x^2 v_A^2 + \frac{\sigma_P^2 + \sigma_H^2}{\epsilon_\perp^2}\right) \omega - ik_x^2 v_A^2 \frac{\sigma_P}{\epsilon_\perp} \quad (4.14)$$

A wave moving across magnetic field lines near the ionospheric boundary will encounter large  $\frac{\sigma_P}{\epsilon_\perp}$  and  $\frac{\sigma_H}{\epsilon_\perp}$ , while at moderate to high altitudes those ratios will be small. Solving Equation (4.14) in those two limits respectively gives:

$$\omega^2 = k_x^2 v_A^2 \pm ik_x v_A \frac{\sigma_P}{\epsilon_\perp} + \dots \quad \text{and} \quad \omega^2 = k_x^2 v_A^2 + \left(\frac{\sigma_H \pm i\sigma_P}{\epsilon_\perp}\right)^2 + \dots \quad (4.15)$$

558 In both limits, Equation (4.15) describes a compressional Alfvén wave. The magnetic  
 559 field perturbation is along the background magnetic field — indicating compression of  
 560 the frozen-in plasma — while the electric field perturbation is perpendicular to both  
 561 the magnetic field and the wave vector.

562 **TODO: Double check terminology.** Jesse's dissertation disagrees with Bob's notes.

### 563 4.3 High Altitude Limit

564 In the limit of large radial distance, it's reasonable to take the collision frequency to  
 565 zero; doing so also neglects the Pedersen and Hall conductivities.

Whereas in Sections 4.1 and 4.2 it was the parallel-polarized component of the dispersion relation that factored out from the other two, the high altitude limit decouples the component polarized out of the  $x$ - $z$  plane. The  $y$ -polarized dispersion ( $E_x = E_z = 0$ ) is simply:

$$\omega^2 = k^2 v_A^2 \quad (4.16)$$

566 Equation (4.16) describes an Alfvén wave with an arbitrary angle of propagation. De-  
 567 pending on the angle between the wave vector and the background magnetic field, it  
 568 could be guided, compressional, or somewhere in between. Regardless of propagation  
 569 angle, the electric field perturbation is perpendicular to both the direction of propaga-  
 570 tion and the magnetic field perturbation.

The other two components (from  $E_y = 0$ ) of the high altitude dispersion tensor give an expression quadratic in  $\omega^2$ :

$$0 = \omega^4 - (k_x^2 c^2 + k_z^2 v_A^2 + \omega_P^2) \omega^2 + k_z^2 v_A^2 \omega_P^2 \quad (4.17)$$

Which can be solved for

$$\omega^2 = \frac{1}{2} (k_x^2 c^2 + k_z^2 v_A^2 + \omega_P^2) \pm \sqrt{\frac{1}{4} (k_x^2 c^2 + k_z^2 v_A^2 + \omega_P^2)^2 - k_z^2 v_A^2 \omega_P^2} \quad (4.18)$$

Noting again that  $\omega_P$  is very large, the two roots can be expanded to

$$\omega^2 = k_z^2 v_A^2 \left( 1 - \frac{k_x^2 c^2 + k_z^2 v_A^2}{\omega_P^2} \right) + \dots \quad \text{and} \quad \omega^2 = k_x^2 c^2 + k_z^2 v_A^2 + \omega_P^2 + \dots \quad (4.19)$$

571 The first is a shear Alfvén wave, as in Equation (4.11). The second oscillates faster than  
 572 the plasma frequency; like the plasma oscillation in Equation (4.8) and the O mode in  
 573 Equation (4.13), it's far outside the Pc4 frequency range.

## 574 4.4 Implications to the Present Work

575 The present section's findings carry three significant implications for the present work.  
 576 First — with the exception of the plasma oscillation and similar modes, which are  
 577 revisited in Chapter 6 — waves propagate at the Alfvén speed. This, in combination  
 578 with the grid configuration, will constrain the time step that can be used to model them  
 579 numerically. The time step must be sufficiently small that information traveling at the  
 580 Alfvén speed cannot “skip over” entire grid cells<sup>5</sup>.

Second, the results of the present section allow an estimate of the magnitude of parallel electric field that might be expected from a field line resonance compared to its perpendicular electric field. Between the full dispersion tensor form in Equation (4.5) and the Alfvén wave described by Equation (4.19),

$$\left| \frac{E_z}{E_x} \right| = \frac{k_x k_z c^2}{\omega^2 - k_x^2 c^2 - \omega_P^2} \sim \frac{k^2 c^2}{\omega_P^2} \quad (4.20)$$

581 In essence, the relative magnitudes of the parallel and perpendicular electric fields should  
 582 be in proportion to the square of the relative magnitudes of the electron inertial length  
 583 (1 km to 100 km) and the wavelength ( $\sim 10^5$  km). That is, parallel electric fields should  
 584 be smaller than the perpendicular electric fields by six or more orders of magnitude.

585 Finally, the dispersion relations shown above indicate how the behavior of a field line  
 586 resonance should behave as the azimuthal modenumber becomes large.

587 Whereas the shear Alfvén wave's dispersion relation depends only on the parallel com-  
 588 ponent of the wave vector, the compressional Alfvén wave depends on its magnitude:  
 589  $\omega^2 = k^2 v_A^2$ . If the frequency is smaller than  $k v_A$ , the wave will become evanescent. The

---

<sup>5</sup>As is the convention, the time step is scaled down from the smallest Alfvén zone crossing time by a Courant factor, typically 0.1, meaning that it takes at least ten time steps to cross a grid cell.

590 wave vector's magnitude can be no smaller than its smallest component, however, and  
 591 the azimuthal component scales with the azimuthal modenumber:  $k_y \sim \frac{m}{2\pi r}$ .

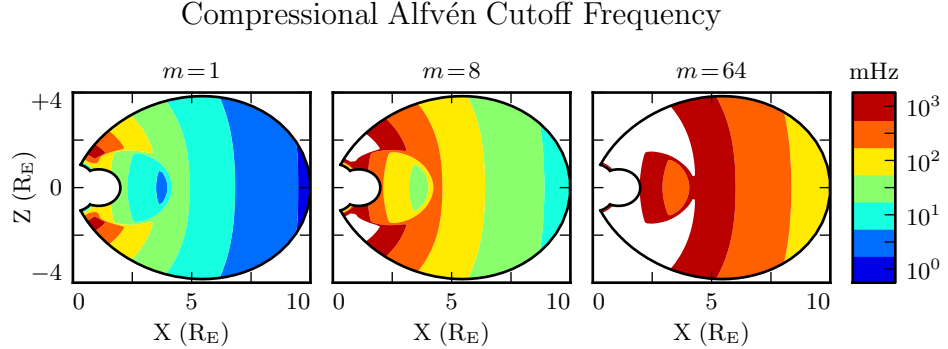


Figure 4.1: Taking  $k_y \sim \frac{m}{2\pi r}$  as a lower bound for the magnitude of the wave vector, the above figure demonstrates the lowest frequency at which compressional Alfvén waves may propagate as a function of position and  $m$ . Regions shown in white are off the color scale — they have a lower bound on the order of  $10^4$  mHz or more. The above Alfvén frequency profile is from Kelley[48], for quiet dayside conditions, as discussed in Section 5.2.

592 This imposes a frequency cutoff on compressional Alfvén waves which scales with the  
 593 azimuthal modenumber, as shown in Figure 4.1. At small values of  $m$ , most of the mag-  
 594 netosphere is conducive to compressional Alfvén waves in the Pc4 frequency range. As  
 595  $m$  increases, and the wave vector with it, the inner magnetosphere becomes increasingly  
 596 inaccessible to them.

597 **Chapter 5**

598 **“Tuna Half” Dimensional Model**

599 The present section describes the implementation of Tuna, a new two and a half dimensional  
600 Alfvén wave code based largely on work by Lysak[58, 61].

601 The half-integer dimensionality refers to the fact that Tuna’s spatial grid resolves a  
602 two-dimensional slice of the magnetosphere, but that electric and magnetic fields —  
603 as well as their curls — are three-dimensional vectors. This apparent contradiction is  
604 reconciled by the use of a fixed azimuthal modenumber,  $m$ . Electric and magnetic fields  
605 are taken to be complex-valued, varying azimuthally per  $\exp(im\phi)$ ; derivatives with  
606 respect to  $\phi$  are then replaced by a factor of  $im$ .

607 Unlike a fully three-dimensional code, Tuna cannot resolve the evolution of wave structures  
608 in the azimuthal direction. Furthermore, the model does not allow coupling between  
609 the dayside and nightside magnetospheres. What Tuna does offer is efficiency.  
610 The model’s economical geometry allows it to include a realistic Earthward boundary:  
611 grid spacing on the order of 10 km, a height-resolved ionospheric conductivity tensor,  
612 and even the computation of magnetic field signatures at the ground. Such features are  
613 computationally infeasible for a large global code.

614 Tuna was developed with field line resonance in mind. As discussed in Chapter 3,  
615 such waves are azimuthally localized, minimizing the importance of Tuna’s missing half  
616 dimension. Moreover, because field line resonances are known to be affected by both

617 the ionosphere and the plasmasphere, a faithful treatment of the inner magnetosphere  
618 is a crucial part of studying them numerically.

619 Perhaps the most exciting feature of Tuna is its novel driving mechanism: ring current  
620 perturbation. Codes similar to Tuna have traditionally been driven using compressional  
621 pulses at the outer boundary[58, 61, 100, 101]. This has precluded the investigation of  
622 waves with large azimuthal modenumber — such as giant pulsations — which are guided,  
623 and thus must be driven from within the magnetosphere.

624 TODO: The dipole geometry isn't super new, but it's not widely used. The height-  
625 resolved ionosphere is new and exciting! Ground signatures are new and exciting!

626 TODO: The support software — the driver and the plotter — are also significant. Do  
627 they get mentioned here? Does the Git repository where the code can be accessed get  
628 mentioned here?

## 629 5.1 Coordinate System

Field line resonance has traditionally been modeled by straightening the field lines into a rectangular configuration[21, 64], by unrolling the azimuthal coordinate into a cylindrical coordinate system[78], or through the use of dipole coordinates[77]<sup>1</sup>:

$$x \equiv -\frac{\sin^2 \theta}{r} \quad y \equiv \phi \quad z \equiv \frac{\cos \theta}{r^2} \quad (5.1)$$

630 Where  $r$ ,  $\theta$ , and  $\phi$  take on their usual spherical meanings of radial distance, colatitude,  
631 and azimuthal angle respectively.

632 The dipole coordinate  $x$  is constant over each equipotential shell<sup>2</sup>,  $y$  is azimuthal angle,  
633 and  $z$  indexes each field line from south to north. The unit vectors  $\hat{x}$ ,  $\hat{y}$ , and  $\hat{z}$  point

---

<sup>1</sup>The dipole coordinates  $x$ ,  $y$  and  $z$  are perhaps more commonly named  $\mu$ ,  $\phi$ , and  $\nu$  respectively; however, in the present work,  $\mu$  and  $\nu$  take other meanings.

<sup>2</sup>In fact,  $x$  is inversely proportional to the McIlwain parameter  $L$ .

634 in the crosswise<sup>3</sup> (radially outward at the equator), azimuthal (eastward), and parallel  
 635 (northward at the equator) directions respectively.

Notably, the dipole coordinates in Equation (5.1) are normal to one another. While mathematically convenient, they do not readily accommodate a fixed-altitude boundary at the ionosphere, nor do they allow the dipole magnetic field to intersect the boundary at an oblique angle, as Earth's field does. As a solution, a nonorthogonal set of dipole coordinates was developed numerically by Proehl[76], then formalized analytically by Lysak[58] in terms of their contravariant components:

$$u^1 = -\frac{R_I}{r} \sin^2 \theta \quad u^2 = \phi \quad u^3 = \frac{R_I^2}{r^2} \frac{\cos \theta}{\cos \theta_0} \quad (5.2)$$

636 Above,  $R_I$  is the position of the ionosphere relative to Earth's center; it's typically taken  
 637 to be  $1 R_E + 100 \text{ km}$ .

638 Like the dipole coordinates  $x$ ,  $y$ , and  $z$ , Lysak's coordinates  $u^1$ ,  $u^2$ , and  $u^3$  correspond to  
 639  $L$ -shell, azimuthal angle, and position along a field line respectively. However, compared  
 640 to  $z$ ,  $u^3$  has been renormalized using the invariant colatitude<sup>4</sup>  $\theta_0$ . As a result,  $u^3$  takes  
 641 the value  $+1$  at the northern ionospheric boundary and  $-1$  at the southern ionospheric  
 642 boundary for all field lines.

Because Lysak's coordinate system is not orthogonal<sup>5</sup>, it's necessary to consider covariant and contravariant basis vectors separately.

$$\hat{e}_i \equiv \frac{\partial}{\partial u^i} \underline{x} \quad \hat{e}^i \equiv \frac{\partial}{\partial \underline{x}} u^i \quad (5.3)$$

Covariant basis vectors  $\hat{e}_i$  are normal to the curve defined by constant  $u^i$ , while contravariant basis vectors  $\hat{e}^i$  are tangent to the coordinate curve (equivalently,  $\hat{e}^i$  is normal

---

<sup>3</sup>In the context of in situ measurements taken near the equatorial plane,  $\hat{x}$  is referred to as the radial direction; however, the present work extends the dipole grid to low altitudes, where  $\hat{x}$  can be more horizontal than vertical. The term "crosswise" is meant to indicate that  $\hat{x}$  is defined by the cross product of  $\hat{y}$  and  $\hat{z}$ .

<sup>4</sup>The invariant colatitude is the colatitude  $\theta$  at which a field line intersects the ionosphere. It is related to the McIlwain parameter by  $\cos \theta_0 \equiv \sqrt{1 - \frac{R_I}{L}}$ .

<sup>5</sup>Curves of constant  $u^1$  and curves of constant  $u^3$  can intersect at non-right angles.

to the plane defined by constant  $u^j$  for all  $j \neq i$ ). These vectors are reciprocal<sup>6</sup> to one another, and can be combined to give components of the metric tensor  $\underline{\underline{g}}$ [20].

$$\hat{e}^i \cdot \hat{e}_j = \delta_j^i \quad g_{ij} \equiv \hat{e}_i \cdot \hat{e}_j \quad g^{ij} \equiv \hat{e}^i \cdot \hat{e}^j \quad (5.4)$$

The metric tensor allows rotation between covariant and contravariant representations of vectors.

$$A_i = g_{ij} A^j \quad \text{and} \quad A^i = g^{ij} A_j \quad \text{where} \quad A_i \equiv \underline{A} \cdot \hat{e}_i \quad \text{and} \quad A^i \equiv \underline{A} \cdot \hat{e}^i \quad (5.5)$$

In addition, the determinant of the metric tensor is used to define cross products and curls<sup>7</sup>.

$$(\underline{A} \times \underline{B})^i = \frac{\varepsilon^{ijk}}{\sqrt{g}} A_j B_k \quad \text{and} \quad (\nabla \times \underline{A})^i = \frac{\varepsilon^{ijk}}{\sqrt{g}} \frac{\partial}{\partial u^j} A_k \quad \text{where} \quad g \equiv \det \underline{\underline{g}} \quad (5.6)$$

Explicit forms of the basis vectors and metric tensor can be found in the appendix of Lysak's 2004 paper[58]. At present, it's sufficient to note the mapping between Lysak's basis vectors and the usual dipole unit vectors.

$$\hat{x} = \frac{1}{\sqrt{g^{11}}} \hat{e}^1 \quad \hat{y} = \frac{1}{\sqrt{g^{22}}} \hat{e}^2 \quad \hat{z} = \frac{1}{\sqrt{g^{33}}} \hat{e}^3 \quad (5.7)$$

<sup>643</sup> TODO: Do these need to be written out? Referring people to the code, which will be in a public Git repository, is also a possibility.

The basis vectors can also be mapped to the spherical unit vectors, though Equation (5.8) is valid only at the ionospheric boundary.

$$\hat{\theta} = \frac{1}{\sqrt{g_{11}}} \hat{e}_1 \quad \hat{\phi} = \frac{1}{\sqrt{g_{22}}} \hat{e}_2 \quad \hat{r} = \frac{1}{\sqrt{g_{33}}} \hat{e}_3 \quad (5.8)$$

---

<sup>6</sup>The symbol  $\delta_j^i$  is the Kronecker delta; the present work also makes use of the Levi-Civita symbol  $\varepsilon^{ijk}$  and Einstein's convention of implied summation over repeated indeces[23].

<sup>7</sup>The square root of the determinant of the metric tensor is called the Jacobian. It's sometimes denoted using the letter  $J$ , which is reserved for current in the present work.

645 The coordinates converge at the equatorial ionosphere, so an inner boundary is necessary  
646 to maintain finite grid spacing. It's typically placed at  $L = 2$ . The outer boundary is  
647 at  $L = 10$ . The dipole approximation of Earth's magnetic field is tenuous at the outer  
648 boundary (particularly on the dayside); however, in practice, wave activity is localized  
649 inside  $L \sim 7$ . The grid is spaced uniformly in  $u^1$ , which gives finer resolution close to  
650 Earth and coarser resolution at large distances.

651 Spacing in  $u^3$  is set by placing grid points along the outermost field line. The points are  
652 closest together at the ionosphere, and grow towards the equator. The spacing increases  
653 in a geometric fashion, typically by 3%.

654 Typically, Tuna uses a grid 150 points in  $u^1$  by 350 points in  $u^3$ . The result is a resolution  
655 on the order of 10 km at the ionosphere, which increases to the order of 10<sup>3</sup> km at the  
656 midpoint of the outermost field line.

657 There are no grid points in  $u^2$  due to the two-and-a-half-dimensional nature of the  
658 model. Fields are assumed to vary as  $\exp(imu^2)$  — equally,  $\exp(im\phi)$  — so derivatives  
659 with respect to  $u^2$  are equivalent to a factor of  $im$ . In effect, the real component of  
660 each field is azimuthally in phase with the (purely real) driving, while imaginary values  
661 represent behavior that is azimuthally offset.

662 The simulation's time step is set based on the grid spacing. As is the convention,  $\delta t$  is  
663 set to match the smallest Alfvén zone crossing time, scaled down by a Courant factor  
664 (typically 0.1). It bears noting that the smallest crossing time need not correspond to  
665 the smallest zone; the Alfvén speed peaks several thousand kilometers above Earth's  
666 surface, in the so-called Ionospheric Alfvén Resonator[61]. A typical time step is on the  
667 order of 10<sup>-5</sup> s.

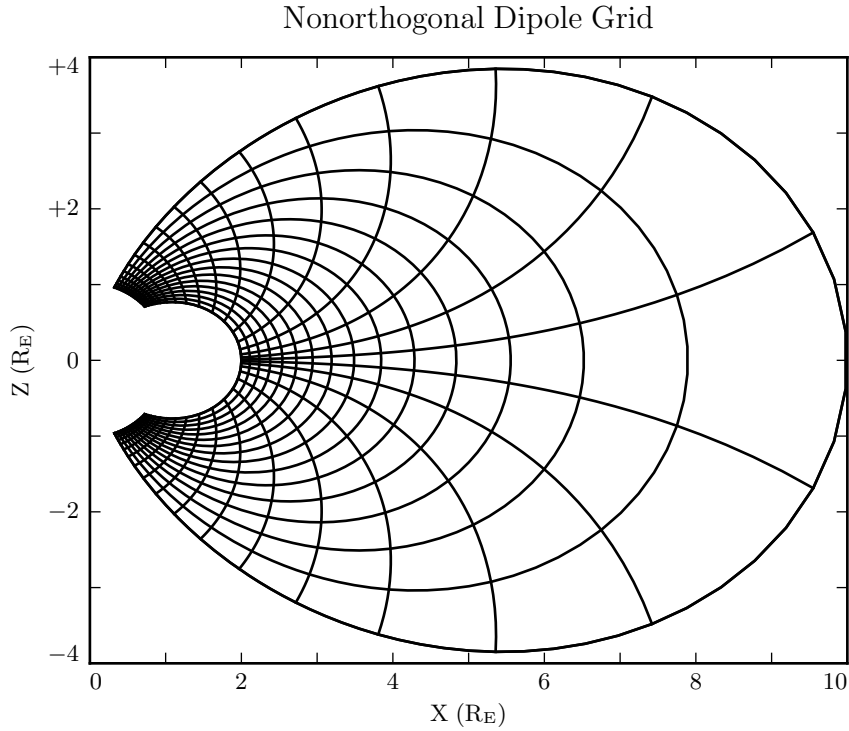


Figure 5.1: The model’s nonorthogonal dipole grid. Every fifth point is shown in each direction. The high concentration of grid points near Earth’s equator is a consequence of the coordinate system, which converges at the equatorial ionosphere. Earth (not shown) is centered at the origin with unit radius.

668 **5.2 Physical Parameter Profiles**

Tuna models Earth’s magnetic field to be an ideal dipole, so the zeroth-order field strength is written in the usual form:

$$\underline{B}_0 = 3.1 \times 10^4 \text{ nT} \left( \frac{R_E}{r} \right)^3 \left( 2 \cos \theta \hat{r} - \sin \theta \hat{\theta} \right) \quad (5.9)$$

Number density is taken to be the sum of an inverse-radial-dependent auroral profile and a plasmaspheric profile dependent on the  $L$ -shell[61]:

$$n = n_{AZ} \frac{r_{AZ}}{r} + n_{PS} \exp\left(\frac{-L}{L_{PS}}\right) \left( \frac{1}{2} - \frac{1}{2} \tanh \frac{L - L_{PP}}{\delta L_{PP}} \right) \quad (5.10)$$

669 Where typical values are shown in Table 5.1.

Table 5.1: Typical Parameters for the Tuna Density Profile

Variable	Value	Description
$L_{PS}$	1.1	Scale $L$ of the plasmasphere.
$L_{PP}$	4.0	Location of the plasmapause.
$\delta L_{PP}$	0.1	Thickness of the plasmapause.
$n_{AZ}$	$10 / \text{cm}^3$	Number density at the base of the auroral zone.
$n_{PS}$	$10^4 / \text{cm}^3$	Number density at the base of the plasmasphere.
$r_{AZ}$	$1 \text{ R}_E$	Scale height of the auroral density distribution.

The perpendicular component of the electric tensor,  $\epsilon_{\perp}$ , is computed based on Kelley's[48] tabulated low-density values,  $\epsilon_K$ , which are adjusted to take into account the effects of high density in the plasmapause.

$$\epsilon_{\perp} = \epsilon_K + \frac{Mn}{B_0^2} \quad (5.11)$$

670 Where  $M$  is the mean molecular mass, which is large ( $\sim 28 \text{ u}$ ) at 100 km altitude, then  
671 drops quickly (down to 1 u by  $\sim 1000 \text{ km}$ )[61].

672 The Alfvén speed profile is computed from the perpendicular electric constant in the  
673 usual way,  $v_A^2 \equiv \frac{1}{\mu_0 \epsilon_{\perp}}$ . This form takes into account the effect of the displacement  
674 current, which becomes important in regions where the Alfvén speed approaches the  
675 speed of light.

676 While the density profile is held constant for all runs discussed in the present work,  
677 the Alfvén speed profile is not. Four different profiles are used for the low-density

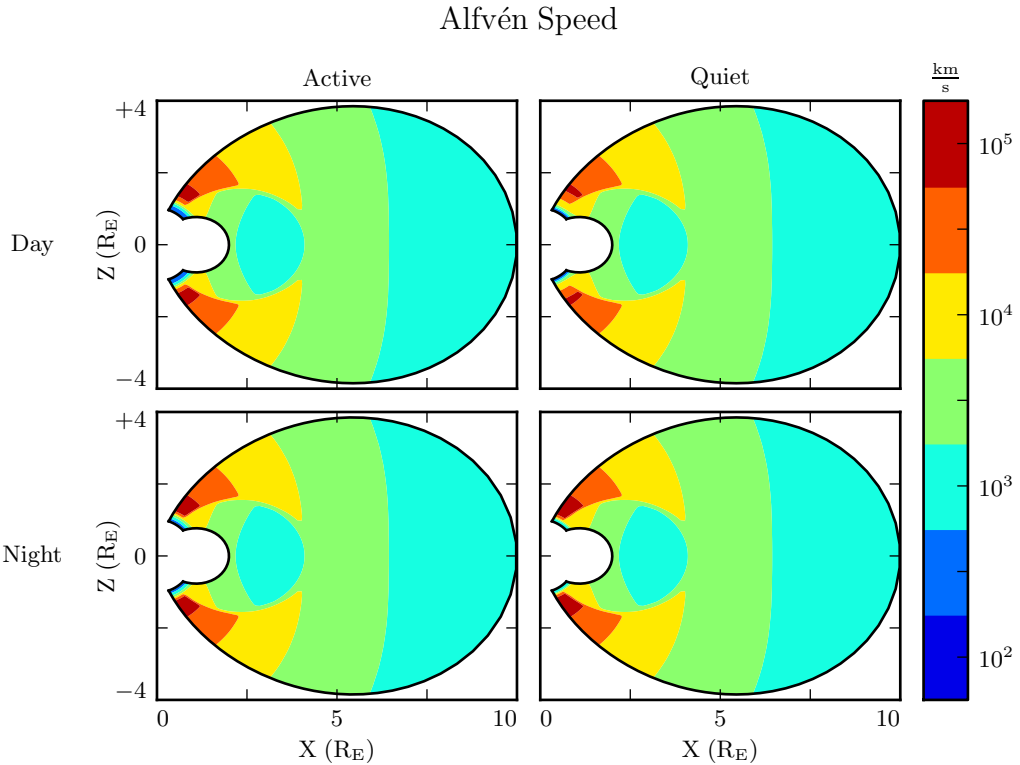


Figure 5.2: Alfvén speed profiles are based on low-density values tabulated by Kelley[48]. They are adjusted to take into account the density of the plasmapause and mass loading near the Earthward boundary.

678 perpendicular electric constant  $\epsilon_K$ , corresponding to the differing ionospheric conditions  
 679 between the dayside and the nightside, and between the high and low points in the  
 680 solar cycle. These differences are visible in Figure 5.2, particularly in the size of the  
 681 ionospheric Alfvén resonator (the peak in Alfvén speed in the high-latitude ionosphere).

682 **TODO:** Runs are only carried out for day and night... is it even worth showing the  
 683 flank profile?

684 Ionospheric conductivity profiles are also based on values tabulated by Kelley, adjusted  
 685 by Lysak[61] to take into account the abundance of heavy ions near the Earthward  
 686 boundary. Pedersen, Hall, and parallel conductivities are each resolved by altitude, as  
 687 shown in Figure 5.3.

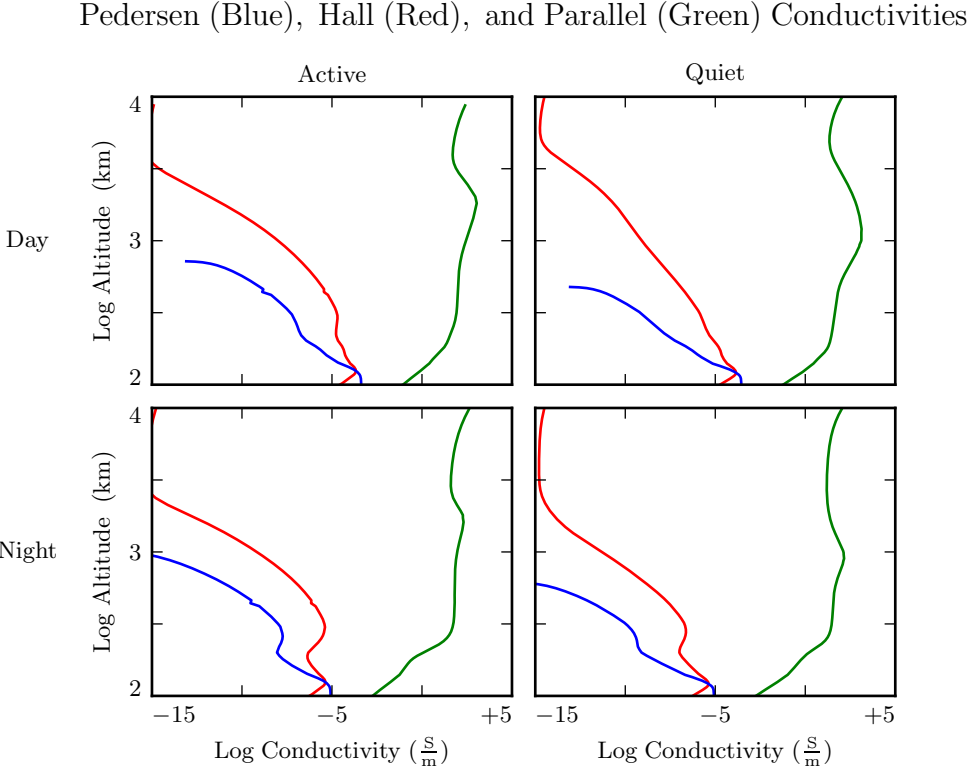


Figure 5.3: Ionospheric conductivity profiles are adapted by Lysak[61] from Kelley's tabulated values[48]. These profiles allow Tuna to simulate magnetosphere-ionosphere coupling under a variety of conditions.

688 Tuna's physical parameter profiles are static over the course of each run. Even so-called  
 689 ultra low frequency waves like Pc4 pulsations are fast compared to convective timescales  
 690 in the magnetosphere.

### 691 5.3 Driving

692 Models similar to Tuna have traditionally been driven using compression at the outer  
 693 boundary[58, 61, 100, 101]. Such driving acts as a proxy for solar wind compression,  
 694 Kelvin-Helmholtz effects at the magnetopause, and so on. However, because of the

695 constraints imposed by the dispersion relation for Alfvén waves<sup>8</sup>, simulations driven from  
696 the outer boundary are constrained to the consideration of waves with low azimuthal  
697 modenumber (equivalently, large azimuthal wavelength).

698 This issue is demonstrated in Figure 5.4. At low modenumber, energy delivered at  
699 the outer boundary propagates across field lines in order to stimulate resonances in  
700 the inner magnetosphere. However, as modenumber increases, Alfvén waves become  
701 increasingly guided, and the inner magnetosphere is unaffected by perturbations at the  
702 outer boundary.

703 In order to simulate high-modenumber Alfvén waves in the inner magnetosphere — such  
704 as giant pulsations — a new driving mechanism is necessary. Perturbation of the ring  
705 current is a natural choice, as Alfvén waves in the Pc4 range are known to interact with  
706 ring current particles through drift and drift-bounce resonances. The ring current is a  
707 dynamic region, particularly during and after geomagnetic storms; it's easy to imagine  
708 the formation of localized inhomogeneities.

709 In order to estimate an appropriate magnitude for perturbations of the ring current,  
710 the Sym-H storm index is used. The index is measured once per minute, and so cannot  
711 directly detect ring current modulations in the Pc4 frequency range. Instead, the index  
712 is transformed into the frequency domain, allowing a fit of its pink noise<sup>9</sup>.

713 **TODO: Sym-H is basically the same as Dst[99].**

714 As shown in Figure 5.5, a Fourier transform of the Sym-H index (taken here from the  
715 June 2013 storm) suggests that magnetic field perturbations at Earth's surface due to  
716 ring current activity in the Pc4 frequency range could be up to the order of  $10^{-2}$  nT.  
717 Supposing that the ring current is centered around  $5 R_E$  geocentric, that corresponds to  
718 a current on the order of 0.1 MA. Tuna's driving is spread using a Gaussian profile in  
719  $u^1$  (typically centered at  $L = 5$ ) and  $u^3$  (typically centered just off the equator), with a  
720 characteristic area of  $1 R_E^2$ ; this gives a current density on the order of  $10^{-4} \mu\text{A}/\text{m}^2$ .

---

<sup>8</sup>See Section 4.4.

<sup>9</sup>Pink noise, also called  $\frac{1}{f}$  noise, refers to the power law decay present in the Fourier transforms of all manner of physical signals.

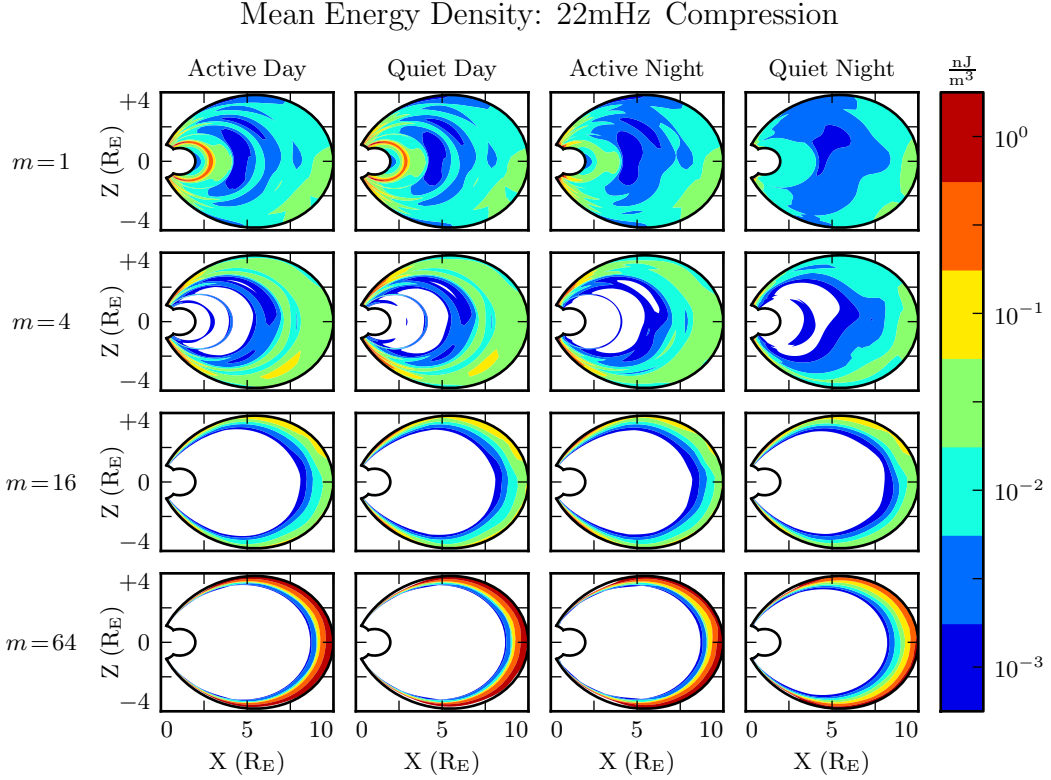


Figure 5.4: Each cell presents the mean energy density over the course of a 300 s run, as a function of position, due to compressional driving at the outer boundary. Azimuthal modenumber varies by row, and ionospheric conditions vary by column. For runs with small azimuthal modenumber, it's clear that energy is able to propagate across field lines and stimulate wave activity in the inner magnetosphere. When the modenumber is large, energy is unable to penetrate to the inner magnetosphere. Notably, the large values on the bottom row should be taken with a grain of salt; it's not clear that the model's results are reliable when waves are continuously forced against the boundary.

- 721 TODO: Admittedly, estimating the strength of localized perturbations using Sym-H —  
 722 an index averaged over the entire globe — is a bit of a kludge.
- 723 In situ observations of Pc4 pulsations and giant pulsations have shown waves with  
 724 modenumbers across the range  $1 \lesssim m \lesssim 100$ [17, 18, 90]. Simulations are carried out  
 725 across that range, corresponding to ring current perturbations with azimuthal extent as  
 726 small as  $0.5 R_E$ .

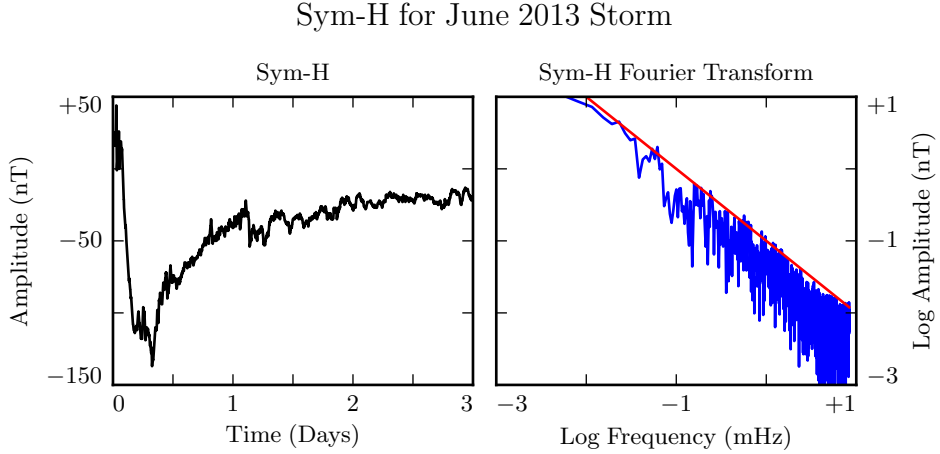


Figure 5.5: The Sym-H storm index[71] measures magnetic perturbations on Earth’s surface due to ring current activity. The amplitude of oscillations in the Pc4 range is estimated by fitting the pink noise in its Fourier transform.

727 TODO: Driving is delivered in the azimuthal component of the current only.

728 TODO: Driving is sinusoidal.

729 TODO: In case it’s not clear: Chapter 7 discusses ONLY simulations using ring current  
730 driving. The only compressional driving we look at is Figure 5.4.

731 TODO: Driving on the dayside is centered at  $L = 5$ . On the nightside, due to the  
732 increased Alfvén speed, it’s moved out to  $L = 6$ . The Alfvén bounce time at  $L = 5$  on  
733 the nightside is well above the Pc4 range.

## 734 5.4 Maxwell’s Equations

735 Tuna simulates the evolution of electromagnetic waves in accordance with Ampère’s  
736 law and Faraday’s law. Computation is carried out on a Yee grid[105]: electric fields  
737 and magnetic fields are offset by half a time step, and each field component is defined  
738 on either odd or even grid points in each dimension to ensure that curls are computed  
739 using centered differences.

The Ohmic current in Ampère's law is replaced with  $\underline{\sigma} \cdot \underline{E}$  per Kirchhoff's formulation of Ohm's law. Then, taking  $\underline{J}$  to represent the driving current discussed in Section 5.3, Maxwell's equations can be written

$$\frac{\partial}{\partial t} \underline{B} = -\nabla \times \underline{E} \quad \underline{\epsilon} \cdot \frac{\partial}{\partial t} \underline{E} = \frac{1}{\mu_0} \nabla \times \underline{B} - \underline{J} - \underline{\sigma} \cdot \underline{E} \quad (5.12)$$

It is convenient to introduce shorthand for the curl of each field:  $\underline{C} \equiv \nabla \times \underline{E}$  and  $\underline{F} \equiv \nabla \times \underline{B} - \mu_0 \underline{J}$ . Or, recalling Equation (5.6),

$$C^i = \frac{\varepsilon^{ijk}}{\sqrt{g}} \frac{\partial}{\partial u^j} E_k \quad F^i = \frac{\varepsilon^{ijk}}{\sqrt{g}} \frac{\partial}{\partial u^j} B_k - J^i \quad (5.13)$$

In these terms, Faraday's law can simply be written:

$$\frac{\partial}{\partial t} B^i = -C^i \quad (5.14)$$

Writing each component out explicitly, and using the metric tensor (per Equation (5.5)) to eliminate contravariant magnetic field components<sup>10</sup>, Equation (5.14) becomes:

$$\begin{aligned} B_1 &\leftarrow B_1 - g_{11} \delta t C^1 - g_{13} \delta t C^3 \\ B_2 &\leftarrow B_2 - g_{22} \delta t C^2 \\ B_3 &\leftarrow B_3 - g_{31} \delta t C^1 - g_{33} \delta t C^3 \end{aligned} \quad (5.15)$$

<sup>740</sup>Note that the  $\leftarrow$  operator is used in Equation (5.15) to indicate assignment, rather than  
<sup>741</sup>equality. Terms on the left are new, while those on the right are old.

Unlike Faraday's law, Ampère's law cannot be trivially solved. Not only does the derivative of  $\underline{E}$  depend on its own future value, but the crosswise and azimuthal components of the equation are coupled by the Hall terms in the conductivity tensor. Fortunately,

---

<sup>10</sup>Fields are stored only in terms of their covariant components, and curls in terms of their contravariant components. This reduces Tuna's memory footprint (since each field need not be stored twice) as well as its computational cost (since time need not be spent rotating between bases). As a result, Tuna's solutions to Maxwell's equations are linear expressions whose coefficients are a mishmash of physical constants and geometric factors. To save time, each coefficient is computed once and stored, rather than being multiplied out from scratch with each time step.

the electric tensor can be inverted, allowing a solution by integrating factors:

$$\underline{\epsilon} \cdot \frac{\partial}{\partial t} \underline{E} = \frac{1}{\mu_0} \underline{F} - \underline{\sigma} \cdot \underline{E} \quad \text{becomes} \quad \left( \underline{\Omega} + \underline{\mathbb{I}} \frac{\partial}{\partial t} \right) \cdot \underline{E} = \underline{V}^2 \cdot \underline{F} \quad (5.16)$$

Where  $\underline{\mathbb{I}}$  is the identity tensor and in  $x$ - $y$ - $z$  coordinates<sup>11</sup>,

$$\underline{V}^2 \equiv \frac{1}{\mu_0} \underline{\epsilon}^{-1} = \begin{bmatrix} v_A^2 & 0 & 0 \\ 0 & v_A^2 & 0 \\ 0 & 0 & c^2 \end{bmatrix} \quad \text{and} \quad \underline{\Omega} \equiv \underline{\epsilon}^{-1} \cdot \underline{\sigma} = \begin{bmatrix} \frac{\sigma_P}{\epsilon_{\perp}} & \frac{-\sigma_H}{\epsilon_{\perp}} & 0 \\ \frac{\sigma_H}{\epsilon_{\perp}} & \frac{\sigma_P}{\epsilon_{\perp}} & 0 \\ 0 & 0 & \frac{\sigma_0}{\epsilon_0} \end{bmatrix} \quad (5.17)$$

Multiplying through by  $\exp(\underline{\Omega} t)$  and applying the product rule, Equation (5.16) becomes<sup>12</sup>

$$\frac{\partial}{\partial t} \left( \exp(\underline{\Omega} t) \cdot \underline{E} \right) = \exp(\underline{\Omega} t) \cdot \underline{V}^2 \cdot \underline{F} \quad (5.18)$$

Equation (5.18) can then be integrated over a small time step  $\delta t$  and expressed in terms of the assignment operator introduced in Equation (5.15).

$$\underline{E} \leftarrow \exp(-\underline{\Omega} \delta t) \cdot \underline{E} + \delta t \exp(-\underline{\Omega} \frac{\delta t}{2}) \cdot \underline{V}^2 \cdot \underline{F} \quad (5.19)$$

The tensor exponential can be evaluated by splitting  $\underline{\Omega}$  into the sum of its diagonal and Hall components<sup>13</sup>. The Hall exponential condenses into sines and cosines, giving a rotation around the magnetic field line:

$$\underline{E} \leftarrow \exp(-\underline{\Omega}' \delta t) \cdot \underline{R}_z \left( \frac{-\sigma_H \delta t}{\epsilon_{\perp}} \right) \cdot \underline{E} + \delta t \underline{V}^2 \cdot \exp(-\underline{\Omega}' \frac{\delta t}{2}) \cdot \underline{R}_z \left( \frac{-\sigma_H \delta t}{2\epsilon_{\perp}} \right) \cdot \underline{F} \quad (5.20)$$

---

<sup>11</sup>Note the parallel component of the present definition of  $\underline{\Omega}$  differs slightly from that used in Chapter 4, due to the present neglect of inertial effects; see Chapter 6.

<sup>12</sup>Tensor exponentiation is analogous to scalar exponentiation[37]:  $\exp(\underline{T}) \equiv \sum_n \frac{1}{n!} \underline{T}^n$ .

<sup>13</sup>For tensors,  $\exp(\underline{S} + \underline{T}) = \exp(\underline{S}) \exp(\underline{T})$  as long as  $\underline{S} \cdot \underline{T} = \underline{T} \cdot \underline{S}$ .

Where

$$\underline{\underline{R}}_z(\theta) = \begin{bmatrix} \cos \theta & -\sin \theta & 0 \\ \sin \theta & \cos \theta & 0 \\ 0 & 0 & 1 \end{bmatrix} \quad \text{and} \quad \underline{\underline{\Omega}}' \equiv \begin{bmatrix} \frac{\sigma_P}{\epsilon_{\perp}} & 0 & 0 \\ 0 & \frac{\sigma_P}{\epsilon_{\perp}} & 0 \\ 0 & 0 & \frac{\sigma_0}{\epsilon_0} \end{bmatrix} \quad (5.21)$$

The parallel component of term of Equation (5.20) is simply

$$E_z \leftarrow E_z \exp\left(\frac{-\sigma_0 \delta t}{\epsilon_0}\right) + c^2 \delta t F_z \exp\left(\frac{-\sigma_0 \delta t}{2\epsilon_0}\right) \quad (5.22)$$

Or, using Equation (5.7) to map to the covariant basis,

$$E_3 \leftarrow E_3 \exp\left(\frac{-\sigma_0 \delta t}{\epsilon_0}\right) + c^2 \delta t (g_{31} F^1 + g_{33} F^3) \exp\left(\frac{-\sigma_0 \delta t}{2\epsilon_0}\right) \quad (5.23)$$

<sup>742</sup> Tuna's conductivity profile gives a minimum value of  $\frac{\sigma_0 \delta t}{\epsilon_0}$  on the order of  $10^3$ , making  
<sup>743</sup>  $\exp\left(\frac{-\sigma_0 \delta t}{\epsilon_0}\right)$  far too small to be stored in a double precision variable<sup>14</sup>. That is, this  
<sup>744</sup> model takes  $E_3$  (and, proportionally,  $E_z$ ) to be uniformly zero. This issue is revisited  
<sup>745</sup> in Chapter 6.

The perpendicular components of Equation (5.20) give the expressions:

$$\begin{aligned} E_1 + \frac{g^{13}}{g^{11}} E_3 &\leftarrow E_1 \cos\left(\frac{-\sigma_H \delta t}{\epsilon_{\perp}}\right) \exp\left(\frac{-\sigma_P \delta t}{\epsilon_{\perp}}\right) \\ &\quad + E_2 \sin\left(\frac{-\sigma_H \delta t}{\epsilon_{\perp}}\right) \exp\left(\frac{-\sigma_P \delta t}{\epsilon_{\perp}}\right) \sqrt{\frac{g^{22}}{g^{11}}} \\ &\quad + E_3 \cos\left(\frac{-\sigma_H \delta t}{\epsilon_{\perp}}\right) \exp\left(\frac{-\sigma_P \delta t}{\epsilon_{\perp}}\right) \frac{g^{13}}{g^{11}} \\ &\quad + F^1 \cos\left(\frac{-\sigma_H \delta t}{2\epsilon_{\perp}}\right) \exp\left(\frac{-\sigma_P \delta t}{2\epsilon_{\perp}}\right) \frac{v_A^2 \delta t}{g^{11}} \\ &\quad + F^2 \sin\left(\frac{-\sigma_H \delta t}{2\epsilon_{\perp}}\right) \exp\left(\frac{-\sigma_P \delta t}{2\epsilon_{\perp}}\right) \frac{v_A^2 \delta t}{\sqrt{g^{11} g^{22}}} \end{aligned} \quad (5.24)$$

---

<sup>14</sup>Not coincidentally,  $\frac{\sigma_0}{\epsilon_0}$  can also be written  $\frac{\omega_P^2}{\nu}$ . At the ionosphere, the collision frequency  $\nu$  is fast compared to field line resonance timescales, but it's still slow compared to the plasma frequency.

and

$$\begin{aligned}
E_2 \leftarrow & -E_1 \sin\left(\frac{-\sigma_H \delta t}{\epsilon_{\perp}}\right) \exp\left(\frac{-\sigma_P \delta t}{\epsilon_{\perp}}\right) \sqrt{\frac{g^{11}}{g^{22}}} \\
& + E_2 \cos\left(\frac{-\sigma_H \delta t}{\epsilon_{\perp}}\right) \exp\left(\frac{-\sigma_P \delta t}{\epsilon_{\perp}}\right) \\
& - E_3 \sin\left(\frac{-\sigma_H \delta t}{\epsilon_{\perp}}\right) \exp\left(\frac{-\sigma_P \delta t}{\epsilon_{\perp}}\right) \frac{g^{13}}{\sqrt{g^{11} g^{22}}} \\
& - F^1 \sin\left(\frac{-\sigma_H \delta t}{2\epsilon_{\perp}}\right) \exp\left(\frac{-\sigma_P \delta t}{2\epsilon_{\perp}}\right) \frac{v_A^2 \delta t}{\sqrt{g^{11} g^{22}}} \\
& + F^2 \cos\left(\frac{-\sigma_H \delta t}{2\epsilon_{\perp}}\right) \exp\left(\frac{-\sigma_P \delta t}{2\epsilon_{\perp}}\right) \frac{v_A^2 \delta t}{g^{22}}
\end{aligned} \tag{5.25}$$

746 The  $E_3$  terms in Equations (5.24) and (5.25) can be ignored at present. They are  
747 revisited in Chapter 6.

748 It bears recalling that the driving current is defined as part of  $\underline{F}$ , per Equation (5.13).  
749 When the driving current is purely azimuthal ( $J^1 = J^3 = 0$ ), the driving is in principle  
750 applied to both the poloidal and the toroidal electric fields through  $F^2$ . However,  
751 in practice, the driving applied to the toroidal electric field is vanishingly small. The  
752 driving current  $J^2$  is localized around  $5 R_E$  geocentric, and  $\exp\left(\frac{-\sigma_P \delta t}{2\epsilon_{\perp}}\right)$  drops off quickly  
753 with altitude.

## 754 5.5 Boundary Conditions

755 Dirichlet and Neumann boundary conditions are applied to the electric field components  
756 and magnetic field components respectively. That is, electric fields are forced to go to  
757 zero at the inner and outer boundaries, and magnetic fields are forced to have a zero  
758 derivative normal to the inner and outer boundaries.

759 These boundary conditions can in principle cause nonphysical reflections at the bound-  
760 ary<sup>15</sup>. However, in practice, wave activity is concentrated well within the simulation  
761 domain. Simulation results are robust under an exchange of Dirichlet and Neumann

---

<sup>15</sup>See, for example, the bottom row of Figure 5.4.

762 boundary conditions (though a self-inconsistent set of boundary condidtions, such as  
 763 applying Neumann boundary conditions to  $B_1$  but Dirichlet boundary conditions to  $B_3$ ,  
 764 quickly causes instability).

765 The Earthward boundary conditions are as follows.

Between the top of the neutral atmosphere and the bottom of the ionosphere, the model includes a thin, horizontal current sheet representing the ionosphere's  $E$  layer[58]. By integrating Ampère's law over the layer, it can be shown[27] that the horizontal electric field values at the edge of the grid are determined by the jump in the horizontal magnetic fields:

$$\underline{\underline{\Sigma}} \cdot \underline{E} = \frac{1}{\mu_0} \lim_{\delta r \rightarrow 0} \left[ \hat{r} \times \underline{B} \right]_{R_I - \delta r}^{R_I + \delta r} \quad (5.26)$$

The integrated conductivity tensor  $\underline{\underline{\Sigma}}$  can be written in  $\theta$ - $\phi$  coordinates as[58]:

$$\underline{\underline{\Sigma}} \equiv \begin{bmatrix} \frac{\Sigma_0 \Sigma_P}{\Sigma_0 \cos^2 \alpha + \Sigma_P \sin^2 \alpha} & \frac{-\Sigma_0 \Sigma_H}{\Sigma_0 \cos^2 \alpha + \Sigma_P \sin^2 \alpha} \\ \frac{\Sigma_0 \Sigma_H}{\Sigma_0 \cos^2 \alpha + \Sigma_P \sin^2 \alpha} & \Sigma_P + \frac{\Sigma_H^2 \sin^2 \alpha}{\Sigma_0 \cos^2 \alpha + \Sigma_P \sin^2 \alpha} \end{bmatrix} \quad (5.27)$$

766 Where  $\alpha$  is the angle between the magnetic field and the vertical direction, given by  
 767  $\cos \alpha \equiv \frac{-2 \cos \theta}{\sqrt{1+3 \cos^2 \theta}}$ , and  $\Sigma_P$ ,  $\Sigma_H$ , and  $\Sigma_0$  are the height-integrated Pedersen, Hall,  
 768 and parallel conductivities respectively. Their values are determined by integrating  
 769 Kelley's[48] conductivity profiles from Earth's surface to the ionospheric boundary; val-  
 770 ues are shown in Table 5.2.

Table 5.2: Integrated Atmospheric Conductivity (S)

	$\Sigma_0$	$\Sigma_P$	$\Sigma_H$
Active Day	424	0.65	6.03
Quiet Day	284	0.44	4.02
Active Night	9	0.01	0.12
Quiet Night	9	0.01	0.12

An expression for the horizontal electric fields at the boundary can be obtained by inverting Equation (5.26). After mapping to covariant coordinates per Equation (5.8), and taking  $\Sigma \equiv \det \underline{\underline{\Sigma}}$ ,

$$\begin{aligned} E_1 &\leftarrow \frac{1}{\mu_0 \Sigma} \lim_{\delta r \rightarrow 0} \left[ -\Sigma_{\theta\phi} B_1 - \sqrt{\frac{g_{11}}{g_{22}}} \Sigma_{\phi\phi} B_2 \right]_{R_I-\delta r}^{R_I+\delta r} \\ E_2 &\leftarrow \frac{1}{\mu_0 \Sigma} \lim_{\delta r \rightarrow 0} \left[ \sqrt{\frac{g_{22}}{g_{11}}} \Sigma_{\theta\theta} B_1 + \Sigma_{\phi\theta} B_2 \right]_{R_I-\delta r}^{R_I+\delta r} \end{aligned} \quad (5.28)$$

771 In order to compute the atmospheric magnetic field, a scalar magnetic potential ( $\Psi$   
772 such that  $\underline{B} = \nabla\Psi$ ) is computed as a linear combination of harmonics. The neutral  
773 atmosphere is considered to be a perfect insulator, giving  $\nabla \times \underline{B} = 0$ . Combined with  
774  $\nabla \cdot \underline{B} = 0$  (per Maxwell's equations),  $\Psi$  satisfies Laplace's equation,  $\nabla^2\Psi = 0$ .

Laplace's equation can be solved analytically; however, a numerical solution is preferable to ensure orthonormality on a discrete and incomplete<sup>16</sup> grid. After separating out the radial and azimuthal dependence in the usual way, the latitudinal component of Laplace's equation can be written in terms of  $s \equiv -\sin^2\theta$ :

$$(4s^2 + 4s) \frac{d^2}{ds^2} Y_\ell + (4 + 6s) \frac{d}{ds} Y_\ell - \frac{m^2}{s} Y_\ell = \ell(\ell+1) Y_\ell \quad (5.29)$$

Using centered differences to linearize the derivatives, Equation (5.29) becomes a system of coupled linear equations, one per field line. It can be solved numerically for eigenvalues  $\ell(\ell+1)$  and eigenfunctions  $Y_\ell$ <sup>17</sup>. In terms of the harmonics  $Y_\ell$ ,  $\Psi$  between the Earth's surface and the top of the atmosphere can be written using eigenweights  $a_\ell$  and  $b_\ell$ :

$$\Psi = \sum_\ell \left( a_\ell r^\ell + b_\ell r^{-\ell-1} \right) Y_\ell \quad (5.30)$$

---

<sup>16</sup>As discussed in Section 5.1, the grid is constrained to finite  $L$ , which excludes the equator as well as the poles.

<sup>17</sup>Solving Laplace's equation analytically results in spherical harmonics indexed by both  $\ell$  and  $m$ , the separation constants for  $\theta$  and  $\phi$  respectively. In two and a half dimensions,  $\phi$  is not explicitly resolved, so  $m$  is set manually.

As a boundary condition for  $\Psi$ , Earth is assumed to be a perfect conductor. This forces the magnetic field at Earth's surface to be horizontal; that is,  $B_r = \frac{\partial}{\partial r}\Psi = 0$ . Noting that solutions to Laplace's equation are orthonormal, each element of the sum in Equation (5.30) must be independently zero at  $R_E$ . This allows the coefficients  $a_\ell$  and  $b_\ell$  to be expressed in terms of one another.

$$b_\ell = \frac{\ell}{\ell+1} R_E^{2\ell+1} a_\ell \quad (5.31)$$

The current sheet at the top of the atmosphere is assumed to be horizontal, so the radial component of the magnetic field must be the same just above and just below it. Taking the radial derivative of Equation (5.30) at the top of the atmosphere, and eliminating  $b_\ell$  with Equation (5.31), gives

$$B_r = \sum_\ell \ell a_\ell R_I^{\ell-1} \left(1 - \lambda^{2\ell+1}\right) Y_\ell \quad \text{where} \quad \lambda \equiv \frac{R_E}{R_I} \sim 0.975 \quad (5.32)$$

The summation can be collapsed by “integrating” over a harmonic<sup>18</sup>. Inverse harmonics can be obtained by inverting the eigenvector matrix. Then  $Y_\ell \cdot Y_{\ell'}^{-1} = \delta_{\ell\ell'}$  by construction.

$$a_\ell = \frac{1}{\ell R_I^{\ell-1}} \frac{B_r \cdot Y_\ell^{-1}}{1 - \lambda^{2\ell+1}} \quad (5.33)$$

Combining Equations (5.30), (5.31), and (5.33) allows the expression of  $\Psi$  at the top and bottom of the atmosphere as a linear combination of radial magnetic field components at the bottom of the ionosphere.

$$\begin{aligned} \Psi_E &= \sum_\ell Y_\ell \frac{R_I}{\ell(\ell-1)} \frac{(2\ell-1)\lambda^\ell}{1-\lambda^{2\ell+1}} B_r \cdot Y_\ell^{-1} \\ \Psi_I &= \sum_\ell Y_\ell \frac{R_I}{\ell(\ell-1)} \frac{(\ell-1)+\ell\lambda^{2\ell+1}}{1-\lambda^{2\ell+1}} B_r \cdot Y_\ell^{-1} \end{aligned} \quad (5.34)$$

---

<sup>18</sup>Because the functions are defined on a discrete grid, their inner product is not an integral, but a sum:  $B_r \cdot Y_\ell^{-1} \equiv \sum_i B_r[i] Y_\ell^{-1}[i]$ .

Horizontal magnetic fields are obtained by taking derivatives of  $\Psi$ .

$$B_1 = \frac{\partial}{\partial u^1} \Psi \quad B_2 = \frac{\partial}{\partial u^2} \Psi \quad (5.35)$$

- 775 Horizontal magnetic field values at the top of the atmosphere are used to impose bound-  
776 ary conditions on the electric fields at the bottom of the ionosphere, per Equation (5.28).  
777 Those at Earth's surface are valuable because they allow a direct comparison between  
778 model output and ground magnetometer data, after being mapped to physical coordi-  
779 nates per Equation (5.8).

780 **Chapter 6**

781 **Electron Inertial Effects**

782 As laid out in Chapter 5, Tuna resolves neither parallel currents nor parallel electric  
783 fields. This is unfortunate; parallel electric fields generated by kinetic and inertial Alfvén  
784 waves (including fundamental field line resonances[79, 95]) are a topic of particular  
785 interest in the study of auroral particle precipitation.

Parallel currents and electric fields can be added to Tuna through the consideration of electron inertial effects in Ohm's law:

$$0 = \sigma_0 E_z - J_z \quad \text{becomes} \quad \frac{1}{\nu} \frac{\partial}{\partial t} J_z = \sigma_0 E_z - J_z \quad (6.1)$$

With the addition of the electron inertial term, it is necessary to track the parallel current independent of the parallel electric field<sup>1</sup>. Solving by integrating factors<sup>2</sup> gives

$$J_3 \leftarrow J_3 \exp(-\nu \delta t) + \delta t \frac{ne^2}{m_e} E_3 \exp\left(-\nu \frac{\delta t}{2}\right) \quad (6.2)$$

---

<sup>1</sup>The parallel current  $J_z$  is defined on the same points of the Yee grid as  $E_z$ . It is offset in time by half of a time step.

<sup>2</sup>The integrating factors technique is laid out explicitly for Ampère's law in Section 5.4.

From there, the parallel electric field can be updated directly; Equation (5.23) is replaced by the following:

$$E_3 \leftarrow E_3 + c^2 \delta t (g_{31} F^1 + g_{33} F^3) - \frac{\delta t}{\epsilon_0} J_3 \quad (6.3)$$

786 The present section explores the complications that arise from the addition of the elec-  
 787 tron inertial term to Ohm's law, as well as a few results that may be gleaned despite  
 788 those complications. Notably — for reasons discussed in Section 6.3 — the results  
 789 presented in Chapter 7 do not make use of the electron inertial term.

## 790 6.1 The Boris Factor

With the addition of the electron inertial term, a cyclical dependence appears between Ampère's law and Ohm's law:

$$\frac{\partial}{\partial t} E_z \sim -\frac{1}{\epsilon_0} J_z \quad \text{and} \quad \frac{\partial}{\partial t} J_z \sim \frac{ne^2}{m_e} E_z \quad \text{so} \quad \frac{\partial^2}{\partial t^2} E_z \sim -\omega_P^2 E_z \quad (6.4)$$

791 That is, electron inertial effects come hand in hand with the plasma oscillation.  
 792 As mentioned in Chapter 4 and shown in Figure 6.1, plasma oscillation is quite fast —  
 793 several orders of magnitude smaller than Tuna's time step as determined in Section 5.1  
 794 ( $\sim 10 \mu\text{s}$ ). This poses a conundrum. At Tuna's usual time step, the plasma oscillation  
 795 becomes unstable within seconds<sup>3</sup>. On the other hand, reducing the time step by three  
 796 orders of magnitude to resolve the plasma oscillation is computationally infeasible; a  
 797 run slated for an hour would require six weeks to complete.  
 798 As it happens, this problem can be solved by artificially increasing the parallel electric  
 799 constant above its usual value of  $\epsilon_0$ . Doing so lowers both the speed of light and the  
 800 plasma frequency within the simulation.  
 801 This technique — and others like it — has been widespread in numerical modeling since  
 802 it was presented by Boris in 1970[6]. More recently, Lysak and Song considered its use

---

<sup>3</sup>For stability,  $\omega_P \delta t < 1$  is necessary.

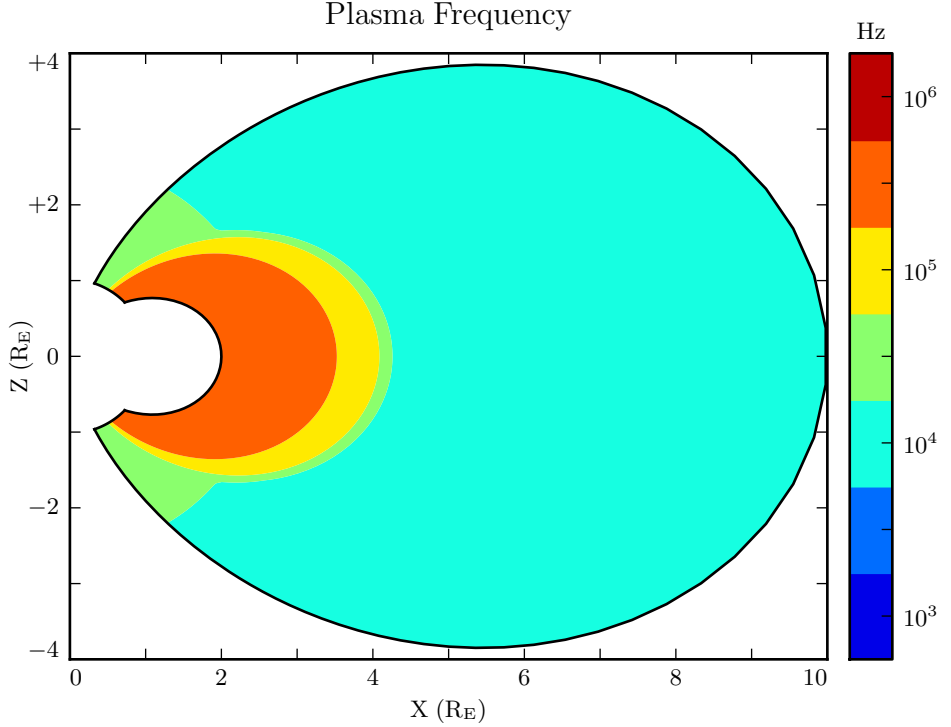


Figure 6.1: The plasma frequency reaches a peak value just under  $10^6$  Hz near the equator. Outside the plasmasphere, its value is closer to  $10^4$  Hz, which is still not well-resolved by Tuna's usual time step.

803 specifically for the case of electron inertial effects[60]. The following paraphrases their  
 804 argument.

Supposing that the current and electric field are oscillating at frequency  $\omega$ , the parallel components of Ampère's law and Ohm's law can be written

$$-i\omega\epsilon_0 E_z = \frac{1}{\mu_0} (\nabla \times \underline{B})_z - J_z \quad -\frac{i\omega}{\nu} J_z = \sigma_0 E_z - J_z \quad (6.5)$$

Then, eliminating the current, the parallel electric field can be related to the curl of the magnetic field by<sup>4</sup>

$$\left(1 - \frac{\omega^2 - i\nu\omega}{\omega_P^2}\right) E_z = \frac{c^2}{\omega_P^2} (\nu - i\omega) (\nabla \times \underline{B})_z \quad (6.6)$$

- 805 In Equation (6.6),  $\frac{c}{\omega_P}$  is the electron inertial length. While the speed of light and the
- 806 plasma frequency each depend on  $\epsilon_0$ , their ratio does not. This allows an estimation of
- 807 how much the model should be affected by an artificially-large electric constant (and
- 808 thus an artificially-small plasma frequency). So long as  $\frac{\omega^2 - i\nu\omega}{\omega_P^2}$  remains small compared
- 809 to unity, the model should behave faithfully.
- 810 For waves with periods of a minute or so, even perhaps-implausibly large Boris factors
- 811 are allowed; for example, increasing  $\epsilon_0$  by a factor of  $10^6$  gives  $\left|\frac{\omega^2 + i\omega\nu}{\omega_P^2}\right| \lesssim 0.01$ .

## 812 6.2 Parallel Currents and Electric Fields

- 813 As discussed in Section 4.4, parallel electric fields in this regime are expected to be six
- 814 or more orders of magnitude smaller than the perpendicular electric fields. Numerical
- 815 results show general agreement: in Figure 6.2, the parallel electric field appears com-
- 816 parable to its perpendicular counterparts only after its been scaled up by six orders of
- 817 magnitude.
- 818 As such, the inclusion of electron inertial effects does not appreciably impact the simu-
- 819 lation's gross behavior; in Faraday's law,  $\nabla \times \underline{E}$  is essentially unaffected. Side by side
- 820 snapshots of the magnetic fields in runs carried out with and without electron inertial
- 821 effects are not visibly distinguishable<sup>5</sup> (not shown).
- 822 Even if there is no significant feedback through Faraday's law, it's informative to con-
- 823 sider the structures that arise in parallel currents and electric fields driven by pertur-
- 824 bations in the ring current. For example, the parallel electric field perturbation (with

---

<sup>4</sup>From Equation (4.4),  $c^2 \equiv \frac{1}{\mu_0 \epsilon_0}$  and  $\sigma_0 \equiv \frac{ne^2}{m_e \nu}$  and  $\omega_P^2 \equiv \frac{ne^2}{m_e \epsilon_0}$ .

<sup>5</sup>In a sense, this is reassuring. It ensures that the present section does not cast doubt on the results presented in Chapter 7, where electron inertial effects are neglected.

Electric Field Snapshots: Quiet Day, 10mHz Current,  $m = 16$

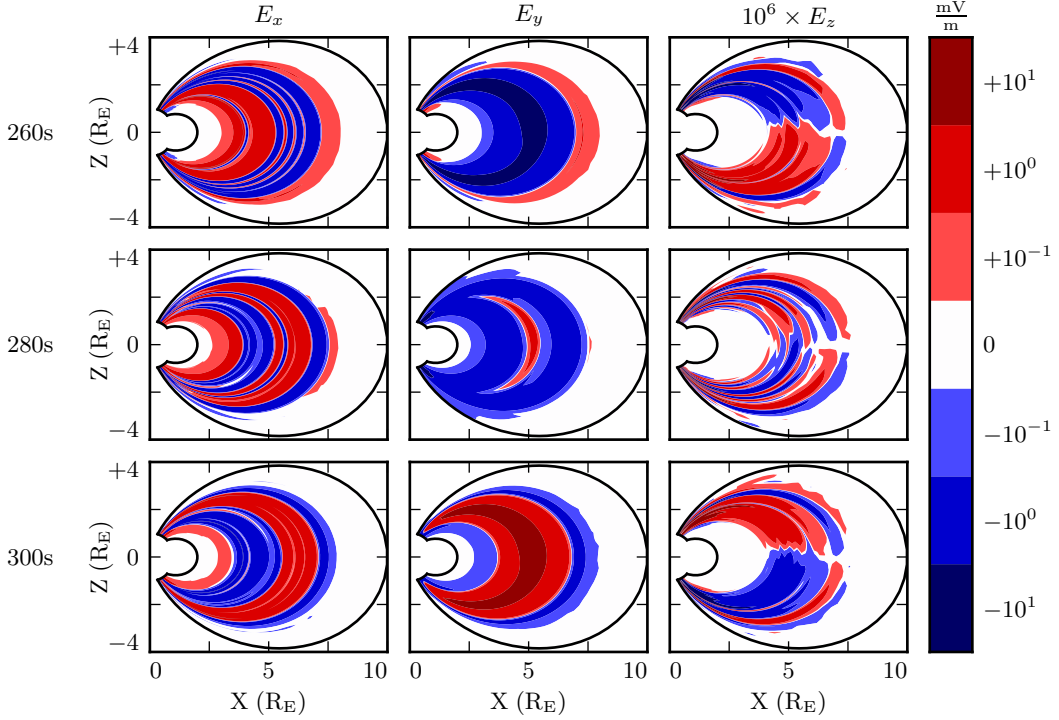


Figure 6.2: Parallel electric fields are smaller than perpendicular electric fields by about six orders of magnitude. As a result, parallel electric fields do not contribute significantly to  $\nabla \times \underline{E}$  in Faraday's law.

maxima near the ionosphere) exhibits the opposite harmonic structure to the perpendicular electric field components (which peak near the equator). It is furthermore notable that the parallel electric field (and the parallel current that comes from it) exhibits real and imaginary components of comparable magnitude.

**TODO:** The compressional component of the magnetic field is also flipped compared to the perpendicular components. Should this have been mentioned in Chapter 3, with the figures showcasing harmonic structure? Radoski showed that it should be the case[78].

832

At low altitude, where the Hall conductivity muddles all of the electric field components together, parallel currents coincide with strong Poynting flux. The imaginary component

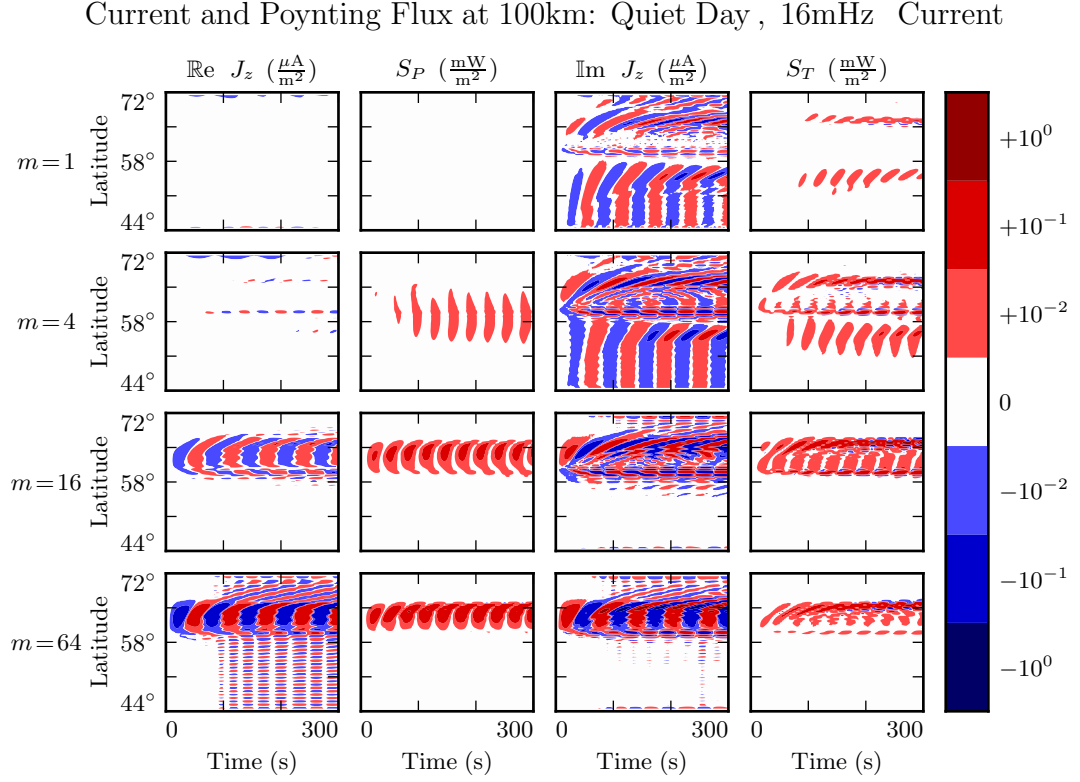


Figure 6.3: TODO: ...

of the current lines up with the toroidal Poynting flux (which comes from imaginary  $E_x$  and imaginary  $B_y^*$ ), while the real current lines up with the poloidal Poynting flux ( $E_y$  and  $B_x^*$  are real)<sup>6</sup>. This is shown in Figure 6.3, which lays out the real and imaginary components of the parallel current (in the first and third column respectively) next to the poloidal and toroidal Poynting flux (second and fourth columns). Four runs are shown, one per row, with azimuthal modenumbers 1, 4, 16, and 64. Values are measured at an altitude of 100 km, the edge of the simulation.

Notably, the Poynting flux waveforms are rectified — they primarily carry energy Earthward. The current, on the other hand, alternates between upward and downward flow.

---

<sup>6</sup>As mentioned in Chapter 5, poloidal field components are in practice overwhelmingly real, indicating that they coincide azimuthally with the (real) driving. Toroidal components are overwhelmingly imaginary, which corresponds to an azimuthal offset.

- 844 This effect presumably arises because the current is a linear quantity while the Poynting  
 845 flux is quadratic: the electric and magnetic fields that make it up oscillate in phase, so  
 846 their product is positive even when they are negative.
- 847 At higher altitude, where the Hall conductivity is small, parallel current is associated  
 848 only with the toroidal mode. Figure 6.4 shows data from the same runs as Figure 6.3,  
 849 arranged in the same way, but the values are taken at an altitude of 1000 km instead of  
 850 100 km.
- 851 In Figure 6.4, as in Figure 6.3, the imaginary component of the parallel current (third  
 852 column) coincides more or less with the toroidal Poynting flux (fourth column). How-  
 853 ever, the real component of the parallel current (first column) is vanishingly small, even  
 854 when the poloidal Poynting flux (second column) is strong. **TODO: Is this expected?**  
 855 **Tikhonchuk[95] looks specifically at the toroidal mode when considering shear Alfven**  
 856 **waves. Does the poloidal mode count as compressional even when it's guided?**
- 857 The magnitude of the parallel current tops out over  $1 \mu\text{A}/\text{m}^2$ , just shy of the up-to-tens  
 858 of  $\mu\text{A}/\text{m}^2$  inferred from ground observations and seen in situ[8, 46, 82].

It's also possible to consider the effect of parallel currents and electric fields on the ionosphere's energy budget, per Poynting's theorem:

$$\frac{\partial}{\partial t} u = -\nabla \cdot \underline{E} - \underline{J} \cdot \underline{E} \quad (6.7)$$

- 859 As shown in Figure 6.5, little energy transfer in the ionosphere is mediated by perpen-  
 860 dicular components of the Poynting flux. The parallel component of  $\underline{J} \cdot \underline{E}$  is comparably  
 861 unimportant. The energy deposited in the ionosphere by the Poynting flux matches  
 862 closely with the energy lost to Joule dissipation — as it should, to conserve energy  
 863 — but according to the model, parallel currents and electric fields do not contribute  
 864 significantly.

Current and Poynting Flux at 1000km: Quiet Day , 16mHz Current

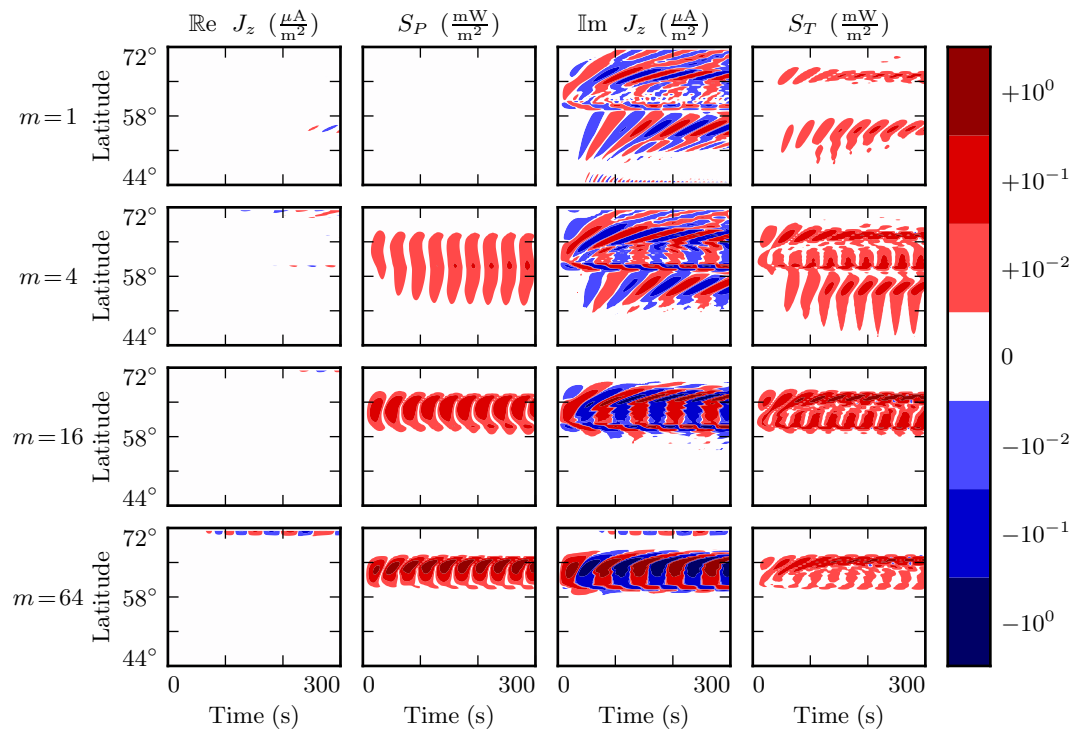


Figure 6.4: TODO: ...

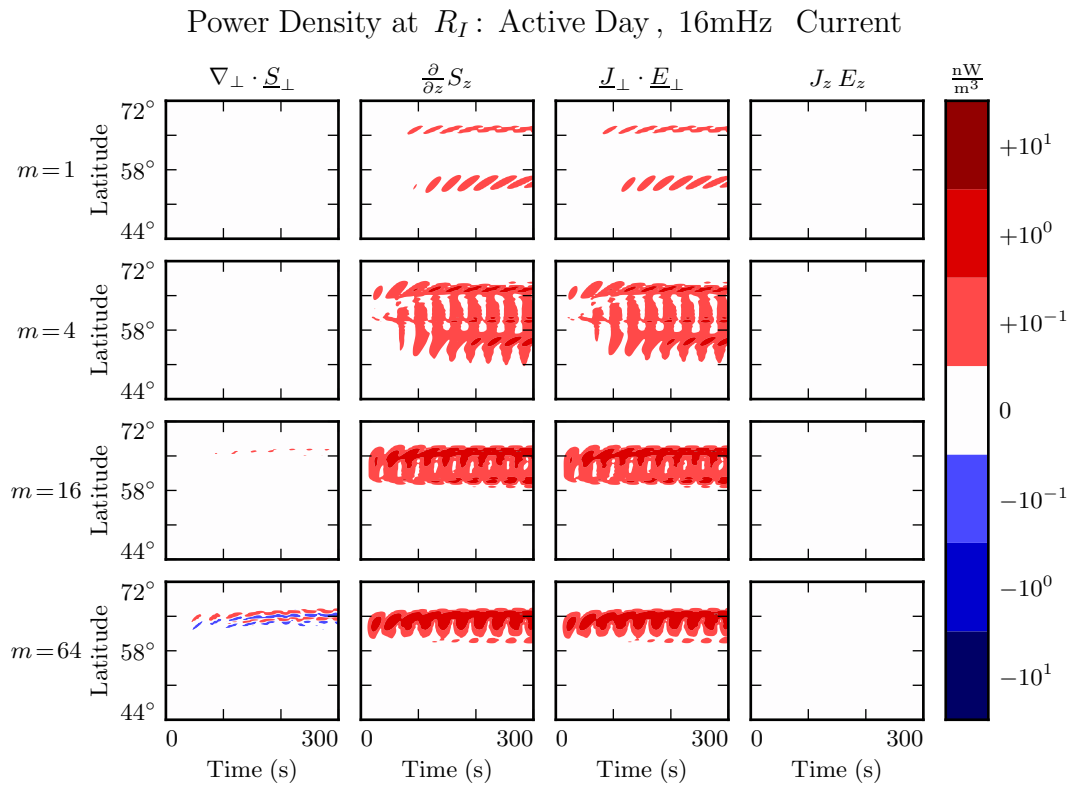


Figure 6.5: While field-aligned currents can be of significant size, they are not particularly good at depositing energy in the ionosphere. Energy deposited by the Poynting flux matches closely with Joule dissipation from the perpendicular currents, while  $J_z E_z$  is smaller by several orders of magnitude.

865 **6.3 Inertial Length Scales**

866 It's not quite fair to compare the parallel and perpendicular contributions to  $\nabla \times \underline{E}$  as  
867 is done in Section 6.2. Perpendicular electric fields are on the order of 1 mV/m, with  
868 wavelengths on the order of  $10^5$  km; they give rise to magnetic field gradients around  
869 0.1 nT/s. Parallel electric fields, closer to  $10^{-6}$  mV/m, would need to vary over length  
870 scales of 0.1 km to match with that.

871 Such scales are believable. The characteristic length scale of the plasma oscillation is  
872 the electron inertial length,  $\frac{c}{\omega_p}$ , which is on the order of 1 km in the auroral ionosphere  
873 and 0.1 km in the low-altitude plasmasphere. However, Tuna's usual grid doesn't resolve  
874 structures so fine; its resolution bottoms out closer to 10 km. That is, with the inclusion  
875 of electron inertial effects, Tuna's grid is too coarse to resolve all of the waves expected  
876 to be present. The model is prone to instability as a result.

877 Figure 6.6 shows a run with perpendicular resolution smaller than the electron inertial  
878 length, side by side with an analogous run on the usual grid. In order to carry out  
879 the inertial-scale run, several concessions were made to computational cost. The run  
880 simulates only a duration of 100 s (other results in previous sections and in Chapter 7  
881 show 300 s), and the grid covers only the auroral latitudes from  $L = 5$  to  $L = 7$ .

882 Even so, the run presents a significant computational expense. Spread over 16 cores, a  
883 100 s run on Tuna's usual grid takes well under an hour. The inertial-scale run barely  
884 finished in 96 hours, the cutoff at the Minnesota Supercomputing Institute<sup>7</sup>.

885 The snapshot shown in Figure 6.6 uses a perpendicular grid resolution of 0.7 km at the  
886 Earthward edge, which just satisfies the Nyquist rate for the minimum inertial length  
887 of 1.7 km. It's still too coarse. There is clearly some small-scale structure developing in  
888 the ionosphere, but it's not well resolved. The large number of "wiggles" portends an  
889 imminent crash.

---

<sup>7</sup>Runtime goes as the inverse square of grid resolution. Not only does finer resolution require more grid cells, but it also gives rise to proportionally smaller crossing times, imposing a smaller time step.

Parallel Electric Fields: Quiet Day, 100s of 16mHz Current,  $m = 16$

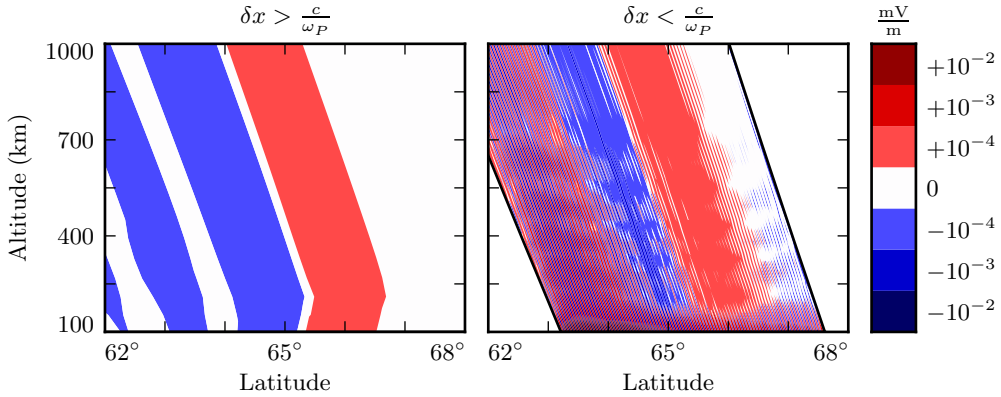


Figure 6.6: The parallel electric field develops significant structure when the perpendicular grid resolution is smaller than the electron inertial length. Unfortunately, such runs are prohibitively expensive. The lower panel — which still fails to resolve wave structure properly — represents a 100-fold increase in computational time.

## 890 6.4 Discussion

891 TODO: The dispersion relation in Chapter 4 suggests that parallel electric fields should  
 892 be smaller than perpendicular electric fields by at least six orders of magnitude. Tuna  
 893 agrees.

894 TODO: Tuna computes parallel currents a bit weaker than those that are observed —  
 895  $\sim 1 \mu\text{A}/\text{m}^2$  rather than  $\sim 10 \mu\text{A}/\text{m}^2$ . The currents accompany the toroidal mode, but  
 896 not the poloidal mode, except where the two are coupled by a strong Hall conductivity.  
 897 Is this expected?

898 TODO: When inertial effects are not properly resolved, the code is prone to instability.  
 899 Resolving inertial scales properly presents a prohibitive computational expense.

900 Electron inertial effects present a promising first-principles-based approach to the in-  
 901 vestigation of parallel currents and electric fields associated with field line resonances.  
 902 Unfortunately, because of the large differences in scale between Pc4 pulsations and the

903 plasma oscillation, the proper deployment of inertial effects presents a prohibitive com-  
904 putational expense. Results shown in Chapter 7 make use of the core version of Tuna  
905 presented in Chapter 5, which does not include the effects of electron inertia.

906 **Chapter 7**

907 **Numerical Results**

908 TODO: An overarching motivation for the present work is that FLRs exhibit significant  
909 behavioral changes as a result of their azimuthal modenumber, but that prior models  
910 have been unable to provide a good picture.

911 **7.1 Modenumber and Compression**

912 It's well known that the poloidal FLR mode is compressional at low modenumber,  
913 but guided at high modenumber. However, the relationship is not well quantified.  
914 Theoretical work has historically been concerned with the limits  $m \rightarrow 0$  and  $m \rightarrow$   
915  $\infty$ [15, 78], and only a handful of satellite observations have explicitly considered an  
916 event's azimuthal modenumber[18, 70, 90]. Using results from Tuna, the present section  
917 examines the strength of the poloidal wave's compressional component at an ensemble  
918 of finite modenumbers.

919 Figures 7.1 and 7.2 show magnetic field snapshots taken from a pair of runs. The first  
920 uses a small azimuthal modenumber, and the second uses a large one. The runs are  
921 otherwise identical: both simulations use the quiet dayside ionospheric profile, and both  
922 are driven at 22 mHz.

923 The differences between the two runs are striking. At low modenumber, wave activity  
924 is visible throughout the simulation domain. Structure in the poloidal magnetic field is  
925 only vaguely governed by the dipole geometry, and the compressional magnetic field is  
926 comparably strong to the two perpendicular components.

927 In contrast, at high modenumber, the poloidal magnetic field is localized to the  $L$ -shells  
928 where the driving is delivered:  $4 \lesssim L \lesssim 6$ . The compressional field is weaker than  
929 the poloidal field by at least an order of magnitude. A third-harmonic poloidal mode  
930 is visible at the outer boundary — its magnitude is just barely large enough to be  
931 visible on the logarithmic scale. The gap between  $L \sim 5$  (where 22 mHz matches a first-  
932 harmonic FLR) and  $L \sim 10$  (where 22 mHz matches a third-harmonic FLR) speaks to  
933 the evanescence of non-guided waves above the compressional Alfvén cutoff frequency<sup>1</sup>.

934 In both the low- $m$  and high- $m$  runs, toroidal activity is more or less coincident with  
935 poloidal activity — as is to be expected, since the driving is purely poloidal, and the  
936 poloidal mode rotates to the toroidal mode over time. It is further notable that the  
937 toroidal mode is sharply guided. Particularly in Figure 7.2, strong, narrow, toroidal  
938 FLRs of opposite phase can be seen oscillating very close to one another. Strong poloidal  
939 waves, in contrast, are smeared in  $L$ .

940 Snapshots are not shown for runs carried out using the other ionospheric profiles (active  
941 day, quiet night, and active night). The morphology of their waves is qualitatively  
942 similar. The differences between the profiles is considered in Sections 7.2 to 7.4.

943 Figure 7.3 quantifies the compressional component of the poloidal mode as a function of  
944 modenumber. Each subplot corresponds to a different run of Tuna — the runs shown in  
945 Figures 7.1 and 7.2 are in the rightmost column, second from the top and second from the  
946 bottom respectively. The red line indicates the ratio between the RMS compressional  
947 magnetic field and the RMS poloidal magnetic field; both averages are taken over the  
948 entire simulation “volume” each time step. Mean values are shown in black.

---

<sup>1</sup>See Section 4.4.

- 949 At  $m = 1$ , the compressional and poloidal magnetic fields are comparable in magnitude.  
950 As  $m$  increases, however, the compressional component quickly falls off. The compres-  
951 sional component is half the strength of the poloidal component at  $m \sim 5$ , and a quarter  
952 by  $m \sim 10$ .
- 953 A slight frequency dependence is apparent across each row in Figure 7.3. Compressional  
954 coupling falls off slower for waves at higher frequency. This is because higher-frequency  
955 waves are that much closer to the cutoff frequency (described in Section 4.4), and so  
956 their propagation across  $L$ -shells is that much less evanescent.
- 957 Similarly, poloidal waves are more prone to compression on the nightside. Due to the  
958 higher Alfvén speed on the nightside, driving is delivered at  $L \sim 6$  instead of  $L \sim 5$ . The  
959 cutoff frequency depends inversely on radial distance. For nightside runs (not shown),  
960  $\left| \frac{B_z}{B_x} \right|$  falls to 50% at  $m \sim 8$  and to 25% at  $m \sim 16$ .
- 961 Notably, the waves considered in the present work are fundamental harmonics. The  
962 compressional behavior of the poloidal mode may vary for the (more-common) second  
963 harmonic: Radoski suggests that the asymptotic value of  $\left| \frac{B_z}{B_x} \right|$  is inversely proportional  
964 to the harmonic number[78].

Magnetic Field Snapshots: Quiet Day , 22mHz Current,  $m = 2$

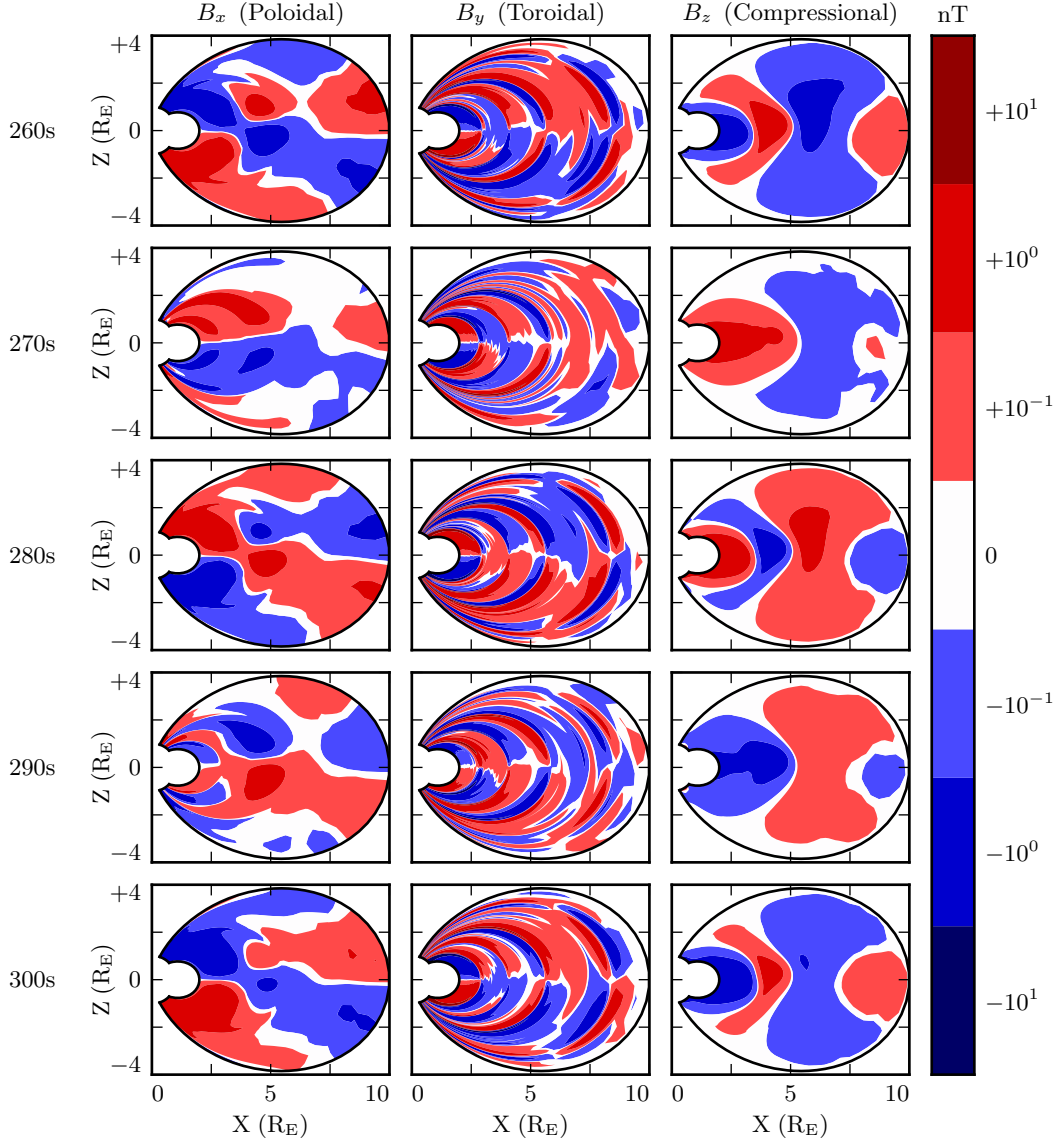


Figure 7.1: Each row in the above figure is a snapshot in time. The three columns show the simulated poloidal, toroidal, and compressional magnetic field. Due to the run's low azimuthal modenumber, the poloidal mode has a significant compressional component. This is visible both in the fact that  $B_z$  is comparable in size to  $B_x$ , and in that structure in  $B_x$  is only vaguely guided by the geometry of the magnetic field. Toroidal waves, in contrast, are sharply guided.

Magnetic Field Snapshots: Quiet Day , 22mHz Current,  $m = 32$

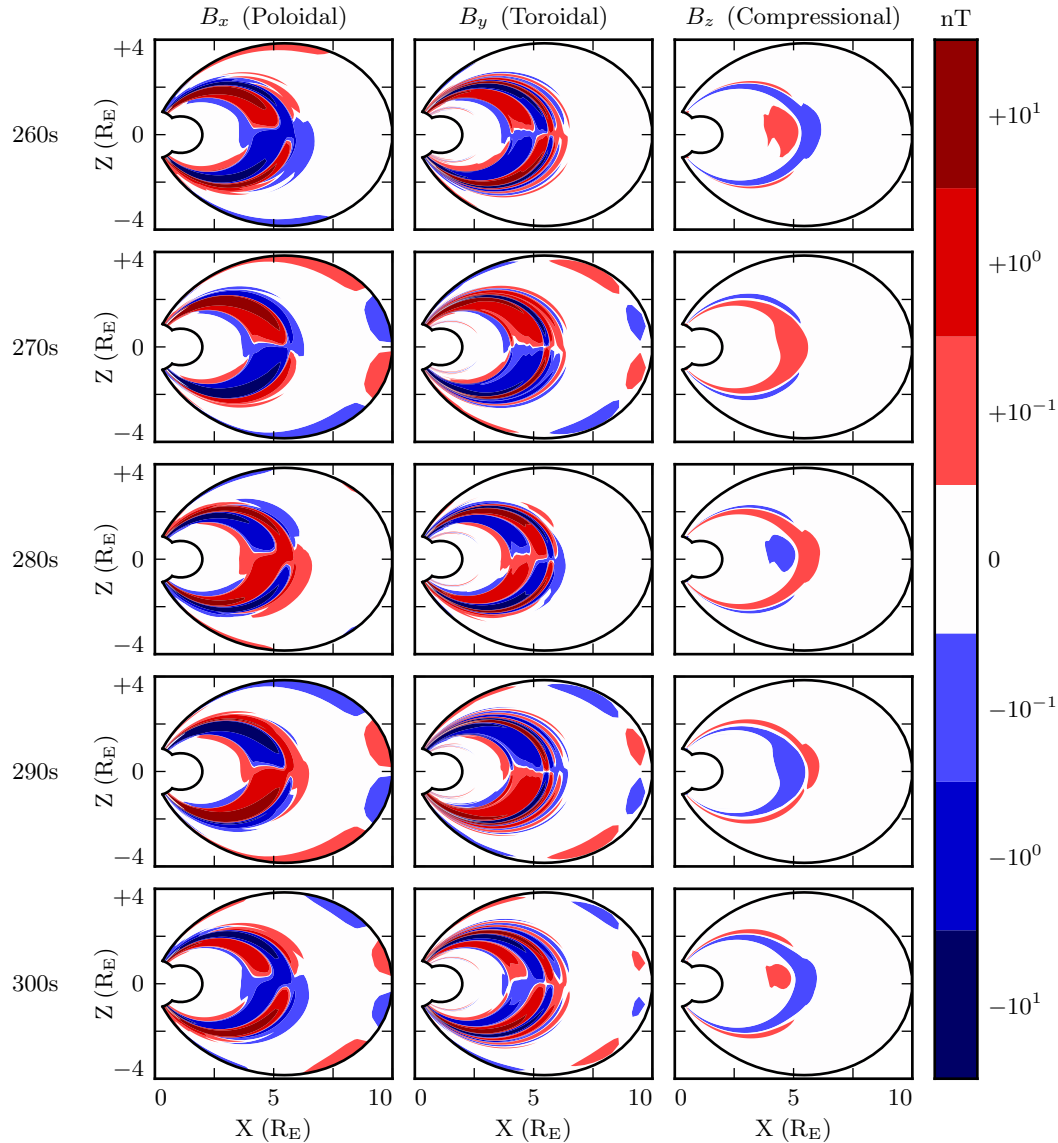


Figure 7.2: The above figure is analogous to Figure 7.1, but the runs use a larger azimuthal modenumber. The change has a dramatic effect. The poloidal wave is concentrated much more sharply in  $L$ , and its compressional component is weaker by an order of magnitude. Regardless of modenumber, toroidal waves exist at a range of  $L$  shells similar to poloidal waves, and show sharp definition across  $L$ -shells.

### Compressional Coupling to the Poloidal Mode: Quiet Day

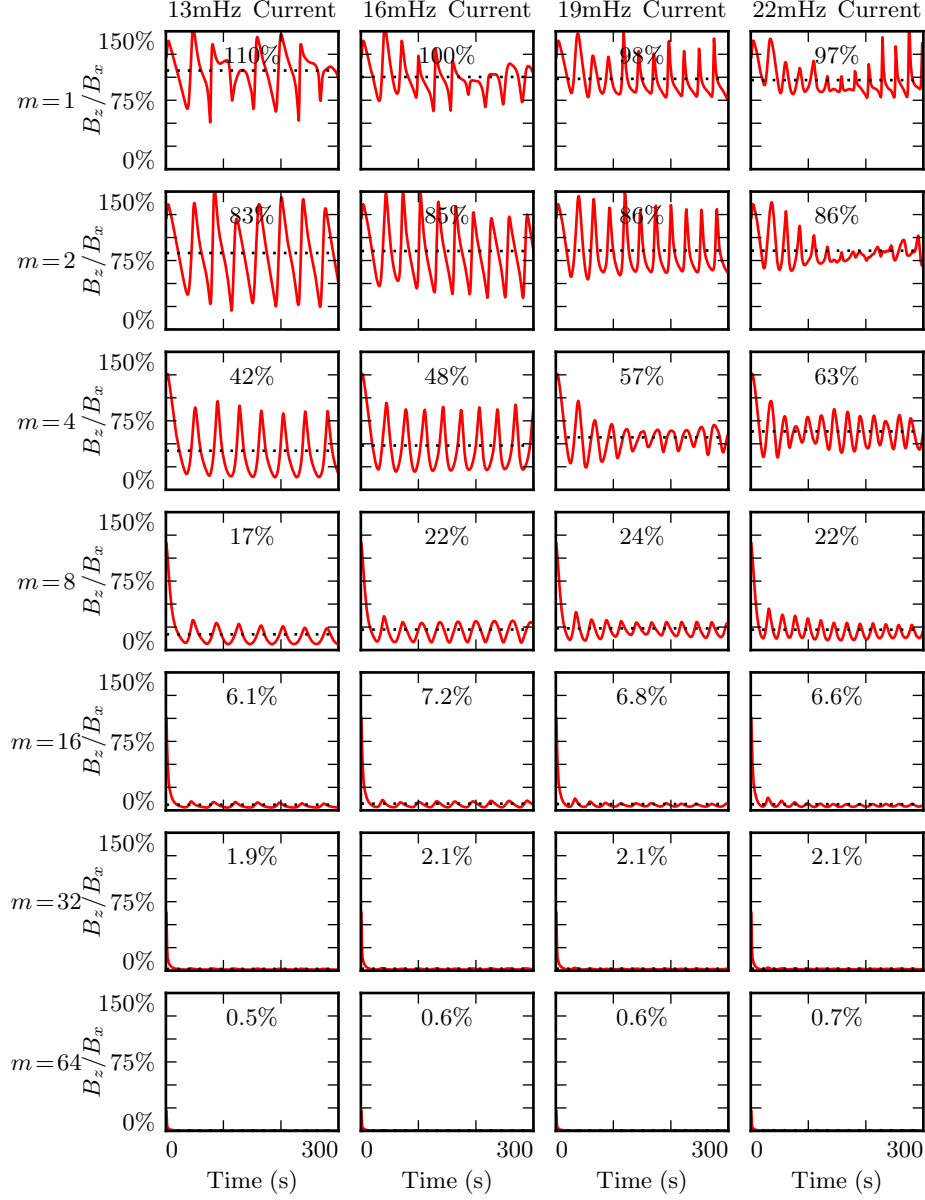


Figure 7.3: Each subplot above corresponds to a different run; the runs shown in Figures 7.1 and 7.2 are in the rightmost column, second from the top and second from the bottom respectively. Red lines indicate the ratio between the RMS compressional and poloidal magnetic fields. Mean values are shown in black. The compressional field is comparable to the poloidal field at  $m = 1$ , but falls quickly.

965    **7.2 Resonance and Rotation on the Dayside**

- 966    In his 1974 paper, Radoski argues that a poloidally-polarized wave should asymptoti-  
967    cally rotate to the toroidal polarization[78] as a result of the curved derivative in the  
968    meridional plane. The question of finite poloidal lifetimes is considered further in a 1995  
969    paper by Mann and Wright[64]. Their numerical work used a straightened field line,  
970    with an Alfvén speed gradient in the “radial” direction. They also found a rotation over  
971    time from poloidal to toroidal polarization, with the characteristic time proportional to  
972    the azimuthal modenumber.
- 973    The present section builds on the aforementioned results by relaxing several of their non-  
974    physical assumptions. Tuna’s geometry is more realistic than Radoski’s half-cylinder or  
975    the box model used by Mann and Wright. Previous work has considered the evolu-  
976    tion of an initial condition, while the simulations shown below include driving delivered  
977    over time. In addition, Tuna features a finite, height-resolved ionospheric conductivity  
978    profile, rather than the perfectly-reflecting boundaries used in the past.

Each subplot in Figure 7.4 is analogous to Figure 3 in Mann and Wright’s paper[64]. Blue lines show the total energy in the poloidal mode as a function of time. Red lines show toroidal energy. Runs are organized analogous to those in Figure 7.3: drive frequency is constant down each column, and azimuthal modenumber is constant across each row. Axis bounds are held constant across all subplots. The poloidal and toroidal energy are computed by integrating over the electromagnetic energy density, per Poynting’s theorem:

$$U_P = \int \frac{dV}{2\mu_0} \left( B_x^2 + \frac{1}{v_A^2} E_y^2 \right) \quad U_T = \int \frac{dV}{2\mu_0} \left( B_y^2 + \frac{1}{v_A^2} E_x^2 \right) \quad (7.1)$$

- 979    Where the differential volume  $dV$  is computed using the Jacobian<sup>2</sup> to account for Tuna’s  
980    unusual geometry. The integral is evaluated in  $u^1$  and  $u^3$  but not  $u^2$  (Tuna’s missing  
981    half-dimension), which gives energy in units of gigajoule per radian. More than anything  
982    else, this serves as a reminder that Pc4 pulsations are localized in MLT.

---

<sup>2</sup>See Section 5.1.

983 The 28 runs shown in Figure 7.4 use an ionospheric profile corresponding to the dayside  
984 during times of low solar activity, where the conductivity is relatively high. The active  
985 and quiet dayside profiles are briefly contrasted in Section 7.4; for the most part, the  
986 focus of the present work is on the difference between the dayside and the nightside  
987 (Section 7.3). Differences between the two dayside profiles are small in comparison.

988 The fact that red (toroidal) lines appear at all in Figure 7.4 speaks to a net rotation  
989 of energy from the poloidal mode to the toroidal. As discussed in Section 5.3, Tuna’s  
990 driving is delivered purely into the poloidal electric field (reflecting a perturbation in  
991 the magnitude of the ring current).

992 As expected, the rotation from poloidal to toroidal is slowest at large azimuthal mode-  
993 numbers. The toroidal energy overtakes the poloidal energy within a single drive period  
994 at  $m = 4$ ; at  $m = 64$ , the most of the energy is in the poloidal mode for  $\sim 10$  periods.  
995 However, the relationship between azimuthal modenumber and rotation timescale is  
996 not linear, as was suggested by Mann and Wright. Instead, in a practical setting, the  
997 rotation is fastest at  $m \sim 4$ .

998 This is explained by the compressional character of the poloidal mode. At very low  
999 modenumber, energy in the poloidal mode moves readily across  $L$ -shells. A significant  
1000 fraction of that energy is lost to the outer boundary before rotating to the toroidal  
1001 mode. At high modenumber — as discussed in Section 7.1 — compressional propagation  
1002 is evanescent, so all energy in the poloidal mode must ultimately rotate to the toroidal  
1003 mode or be lost to Joule dissipation.

1004 Joule dissipation is a major player in the system’s energy economy. However, due to the  
1005 highly conductive dayside ionosphere, dissipation timescales are in the tens of Pc4 wave  
1006 periods. Energy loss through Joule dissipation asymptotically balances energy input  
1007 from driving, but most of that energy is not lost until after it has rotated from the  
1008 poloidal mode to the toroidal. As such, in most runs shown in Figure 7.4, the energy  
1009 content of the toroidal mode asymptotically exceeds that of the poloidal mode.

1010 The asymptotic energy content of the system also depends on how well the drive fre-  
1011 quency matches the local eigenfrequency. If the two do not match, energy is lost to  
1012 destructive interference between the standing wave and the driving.

1013 In principle, energy moves between the poloidal and toroidal modes due to their direct  
1014 coupling through the ionospheric Hall conductivity. In practice, this effect is small.  
1015 When the runs shown in Figure 7.4 are repeated with the Hall conductivity set to zero,  
1016 the resulting energy curves are not visibly different.

1017 The low- $m$  runs at 19 mHz merit additional discussion. These runs accumulate energy  
1018 over a large number of wave periods, while the low- $m$  waves at 13 mHz, 16 mHz, and  
1019 22 mHz do not. This effect is likely nonphysical. At 19 mHz, a third-harmonic resonance  
1020 forms very close to the outer boundary. The resonance is likely enhanced by nonphysical  
1021 reflections against the simulation’s boundary conditions.

1022 The presence of individual harmonics can be seen in the contours shown in Figures 7.5  
1023 and 7.6. These figures show the same runs as Figure 7.4, arranged in the same way on  
1024 the page. However, instead of showing the total energy integrated over the simulation  
1025 domain, the energy densities are averaged over the volume of each flux tube individually.  
1026 Figure 7.5 shows contours of poloidal energy density and Figure 7.6 shows toroidal  
1027 energy density.

1028 The top few rows of Figure 7.5 confirm that the poloidal mode’s compressional nature is  
1029 to blame for its failure to accumulate energy at low modenumber. Waves move so readily  
1030 across field lines that no visible amount of energy builds up at  $L \sim 5$ , the location of the  
1031 driving. Some energy moves inward, and is trapped by the peak in Alfvén speed just  
1032 inside the plasmapause, while the rest moves to the outer boundary. The time spent  
1033 moving across field lines counts against the poloidal mode’s finite lifetime, inhibiting  
1034 the buildup of poloidal energy density even at  $L$ -shells where the wave matches the local  
1035 eigenfrequency.

1036 As  $m$  increases, the energy distribution becomes more concentrated in  $L$ , though indi-  
1037 vidual features remain fairly broad. At  $m = 8$ , runs at 13 mHz and 16 mHz are inclined  
1038 to build up energy just inside the plasmapause, while those at 19 mHz and 22 mHz res-  
1039 onate just outside the plasmapause; in all four cases, the energy is spread over a range  
1040 of at least 1 in  $L$ .

1041 The peak energy density in the bottom-right run (22 mHz driving,  $m = 64$ ) is by far the  
1042 largest of any run in Figure 7.5. The azimuthal modenumber is large, so the poloidal

1043 mode is purely guided; energy is not smeared across multiple  $L$ -shells. And, crucially, the  
1044 frequency of the driving matches closely with the Alfvén frequency at  $L \sim 5$ . Other runs  
1045 on the bottom row are also guided, but they reach lower asymptotic energy densities  
1046 because of a mismatch between the drive frequency and the local eigenfrequency —  
1047 resulting in destructive interference between the standing wave and its driver.

1048 The eigenfrequencies in the magnetosphere are significantly affected by the location of  
1049 the plasmapause. When the runs in Figure 7.5 are repeated with the plasmapause at  
1050  $L = 5$  instead of  $L = 4$ , the strongest resonance at  $L \sim 5$  drops from 22 mHz to 16 mHz  
1051 (not shown).

1052 Whereas the poloidal contours are smeared over a swath of  $L$ -shells (though the high- $m$   
1053 runs less so), the toroidal contours in Figure 7.6 appear only where the wave frequency  
1054 matches the local eigenfrequency. A horizontal line drawn through the Alfvén speed  
1055 frequency profiles (recall Figure 3.1) intersects the profile up to three times: once as  
1056 the Alfvén frequency drops through the Pc4 range from its low-latitude peak, again as  
1057 the Alfvén frequency rises sharply at the plasmapause, and a third time as the Alfvén  
1058 frequency drops asymptotically. Toroidal waves can be seen resonating at all three of  
1059 these locations in the  $m = 4$ , 22 mHz run in Figure 7.6, along with a third harmonic at  
1060 large  $L$ . This is consistent with observations: toroidal resonances are noted for having  
1061 frequencies which depend strongly on  $L$ , in contrast to the poloidal mode's less-strict  
1062 relationship between frequency and location.

1063 In only one of the runs shown in Figure 7.5 does the poloidal mode attain an energy  
1064 density on the order of  $10^{-1}$  nJ/m<sup>3</sup>. On the other hand, the toroidal mode reaches  
1065  $\sim 10^{-1}$  nJ/m<sup>3</sup> in six of the runs in Figure 7.6. That is, the poloidal mode only exhibits  
1066 a high energy density on the dayside only when conditions are ideal; the toroidal mode  
1067 isn't nearly so particular.

Poloidal (Blue) and Toroidal (Red) Energy: Quiet Day

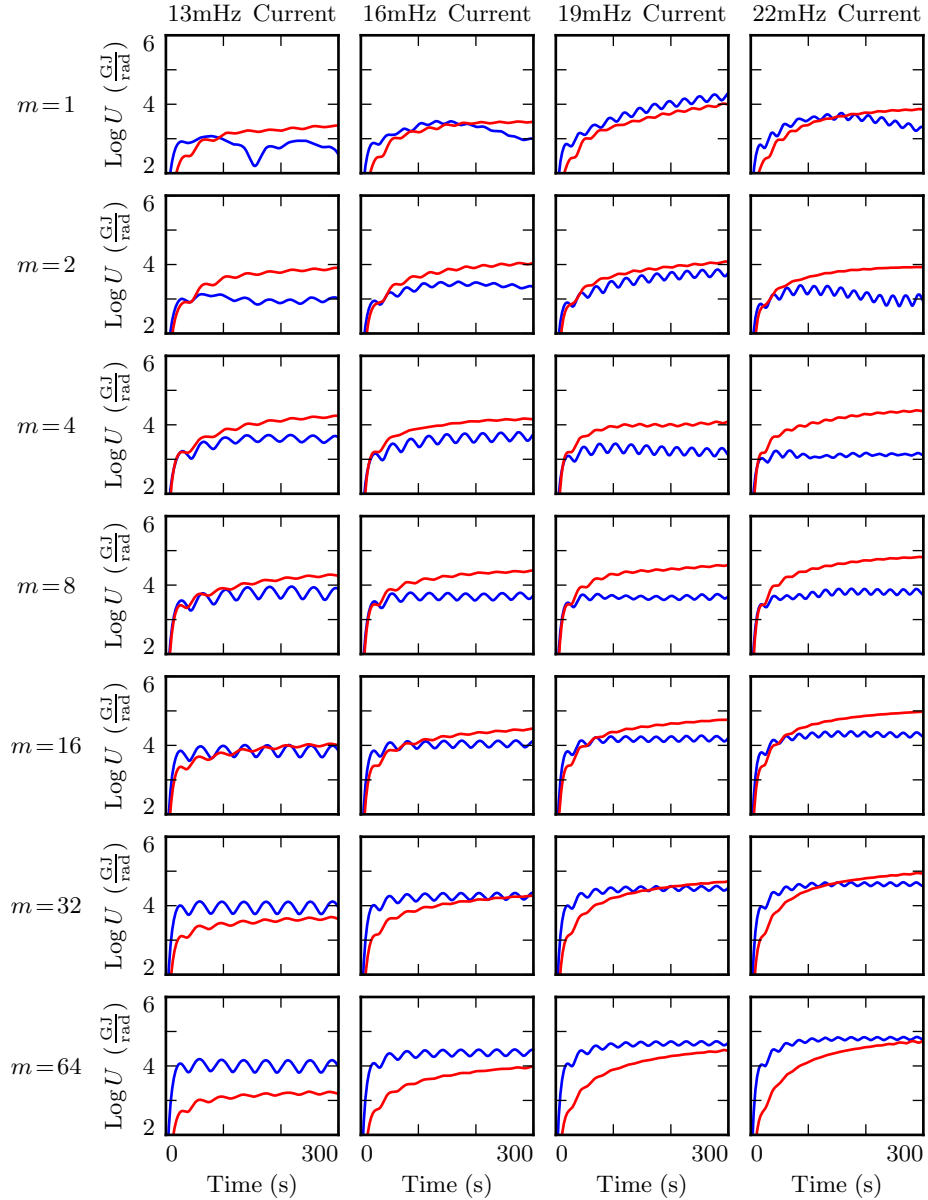


Figure 7.4: TODO: Lorem ipsum dolor sit amet, consectetur adipiscing elit, sed do eiusmod tempor incididunt ut labore et dolore magna aliqua. Ut enim ad minim veniam, quis nostrud exercitation ullamco laboris nisi ut aliquip ex ea commodo consequat. Duis aute irure dolor in reprehenderit in voluptate velit esse cillum dolore eu fugiat nulla pariatur.

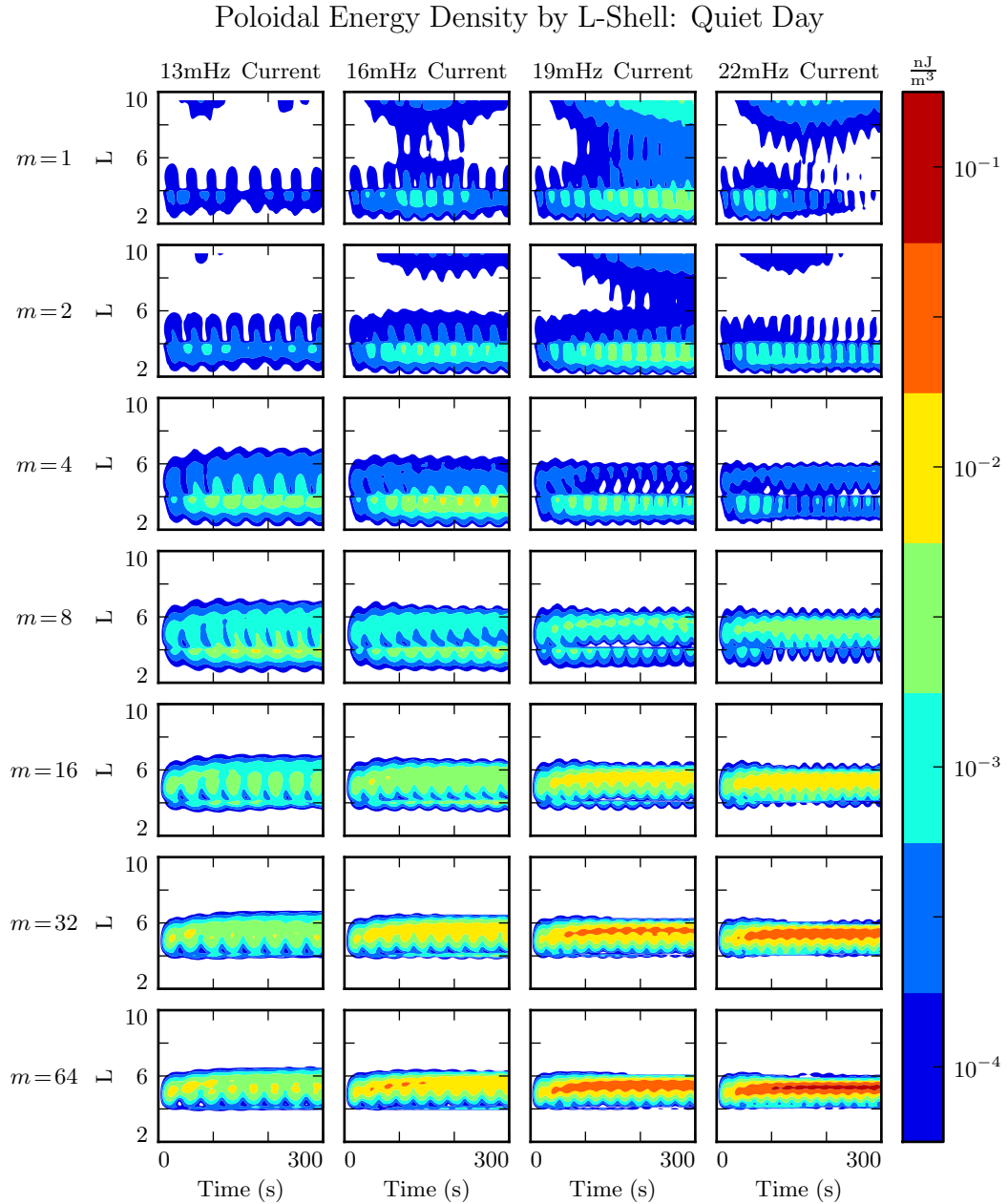


Figure 7.5: TODO: Lorem ipsum dolor sit amet, consectetur adipiscing elit, sed do eiusmod tempor incididunt ut labore et dolore magna aliqua. Ut enim ad minim veniam, quis nostrud exercitation ullamco laboris nisi ut aliquip ex ea commodo consequat. Duis aute irure dolor in reprehenderit in voluptate velit esse cillum dolore eu fugiat nulla pariatur.

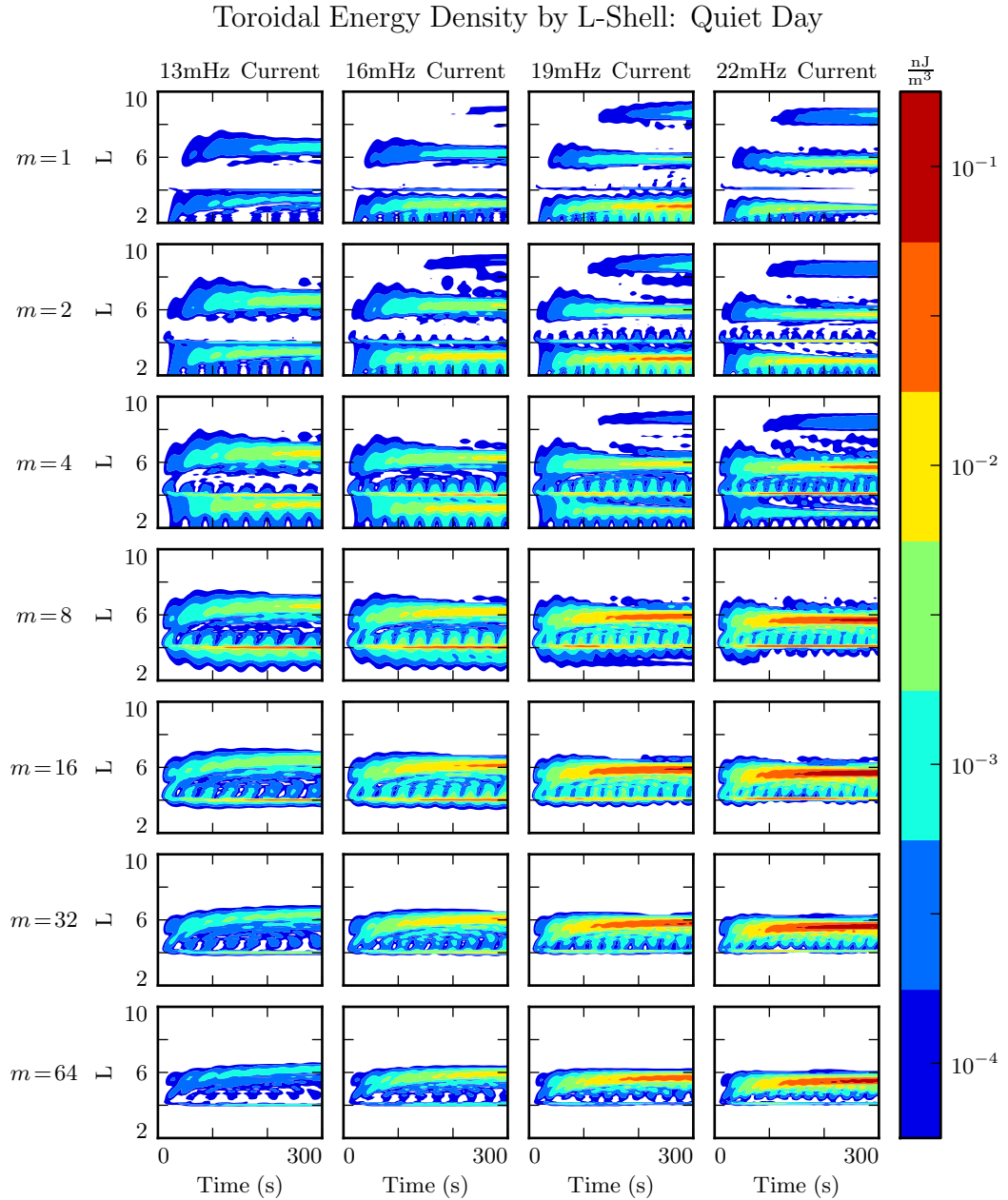


Figure 7.6: TODO: Lorem ipsum dolor sit amet, consectetur adipiscing elit, sed do eiusmod tempor incididunt ut labore et dolore magna aliqua. Ut enim ad minim veniam, quis nostrud exercitation ullamco laboris nisi ut aliquip ex ea commodo consequat. Duis aute irure dolor in reprehenderit in voluptate velit esse cillum dolore eu fugiat nulla pariatur.

1068 **7.3 Resonance and Rotation on the Nightside**

1069 Each subplot in Figures 7.7 to 7.9 corresponds to a run.

1070 Driving is moved from  $L = 5$  to  $L = 6$  to line up better. Or even  $L = 7$ ?

1071 Compared to the dayside ionosphere employed in Section 7.2, the nightside profiles  
1072 exhibit two major differences. The ionospheric conductivity is lower, and the Alfvén  
1073 speed is higher. The present section and Section 7.3 show results using only the active  
1074 nightside profile. The differences between the quiet and active nightside ionospheric  
1075 profiles are small compared to the differences between either dayside profile and either  
1076 nightside profile; all four profiles are briefly compared in Section 7.4.

1077 The low conductivity on the nightside gives rise to strong Joule dissipation. Waves are  
1078 damped out in just a few bounces, so asymptotic energy values are reached quickly.

1079 Even so, the poloidal-to-toroidal rotation is qualitatively the same as on the dayside.

1080 The further the azimuthal modenumber from the rotation peak at  $m = 4$ , the lower the  
1081 asymptotic toroidal energy level is compared to the poloidal. If anything, the effect is  
1082 exaggerated by the small dissipation timescale. When  $m = 64$ , no more than  $\sim 10\%$  of  
1083 the energy in the poloidal mode rotates to the toroidal mode before being lost.

1084 **TODO:**  $\dots$  is arranged analogously to the figures in Section 7.2: each subplot is  
1085 an independent run, drive frequency is constant down each column, and azimuthal  
1086 modenumber is constant across each row. Poloidal energy is blue; toroidal energy is  
1087 red.

1088 The lower energies in **TODO:**  $\dots$  (compared to **TODO:**  $\dots$ , the analogous dayside  
1089 runs) are not entirely due to increased Joule dissipation. Due to the difference in electric  
1090 constant between the dayside and nightside magnetospheres<sup>3</sup>, resonant frequencies just  
1091 outside the typical ( $L_{PP} = 4$ ) plasmapause fall well outside the  $Pc4$  range. None of the  
1092 frequencies shown in **TODO:**  $\dots$ , when delivered at  $L_{drive} = 5$ , align with the local  
1093 eigenfrequency.

---

<sup>3</sup>See Figure 3.1.

Poloidal (Blue) and Toroidal (Red) Energy: Quiet Night

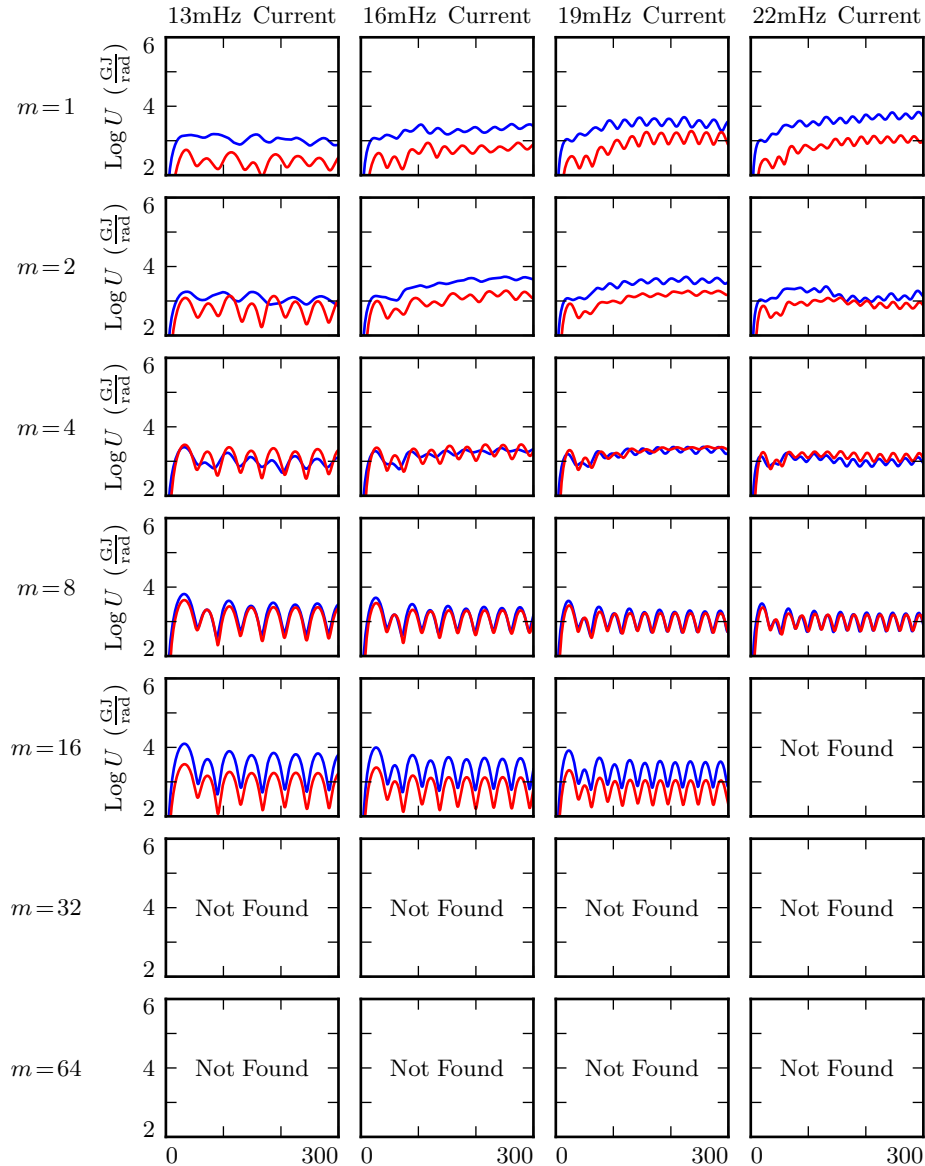


Figure 7.7: **TODO: ...**

1094 As in **TODO: ...**, the 19mHz run with  $m = 1$  is an apparent exception. A large  
 1095 amount of energy builds up in a third harmonic very close to the outer boundary. The  
 1096 interaction is likely nonphysical.

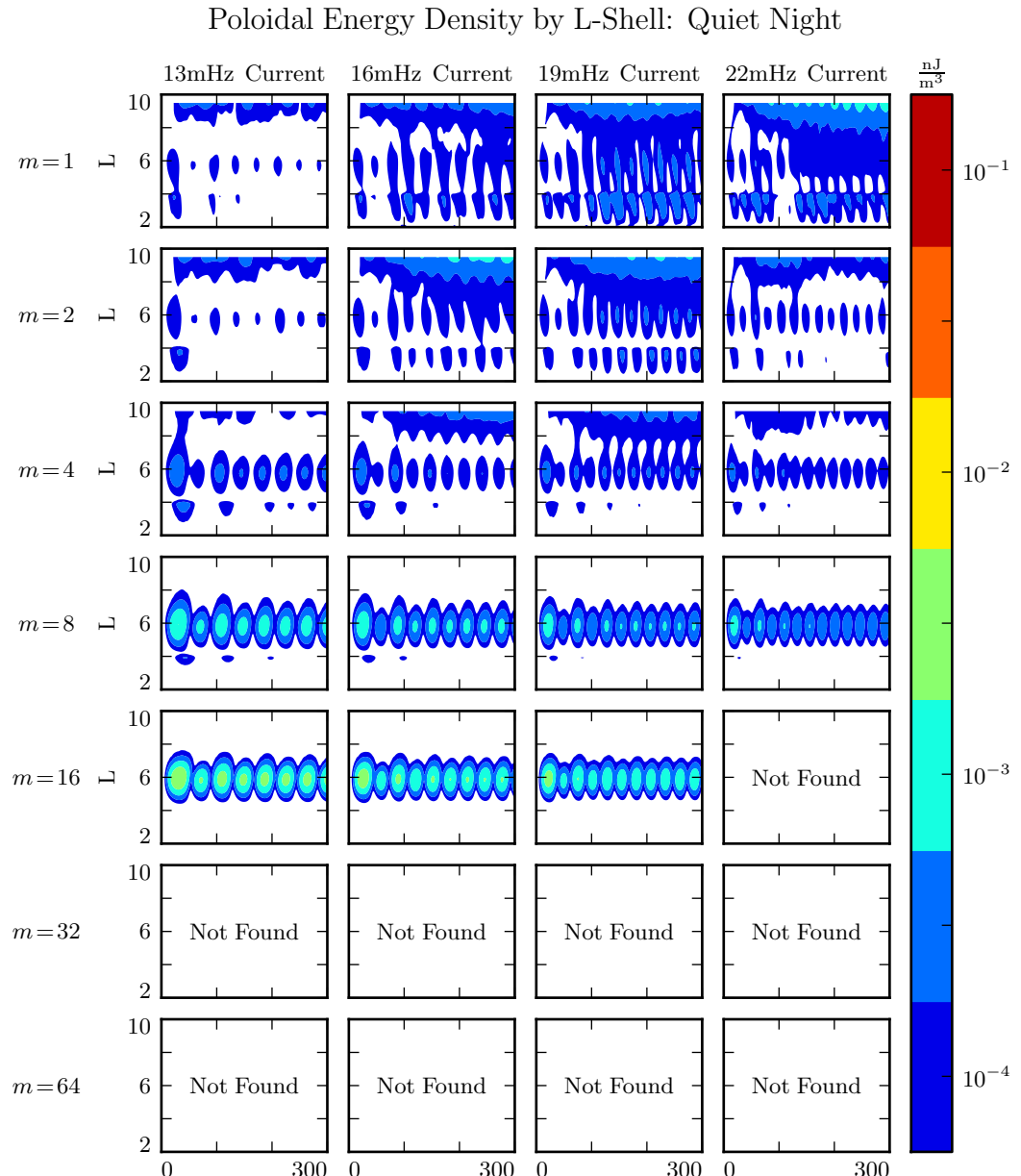


Figure 7.8: TODO: ...

<sup>1097</sup> TODO: It may be significant that  $\int \sigma dz$  is constant across all  $L$ -shells, but  $\int \frac{\sigma}{v_A^2} dz$  is  
<sup>1098</sup> not.

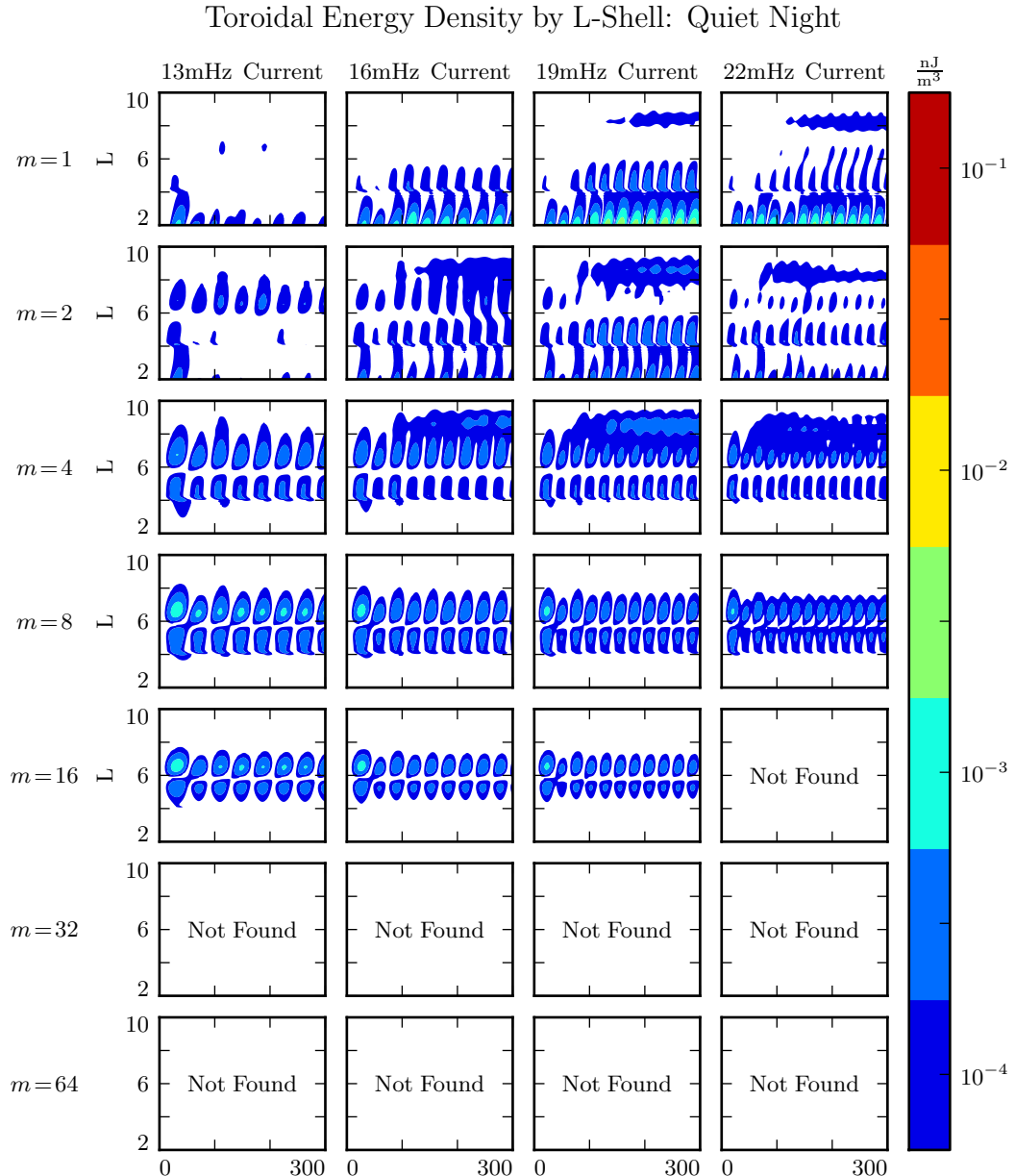


Figure 7.9: **TODO: ...**

1099 Behavior closer to resonance is shown in **TODO: ...**. The plasmapause remains at  
 1100  $L_{PP} = 4$ , but the driving is moved out to  $L_{drive} = 6$ , at which point the local Alfvén  
 1101 frequency overlaps the Pc4 frequency band.

1102 There is surprisingly little difference between `TODO: ...` (the subplots of which are  
1103 arranged analogously). Asymptotic energy levels vary — in the case of high  $m$  and low  
1104 frequency, runs in `TODO: ...` are more energetic by an order of magnitude or more  
1105 — but the qualitative behavior is the same. Driving is balanced by dissipation over the  
1106 course of just a few drive periods. Dissipation outstrips poloidal-to-toroidal rotation in  
1107 the case of large azimuthal modenumber. And, unlike on the dayside, the toroidal mode  
1108 typically does not match the asymptotic energy level seen in the poloidal mode.

1109 `TODO: ...` shows the radial distribution of poloidal energy on the nightside — a slice  
1110 of each run shown in `TODO: ...`. Broadly speaking, the behavior is consistent with  
1111 that seen in `TODO: ...`: energy is smeared across  $L$ -shells at small  $m$  and guided at  
1112 high  $m$ , with particularly strong energy buildup when the drive frequency matches the  
1113 local Alfvén frequency.

1114 As discussed in `TODO: ...`, the nightside's relatively low ionospheric conductivity  
1115 increases the rate of dissipation. Asymptotic energy content is reached quickly, and is  
1116 small compared to that seen in analogous dayside runs.

1117 The effect is particularly pronounced at large modenumber, where the poloidal-to-  
1118 toroidal rotation timescale is slower than the nightside dissipation timescale. In most of  
1119 the dayside runs shown in `TODO: ...`, the toroidal mode asymptotically exceeds the  
1120 poloidal mode both in terms of total energy content and in terms of peak energy density.  
1121 On the nightside, the opposite is true. At high modenumber, the asymptotic rotation  
1122 from the poloidal mode to the toroidal mode doesn't occur until most of the energy has  
1123 been lost to Joule dissipation. Peak poloidal energy densities at  $m = 64$  exceed their  
1124 toroidal counterparts — shown in `TODO: ...` — by an order of magnitude.

1125 `TODO: On the nightside, unlike the dayside, toroidal contours are messy. Why?`

1126 The behavior of the poloidal mode on the nightside matches qualitatively with the  
1127 behavior on the dayside. At low  $m$ , energy is lost to the outer boundary. At high  $m$ ,  
1128 resonance occurs, but only if the drive frequency is close to the local eigenfrequency.  
1129 The big difference is that, due to the increased dissipation in the ionosphere, asymptotic  
1130 energy densities are relatively low, and reached relatively quickly.

1131 In low- $m$  runs, the poloidal mode loses energy to the outer boundary, which impairs the  
1132 growth of the toroidal mode. At high  $m$ , poloidal-to-toroidal rotation is slow compared  
1133 to dissipative timescales on the nightside. The strongest toroidal waves — which are  
1134 still weak compared to those on the dayside — thus appear at moderate  $m$ .

## 1135 7.4 Ground Signatures and Giant Pulsations

1136 While the majority of the action is in space, the majority of FLR observations have  
1137 been ground-based. The present section explores the same simulations discussed in  
1138 Sections 7.2 and 7.3, but in terms of their ground signatures rather than their broad  
1139 energy distributions.

1140 As in the figures shown in Sections 7.2 and 7.3, each row in Figures 7.10 and 7.11 shows  
1141 runs at a different modenumber. The columns are magnetic field contours; the vertical  
1142 axis is latitude, and the horizontal axis is time. The four columns are components of  
1143 the magnetic field signatures at the ground: the north-south magnetic field (first and  
1144 third columns) and the east-west magnetic field (second and fourth columns). The pair  
1145 on the left show a simulation carried out using the active ionospheric profile, and the  
1146 pair on the right show a simulation using the quiet profile.

1147 Notably, the magnetic polarization of a low frequency Alfvén wave is rotated by  $\sim 90^\circ$  as  
1148 it passes through the ionosphere[41]. The east-west field on the ground ( $B_\phi$ ) corresponds  
1149 to the poloidal polarization in space, and the north-south field on the ground ( $B_\theta$ )  
1150 corresponds to the toroidal mode.

1151 **TODO:** What's going on with the empty frame for nightside,  $m = 1, 16\text{ mHz}$ ?

1152 **TODO:** Don't use 19 mHz! It's wonky at low modenumber. Use 22 mHz instead.

1153 The most striking feature of Figures 7.10 and 7.11 is the modenumber dependence.  
1154 As modenumber increases, the magnetic field signatures become sharply localized in  
1155 latitude. At high  $m$ , ground signatures are concentrated between  $60^\circ$  and  $70^\circ$ , peaking  
1156 just below  $65^\circ$ . This shows good agreement with observations of Pgs peaked near  $66^\circ$ .

1157 At low modenumber, magnetic signatures are weak on the ground because the waves  
1158 in space are also weak. At high modenumber, waves in space are strong, but so is  
1159 the attenuation of magnetic signatures by the ionosphere<sup>4</sup>. The “sweet spot” at which  
1160 magnetic ground signatures are maximized falls at  $m = 16$  to  $m = 32$ . For comparison,  
1161 Pgs are generally observed with azimuthal modenumbers of 16 to 35[92].

1162 Ground signatures are maximized at  $m = 16$  and  $m = 32$  on both the dayside (Fig-  
1163 ure 7.10) and the nightside (Figure 7.11). Dayside signatures are stronger than those on  
1164 the nightside, and quiet dayside and quiet nightside responses are stronger than those  
1165 on the active dayside and active nightside respectively. The strongest magnetic fields  
1166 at the ground are primarily east-west polarized – as Pgs are[92].

1167 **TODO:** At present, Tuna’s ionospheric profiles do not allow the dawn and dusk flanks  
1168 to be distinguished from the dayside and nightside.

---

<sup>4</sup>See Equation (3.2).

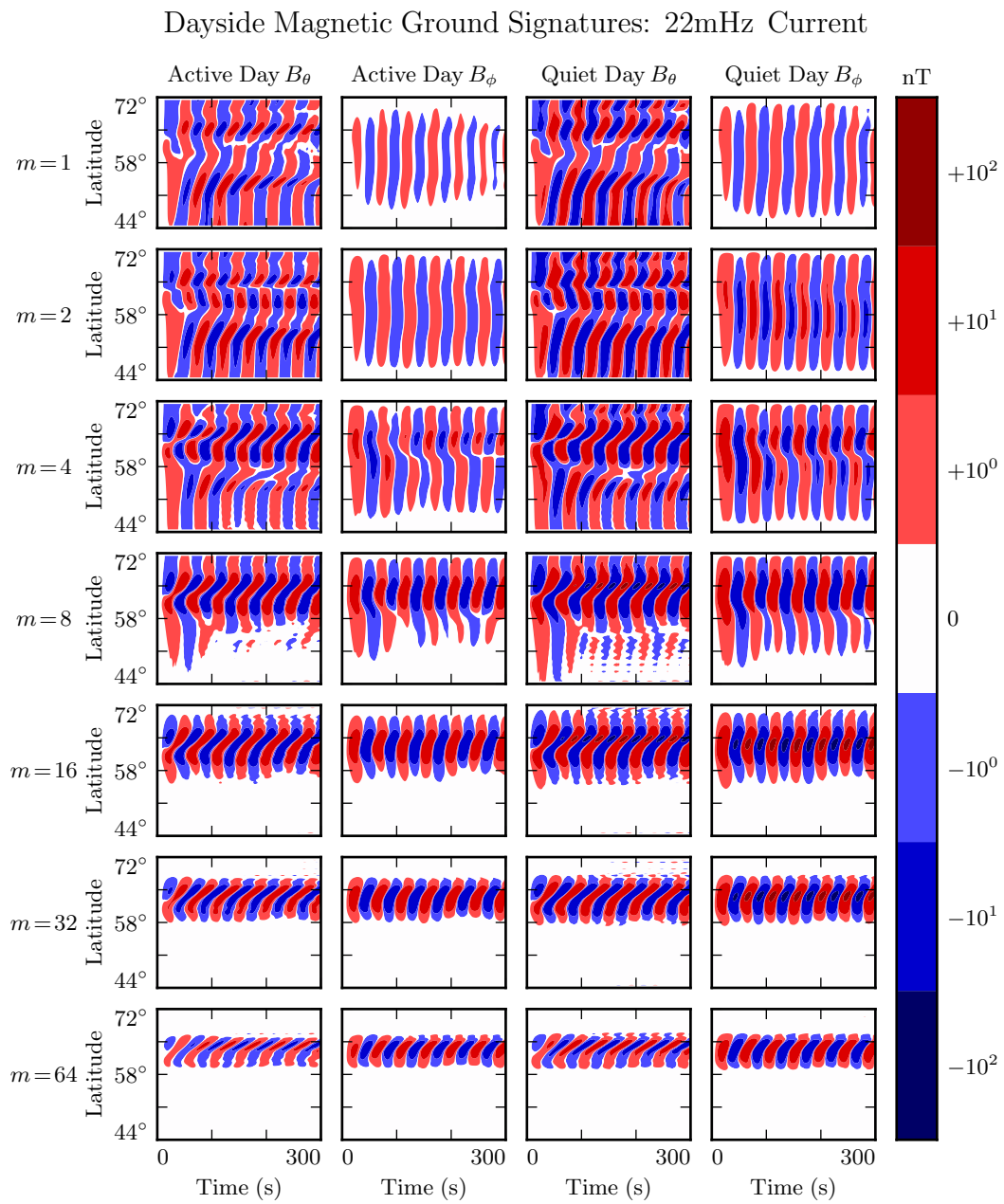


Figure 7.10: TODO: ...

### Nightside Magnetic Ground Signatures: 13mHz Current

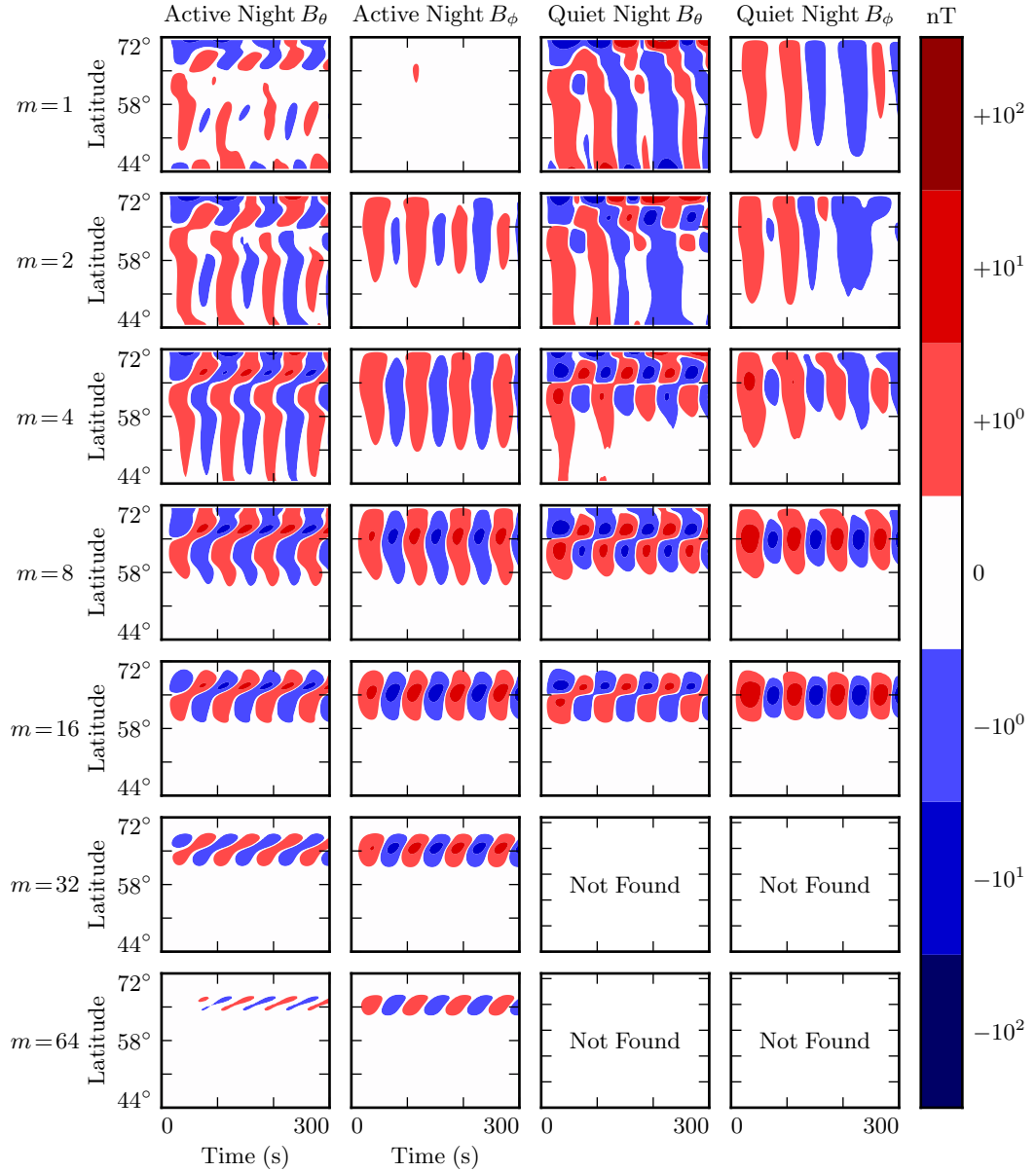


Figure 7.11: Nightside ground signatures are less strongly peaked than those on the dayside, but qualitative features are the same: the strongest signals are in  $B_\phi$ , peaked over just a few degrees in latitude, at a modenumber of 16 or 32, under quiet ionospheric conditions.

1169 **7.5 Discussion**

1170 **TODO:** Make this section read nicely.

1171 Poloidal FLRs rotate to the toroidal mode over time. Toroidal modes do not appear to  
1172 rotate back to the poloidal mode. When  $m$  is small, the rotation is comparable to an  
1173 oscillation period; when  $m$  is large, rotation timescales are comparable to ten periods,  
1174 sometimes more.

1175 On the dayside, little damping takes place over rotation timescales, so the toroidal mode  
1176 asymptotically exceeds the toroidal mode. The exception is waves with low modenumber,  
1177 where poloidal waves can escape by propagating across field lines. An evaluation  
1178 of what happens then — whether they bounce back off the magnetopause, for example  
1179 — is beyond the scope of the present work.

1180 On the nightside, the conductivity of the ionosphere is low enough that damping  
1181 timescales become comparable to oscillation timescales. Waves are weaker, since they  
1182 are unable to accumulate energy over as many periods. High- $m$  toroidal waves are  
1183 particularly weak, since the dissipation timescale is faster than the poloidal-to-toroidal  
1184 rotation timescale.

1185 Waves resonate best when the frequency of the driving matches the local eigenfrequency  
1186 where it's delivered. The eigenfrequency is significantly affected by the size of the  
1187 plasmasphere.

1188 The poloidal mode, due to its compressional character, exhibits an energy profile which  
1189 is smeared in  $L$ . The toroidal mode, on the other hand, forms sharp resonances where the  
1190 drive frequency matches the local eigenfrequency. This may explain why the observed  
1191 frequencies of poloidal waves depend weakly on  $L$ , while the frequencies of toroidal  
1192 waves are strongly dependent on  $L$ .

1193 At low  $m$ , ground signatures are weak because waves in space are weak because energy  
1194 can easily escape through the simulation's outer boundary. At large  $m$ , ground signatures  
1195 are attenuated by the ionosphere. The “sweet spot” in azimuthal modenumber at  
1196 which ground signatures are strongest is around 16 to 32. Furthermore, ground signatures  
1197 are strongest when ionospheric profiles corresponding to solar minimum are used.

1198 Driving in the poloidal electric field gives rise to primarily ground signatures polarized  
1199 primarily in the east-west direction at the ground. And, when the frequency of the  
1200 driving does not match the local eigenfrequency, the high- $m$  resonates weakly in place,  
1201 rather than tunneling across field lines to resonate strongly somewhere else.

1202 These findings imply, awkwardly, that the morphology of giant pulsations may reveal  
1203 relatively little about their origins. One can consider a hypothetical magnetosphere  
1204 subject to constant driving: broadband in frequency, broadband in modenumber, just  
1205 outside the plasmapause. Low- $m$  poloidal waves will quickly rotate to the toroidal mode  
1206 (and/or propagate away). High- $m$  waves will resonate in place, accumulating energy  
1207 over time, and giving rise to “multiharmonic toroidal waves”[89]; Fourier components  
1208 that do not match the local eigenfrequency will quickly asymptote. Waves with very high  
1209 modenumbers will be attenuated by the ionosphere. The response on the ground will be  
1210 significantly stronger during quiet solar conditions. In other words, the measurements  
1211 on the ground will look very much like a giant pulsation.

1212 **TODO:** Notably, the present work offers no explanation as to Pgs’ distinctive distribu-  
1213 tion in MLT!

1214 **Chapter 8**

1215 **Observations**

1216 TODO: You know what would be great for putting this numerical work in context?

1217 A nice, consistent survey that breaks down the occurrence rate of Pc4 pulsations by  
1218 harmonic, etc.

1219 TODO: The tools used in the present chapter — SPEDAS and the SPICE kernel —  
1220 are publicly available. They run best with an IDL license, which is not, but they are  
1221 functional using just the (free) IDL virtual machine. The code is wrapped up in a Git  
1222 repository: <https://github.com/chizarlicious/RBSP> (maybe should make a GitHub  
1223 organization to hold this code, to decouple it from my personal account?).

1224 Previous work:

1225 Dai[17] used RBSP to look at poloidal Pc4 events, with a bias in favor of the second  
1226 harmonic — 890 events. Events are most common near noon, but are spread across the  
1227 day and dusk side, with a few stragglers at midnight.

1228 Anderson[3] used AMPTE/CCE (mostly  $L > 7$ , near the equator) to look at Pc4 events  
1229 — 7000 hours. Limited commentary on parity. Toroidal modes were found to outnumber  
1230 poloidal modes three-to-one. “Harmonic toroidal resonances” are spread 0600 to 1600.  
1231 “Fundamental toroidal resonances” (which are not mutually exclusive with harmonic  
1232 ones!) appear everywhere but dusk.

1233 Liu[56] used THEMIS (equatorial orbit,  $L$  out to  $\sim 10$ ) to look at both poloidal and  
1234 toroidal modes — 9805 one-minute Pc4 events (?). No commentary on parity. Poloidal  
1235 events are most common at noon (with another peak post-midnight) and strongest  
1236 on the dusk side. Toroidal events are most common from pre-dawn to pre-noon and  
1237 strongest pre-midnight and post-dawn.

1238 Kokubun[52] used ATS6 (synchronous orbit) —  $\sim 150$  events. No commentary on har-  
1239 monic. Toroidal events dominate in the dawn sector. Poloidal events are spread across  
1240 all MLT, with a peak in the early afternoon and Pgs in the early morning.

1241 Motoba[70] used GOES13 and GOES15 (geosynchronous) to look specifically at Pgs —  
1242 105 events. Seen from midnight to noon, with a strong peak before dawn, 0300 or so.

## 1243 8.1 Sampling Bias and Event Selection

1244 The present analysis makes use of all available Van Allen Probe data, which spans from  
1245 October 2012 to August 2015. Between the two probes, that's just over 2000 days of  
1246 observation.

1247 For the purposes of Pc4 pulsations, it's reasonable to consider the two probes to be  
1248 independent observers. Nearly all Pc4 events occur near apogee ( $L \gtrsim 5$ ), at which  
1249 point the two probes are several hours apart in MLT. Pc4 events are typically not large  
1250 enough to be seen by both probes simultaneously, and not long enough in duration to  
1251 be seen by two probes passing through the same region of space several hours apart.

1252 **TODO:** Quantify how often an event is seen by both probes?

1253 Electric and magnetic field waveforms are collected using the probes' **TODO: ...** in-  
1254 strument. Values are cleaned up by averaging over the ten-second spin period. Three-  
1255 dimensional electric field data is then obtained using the  $\underline{E} \cdot \underline{B} = 0$  assumption. Notably,  
1256 this assumption is taken only when the probe's spin plane is offset from the magnetic  
1257 field by at least  $15^\circ$ . The rest of the data — about half — is discarded, which introduces  
1258 a sampling bias against the flanks.

1259 A further bias is introduced by the probes' non-integer number of precessions around  
 1260 Earth. As of July 2014, apogee had precessed once around Earth[17]. The present work  
 1261 considers roughly one and a half precessions; the nightside has been sampled at apogee  
 1262 twice as often as the dayside.

1263 The spatial distribution of usable data — that is, data for which three-dimensional  
 1264 electric and magnetic fields are available — is shown in Figure 8.1. Bins are unitary  
 1265 in  $L$  and in MLT. Event distribution in magnetic latitude is not shown; the Van Allen  
 1266 Probes are localized to within  $\sim 10^\circ$  of the equatorial plane.

1267 **TODO:**  $L$  is italicized and MLT is not? That seems weird.

1268 Field measurements are transformed from GSE coordinates into the same dipole coor-  
 1269 dinates used in Chapters 5 and 7. The  $z$  axis is parallel to the background magnetic  
 1270 field, which is estimated using a ten-minute running average of the magnetic field mea-  
 1271 surements. The  $y$  axis is defined per  $\hat{y} \parallel \hat{z} \times \underline{r}$ . The  $x$  axis is then defined per  $\hat{x} \equiv \hat{y} \times \hat{z}$ .  
 1272 This scheme guarantees that the axes are right-handed and pairwise orthogonal[56].

1273 The  $\sim 1000$  days of usable data are considered half an hour at a time, which gives a fre-  
 1274 quency resolution of  $\sim 0.5$  mHz in the discrete Fourier transform. Spectra are computed  
 1275 for all six field components:  $\tilde{B}_x$ ,  $\tilde{B}_y$ ,  $\tilde{B}_z$ ,  $\tilde{E}_x$ ,  $\tilde{E}_y$ , and  $\tilde{E}_z$ . The background magnetic  
 1276 field is subtracted before transforming the magnetic field components, leaving only the  
 1277 perturbation along each axis<sup>1</sup>. Each waveform is also shifted horizontally so that its  
 1278 mean over the thirty minute event is zero.

Frequency-domain Poynting flux is computed from the electric and magnetic field trans-  
 forms. A factor of  $L^3$  compensates the compression of the flux tube, so that the resulting  
 values are effective at the ionosphere. Poloidal and toroidal Poynting flux, respectively,  
 are given by:

$$\tilde{S}_P \equiv -\frac{L^3}{\mu_0} \tilde{E}_y \tilde{B}_x^* \quad \tilde{S}_T \equiv \frac{L^3}{\mu_0} \tilde{E}_x \tilde{B}_y^* \quad (8.1)$$

---

<sup>1</sup>As in Chapters 5 and 7,  $B_x$  refers not to the full magnetic field in the  $x$  direction, but to the perturbation in the  $x$  direction from the zeroth-order magnetic field.

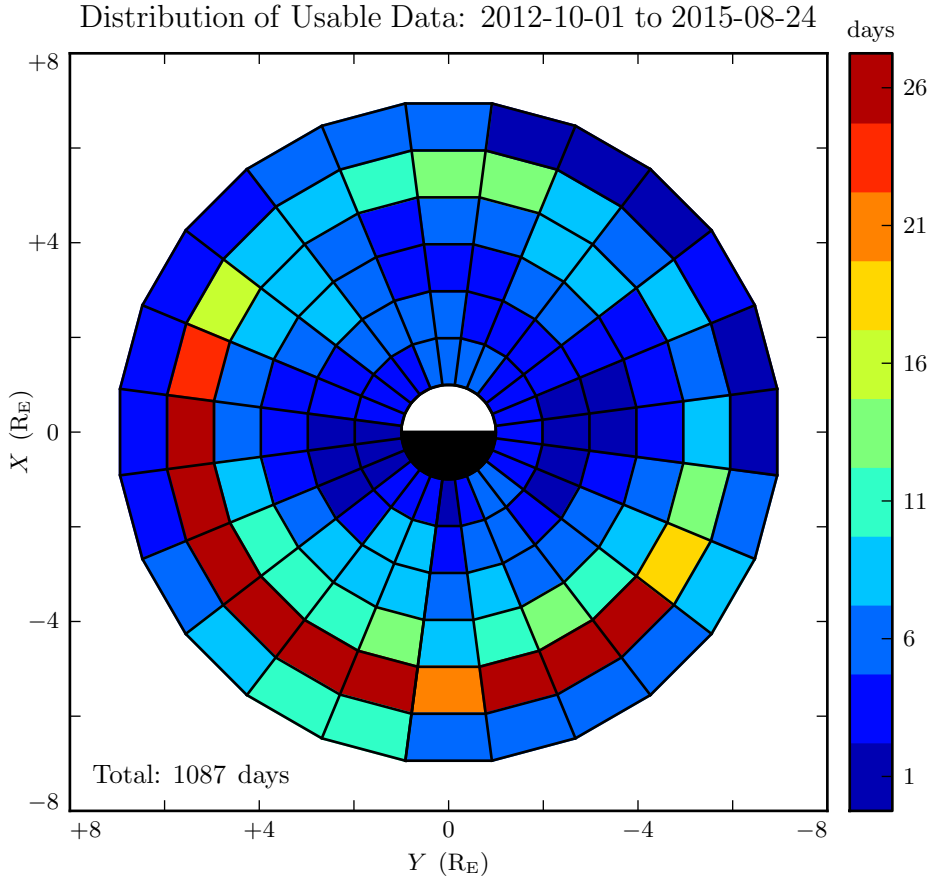


Figure 8.1: Three-dimensional electric field values are computed by assuming  $\underline{E} \cdot \underline{B} = 0$ . Data is discarded whenever the magnetic field falls within  $15^\circ$  of the spin plane, which introduces a bias against the flanks. Furthermore, the probes have completed one and a half precessions around Earth; the dayside has been sampled once at apogee, and the nightside twice.

1279 The poloidal and toroidal channels are independently checked for Pc4 waves. For each  
 1280 channel, a Gaussian profile is fit to the magnitude of the Poynting flux,  $|\tilde{S}(\omega)|$ . If the  
 1281 fit fails to converge, or if the peak of the Gaussian does not fall within 5 mHz of the  
 1282 peak value of  $\tilde{S}$ , the event is discarded. Events are also discarded if their frequencies  
 1283 fall outside the Pc4 frequency range (7 mHz to 25 mHz) or if their amplitudes fall below  
 1284  $10^{-2}$  mW/m<sup>2</sup> (out of consideration for instrument sensitivity).

1285 Events are discarded if their parity is ambiguous. The electric field and the magnetic  
1286 field must be coherent at a level of 0.9 or better (judged at the discrete Fourier transform  
1287 point closest to the peak of the Gaussian fit). Any event within  $3^\circ$  of the magnetic  
1288 equator is also not used; as discussed in Chapter 3, in order to distinguish an odd mode  
1289 from an even mode, it's necessary to know whether the observation is made north or  
1290 south of the equator.

1291 TODO: How much time do the probes spend within  $3^\circ$  of the magnetic equator?

1292 Notably, events are not filtered based on the width of their spectra or on the division of  
1293 their energy between standing and traveling modes. These two parameters are discussed  
1294 in Section 8.6 and Section 8.5 respectively.

1295 TODO: First and third harmonics can only be distinguished by guessing at the fre-  
1296 quency. Chisham and Orr[14] argue that around  $7 R_E$ , frequency around 10 mHz pre-  
1297 cludes higher harmonics. Or maybe look at [34]?

1298 TODO: Are we biased in terms of Dst? What's the distribution look like for the good  
1299 data and for the bad data?

## 1300 8.2 Rate of Pc4 Events

1301 The filters described in Section 8.1 yield 840 Pc4 events, the spatial distribution of  
1302 which is shown in Figure 8.2. In each bin, the event count is normalized to the amount  
1303 of usable data, per Figure 8.1. Bins shown in white contain zero events.

1304 Consistent with previous work, Pc4 events are rarely observed at  $L < 4$ . Nearly 30 %  
1305 of the usable data shown in Figure 8.1 is located inside  $L = 4$ , yet that data accounts  
1306 for only 18 of the 840 events.

1307 TODO: Dai thinks that Pc4 pulsations are common inside the plasmasphere. He uses  
1308 the plasma number density gradient to estimate the plasmapause location. We use  
1309 Scott's method, which is a cutoff of  $100 / \text{cm}^3$ . We find basically no events inside the  
1310 plasmapause — only 43 out of 840.

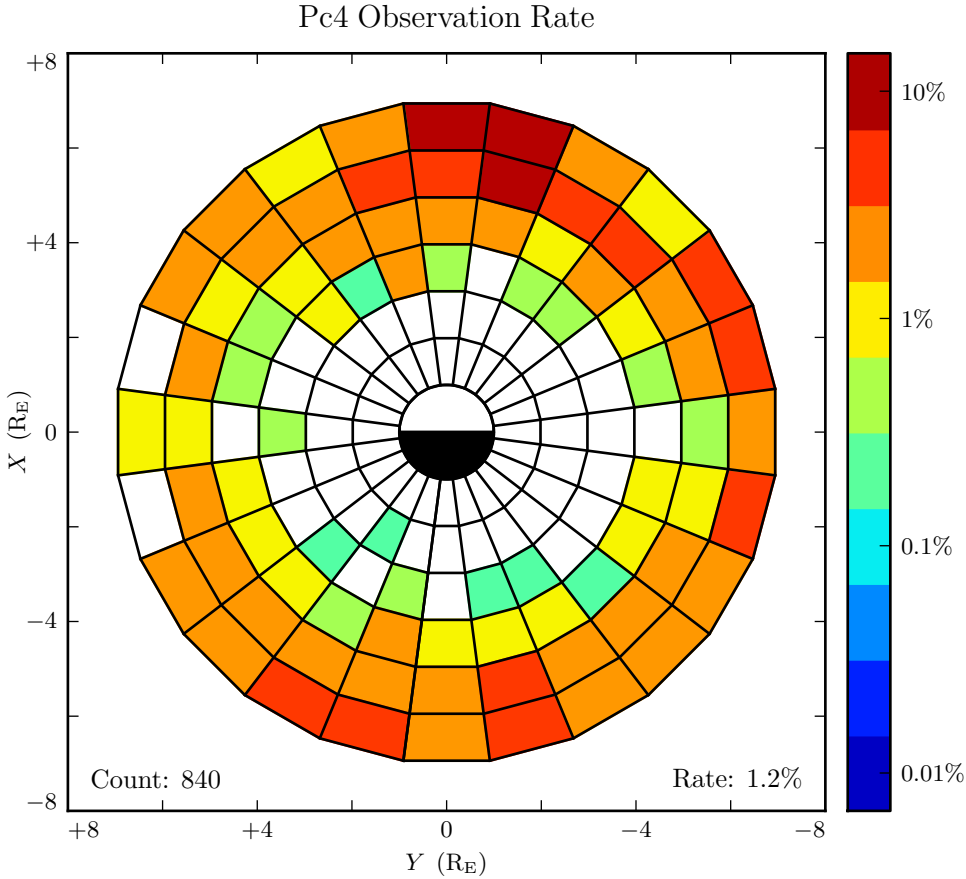


Figure 8.2: The above figure shows the spatial distribution of all 840 observed Pc4 events. Counts are normalized by the amount of usable data in each bin. The value in the bottom-right corner is the mean of the rate in each bin; it's an estimate of how often Pc4 events would be observed if the sampling were distributed uniformly in space. Events where the poloidal and toroidal channel trigger simultaneously ( $\sim 10\%$  of cases) are counted as only a single event. Bins shown in white contain zero events.

1311 In Figure 8.3, events are partitioned by parity and polarization, yielding 141 odd poloidal  
 1312 events, 237 even poloidal events, 457 odd toroidal events, and 87 even toroidal events  
 1313 — a total of 922 events. The total is greater than 840 because in  $\sim 10\%$  of events, the  
 1314 poloidal and toroidal channels trigger independently. Such cases count as only a single  
 1315 event in Figure 8.2, but the toroidal and poloidal events are both shown in Figure 8.3.

1316 TODO: Even poloidal events and even toroidal events are distributed similarly, which is  
1317 good to see, since even poloidal events give rise to even toroidal events. The relationship  
1318 is less clear for odd events, though odd poloidal modes and odd toroidal modes are both  
1319 least common at dusk.

1320 TODO: Odd toroidal events are by far the most commonly observed. Oddly, even  
1321 poloidal events are the least common.

1322 TODO: Even modes are less likely to be observed on the ground? [92]

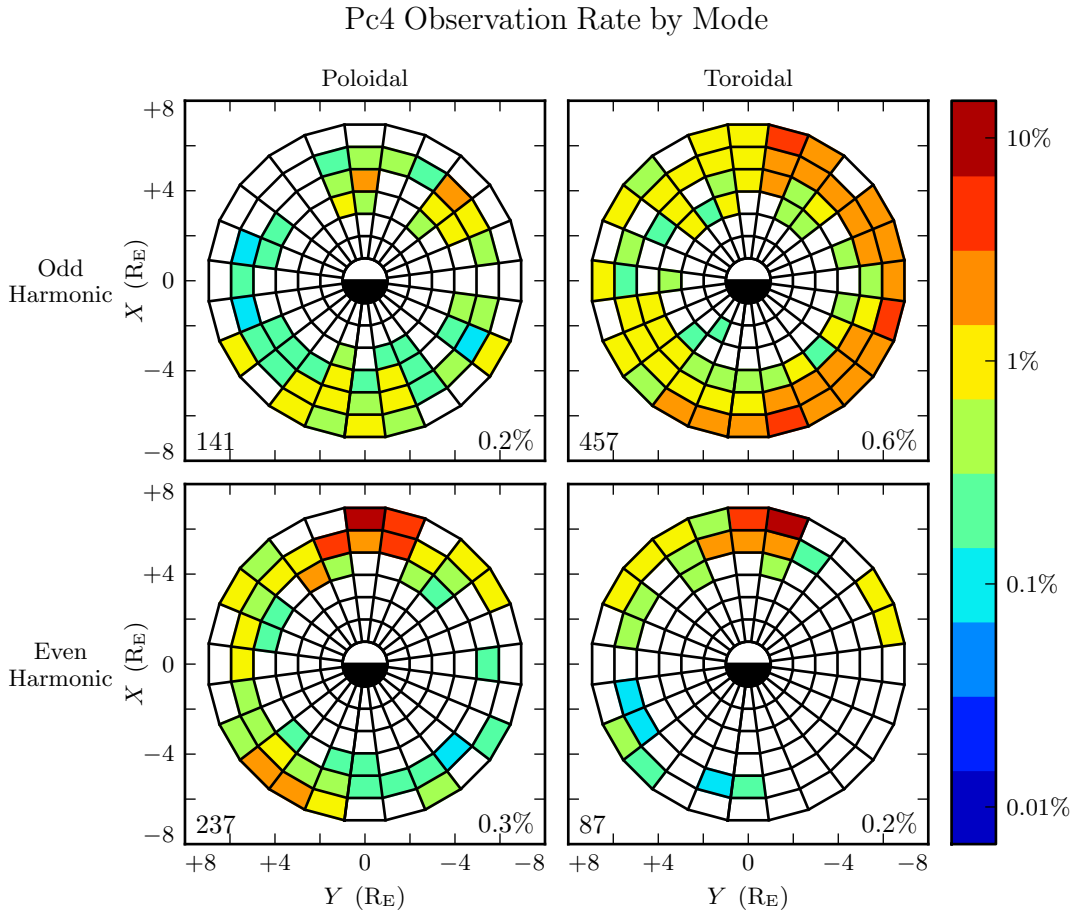


Figure 8.3: The above figure shows the spatial distribution for the same 840 events shown in Figure 8.2, partitioned by polarization and parity. The selection criteria described in Section 8.1 ensure that both properties are known for all events. Event counts are normalized by the time spent by the amount of usable data in each bin. Event counts do not sum to 840 because some events trigger on both the poloidal channel and the toroidal channel. Bins shown in white contain zero events.

### <sup>1323</sup> 8.3 Rate of Pc4 Events by Amplitude

### Amplitude Distribution of Pc4 Events by Mode

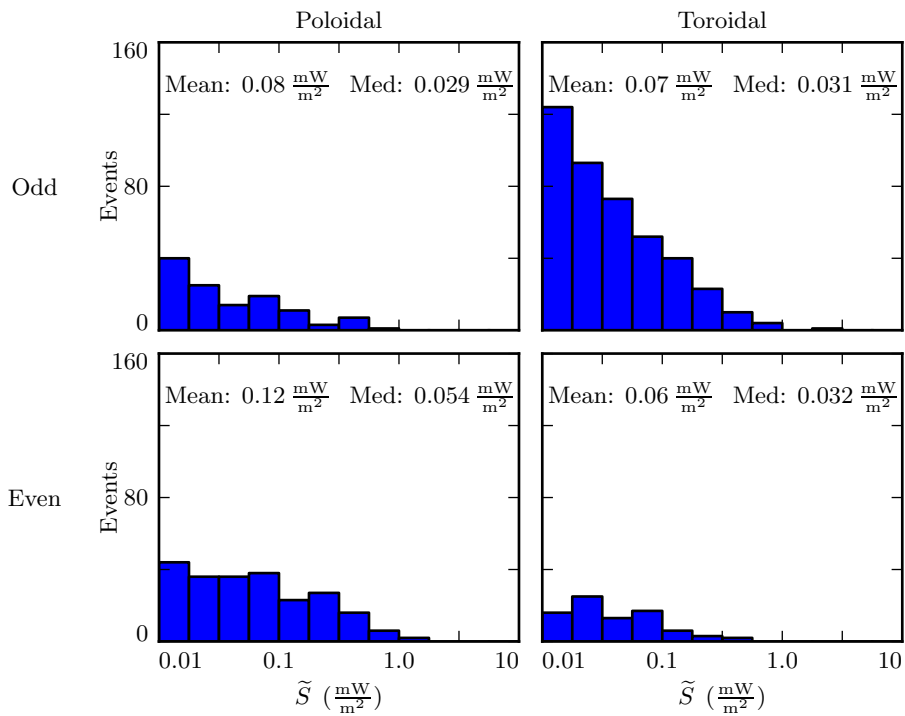


Figure 8.4: TODO: ...

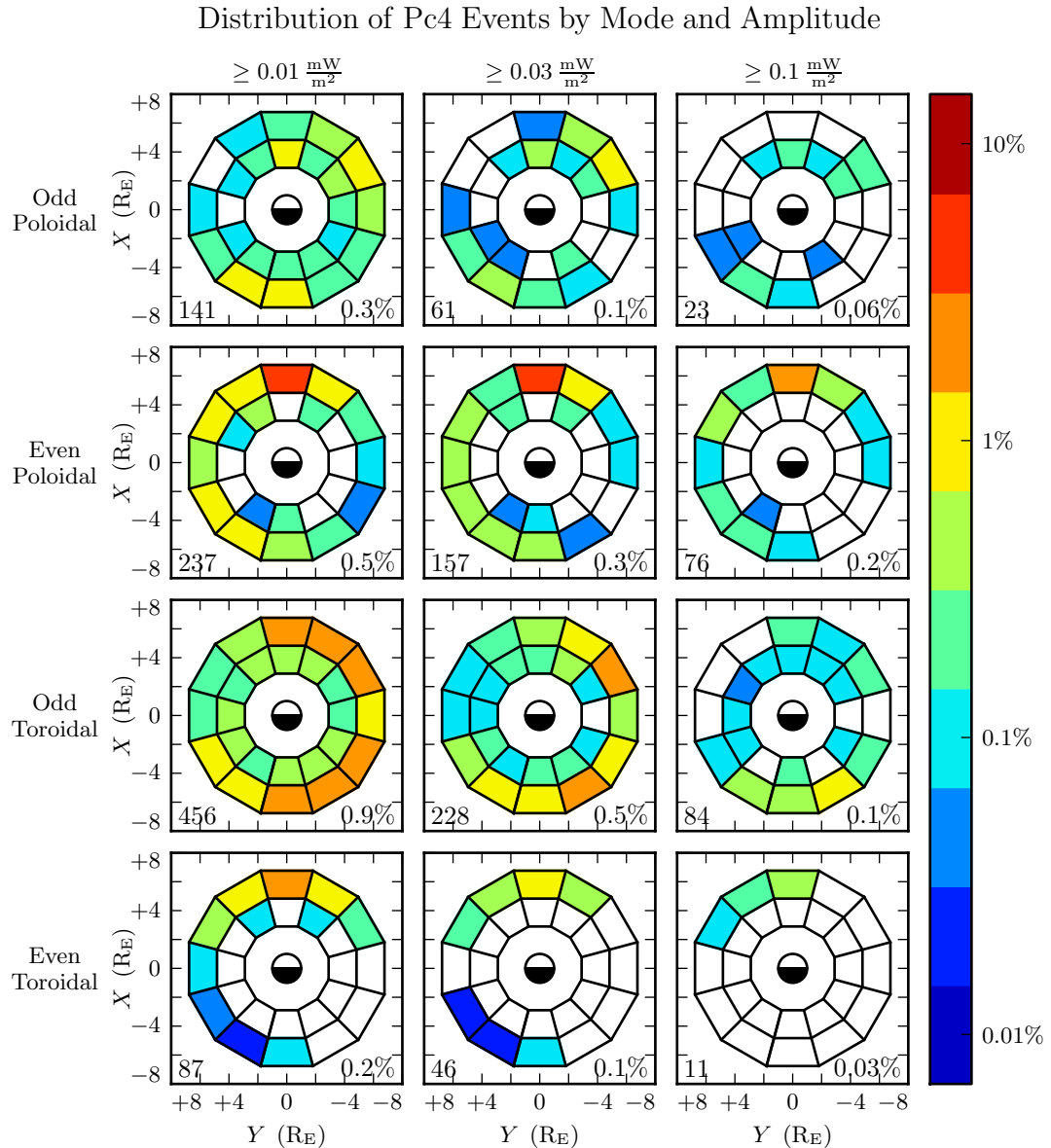


Figure 8.5: TODO: ...

<sub>1324</sub> 8.4 Rate of Pc4 Events by Frequency

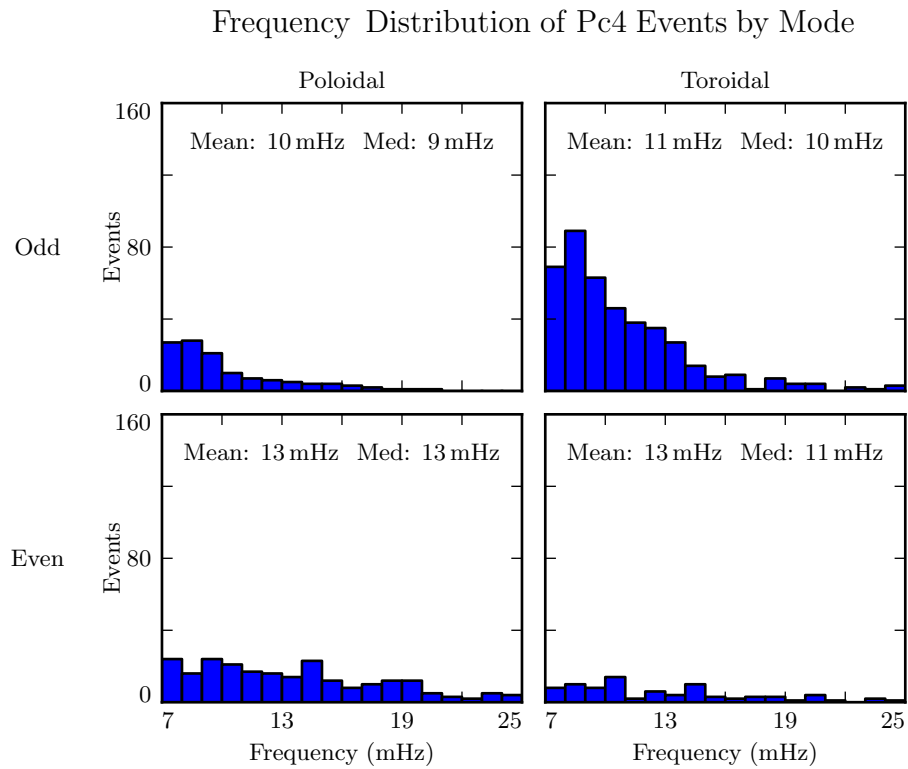


Figure 8.6: TODO: ...

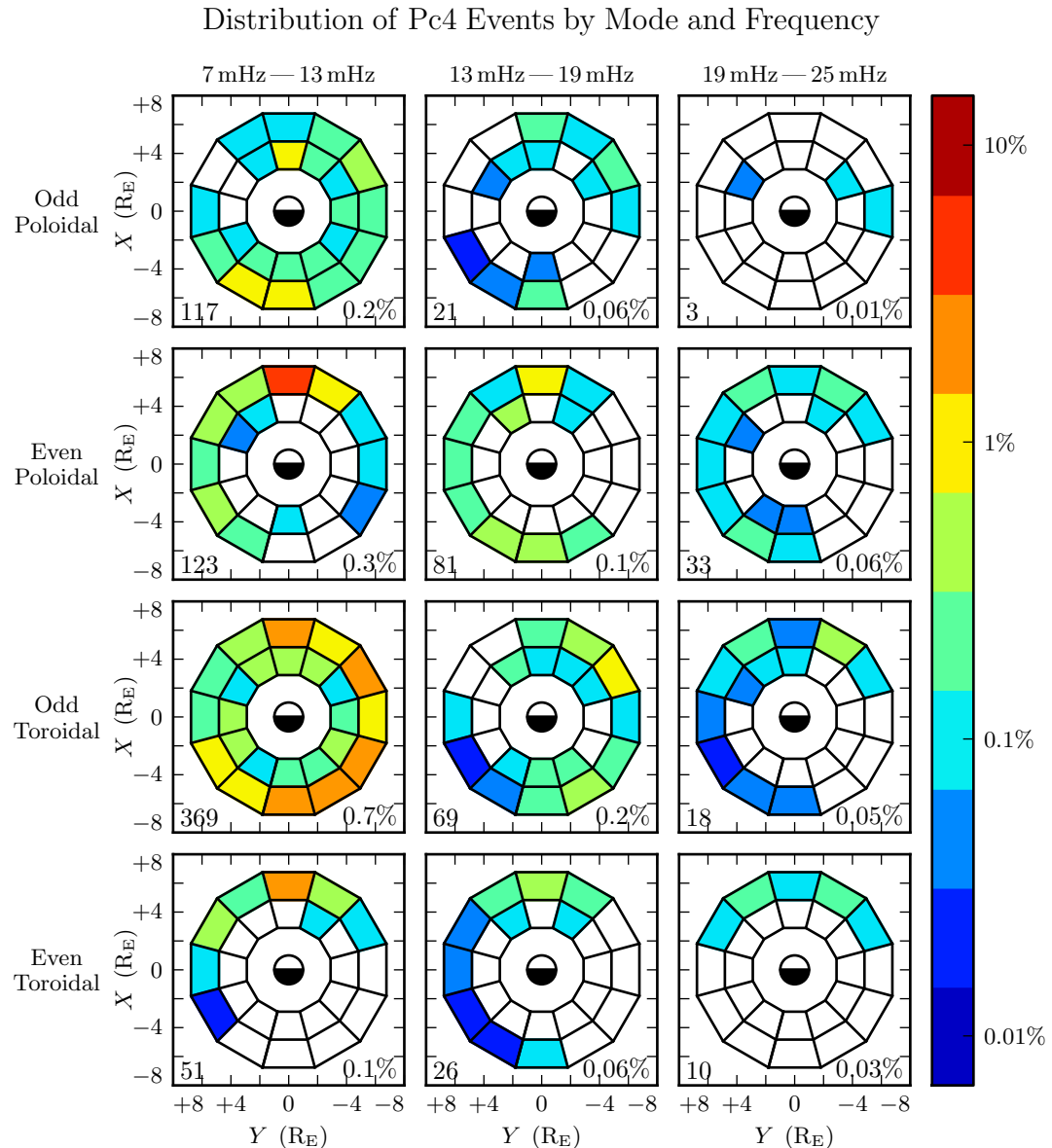


Figure 8.7: TODO: ...

## 1325 8.5 Rate of Pc4 Events by Phase

### Phase Distribution of Pc4 Events by Mode

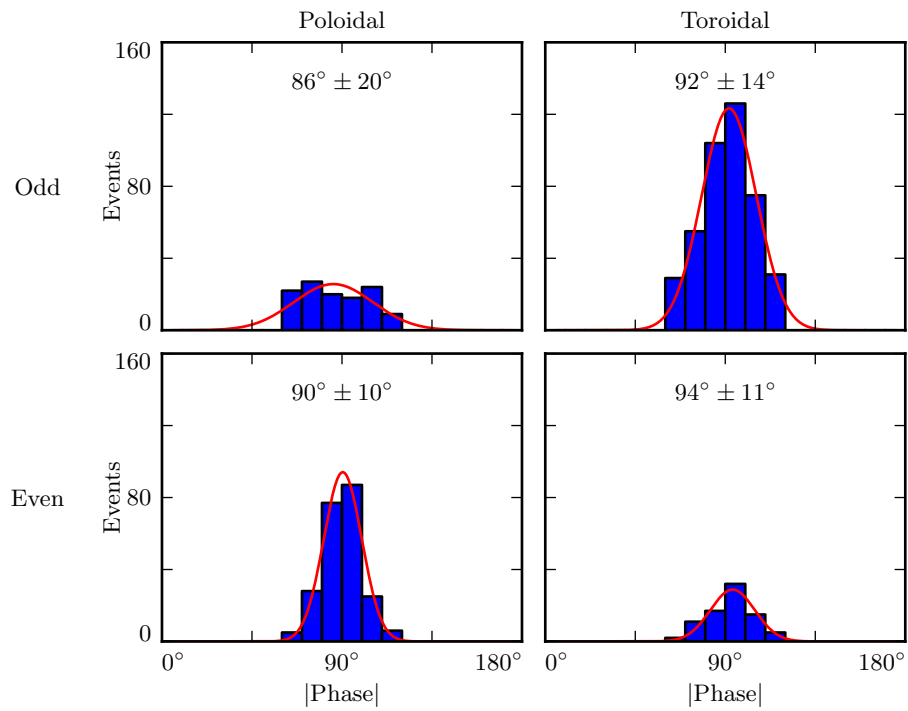


Figure 8.8: TODO: ...

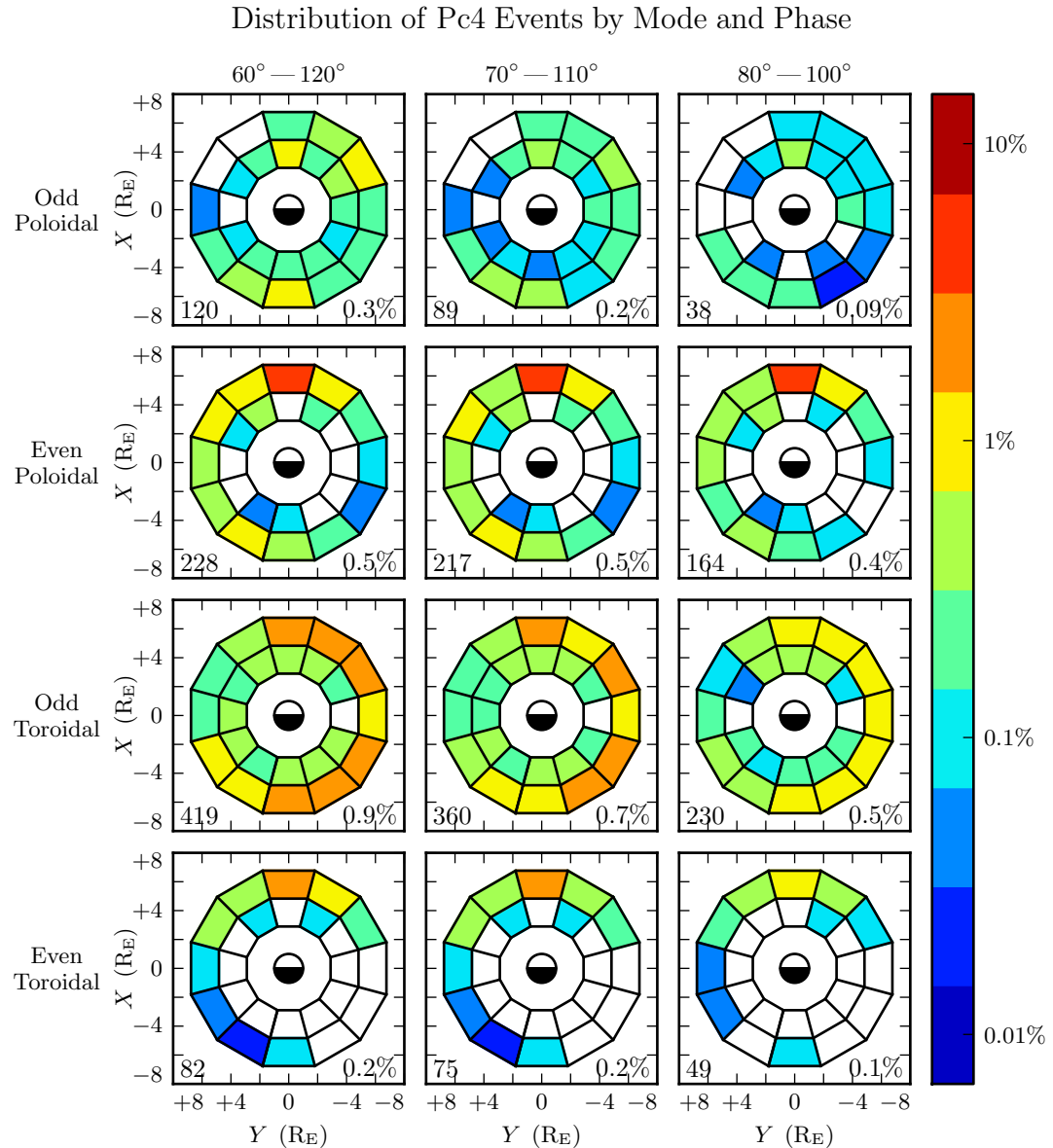


Figure 8.9: TODO: ...

## **8.6 Rate of Pc4 Events by Spectral Width**

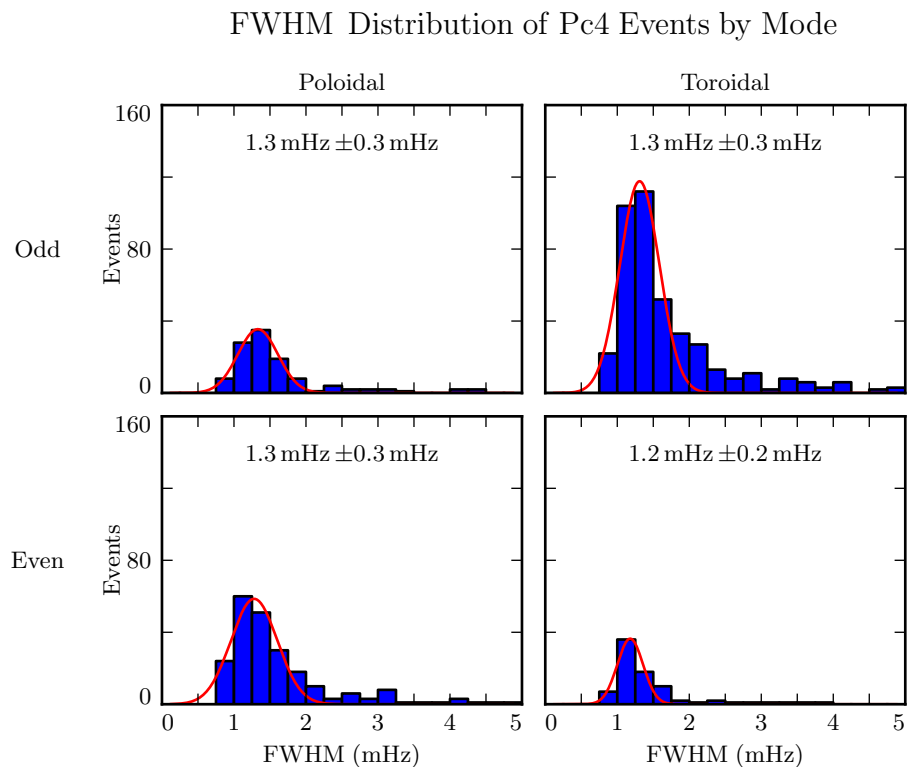


Figure 8.10: TODO: ...

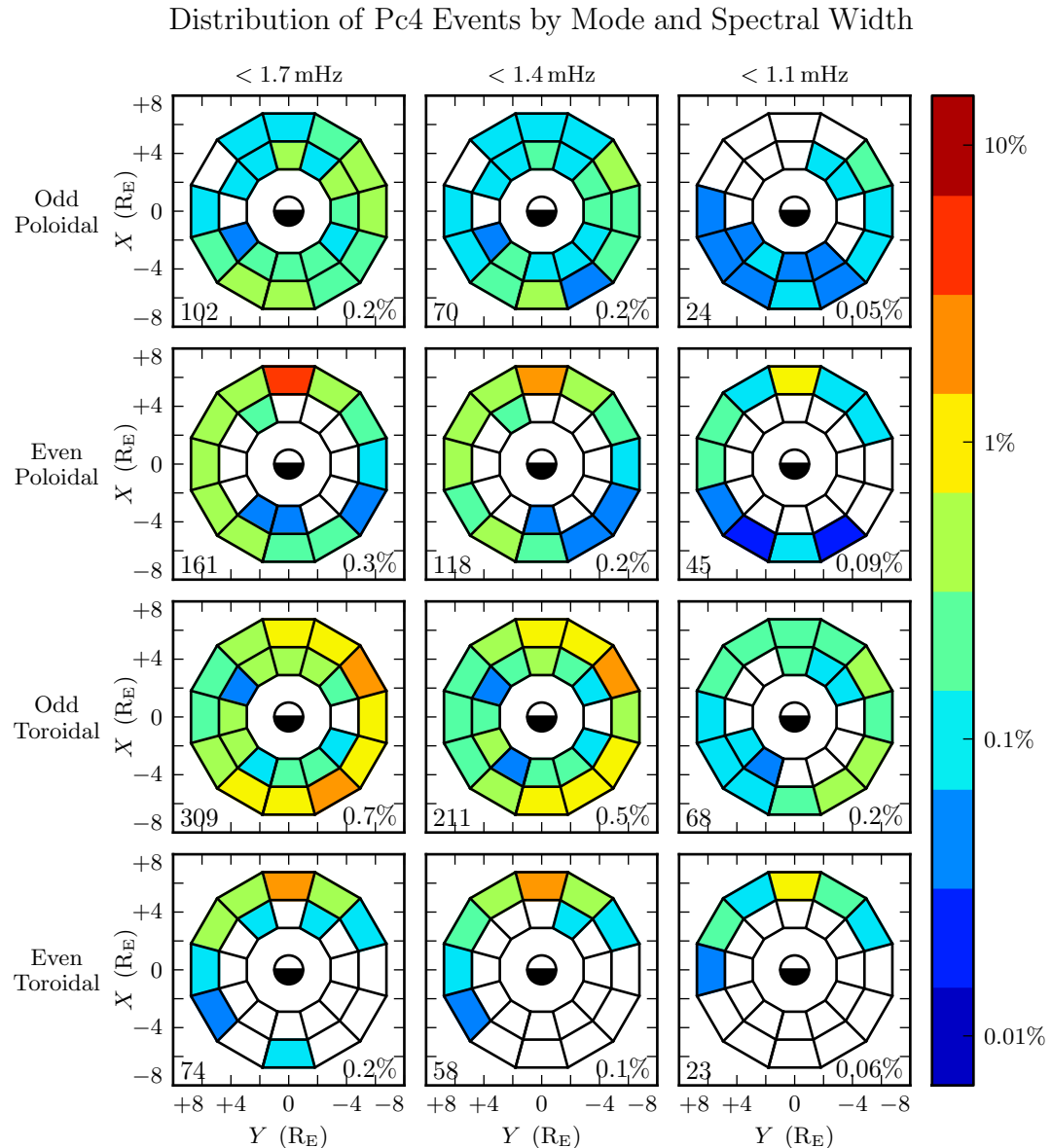


Figure 8.11: TODO: ...

## <sup>1327</sup> 8.7 Discussion

<sup>1328</sup> TODO: ...

1329 **Chapter 9**

1330 **Conclusion**

1331 **9.1 Summary of Results**

1332 TODO: Code development... Chapters 5 and 6

1333 TODO: Make the Git repository public, and link to it.

1334 TODO: Numerical results... Chapter 7

1335 TODO: Re-summarize the Discussion sections, I guess.

1336 TODO: Observational results... Chapter 8

1337 TODO: Link to the Git repository.

1338 **9.2 Future Work**

1339 TODO: Code development.

1340 Arbitrary deformation of grid. Get  $\hat{e}_i = \frac{\partial}{\partial u^i} \underline{x}$ , then  $g_{ij} = \hat{e}_i \cdot \hat{e}_j$ , then invert the metric  
1341 tensor for contravariant components.

1342 MPI. Time to compute vs time to broadcast. This might make sense for inertial length  
1343 scales.

1344 Better ionospheric profiles. Distinction between the dawn and dusk flanks. Maybe even  
1345 update the conductivity based on energy deposition — precipitation causes ionization!

1346 IRI ionosphere model. Solar illumination effects.

1347 **TODO: Numerical work.**

1348 More complicated driving. Higher harmonics, non-sinusoidal waveforms. Maybe even  
1349 drive based on events?

1350 **TODO: Analysis of RBSP data.**

1351 Basically just do everything over again, twice as well, once the probes have finished  
1352 sampling the dayside again.

# 1353 References

- 1354 [1] S.-I. Akasofu. The development of the auroral substorm. *Planetary and Space*  
1355 *Science*, 12(4):273–282, 1964.
- 1356 [2] H. Alfvén. On the cosmogony of the solar system III. *Stockholms Observatoriums*  
1357 *Annaler*, 14:9.1–9.29, 1946.
- 1358 [3] B. J. Anderson, M. J. Engebretson, S. P. Rounds, L. J. Zanetti, and T. A. Potemra.  
1359 A statistical study of Pc 3-5 pulsations observed by the AMPTE/CCE magnetic  
1360 fields experiment, 1. occurrence distributions. *J. Geophys. Res.*, 95(A7):10495,  
1361 1990.
- 1362 [4] V. Angelopoulos. The THEMIS mission. *Space Science Reviews*, 141(1-4):5–34,  
1363 2008.
- 1364 [5] K. Birkeland. Expédition norvégienne de 1899-1900 pour l'étude des aurores  
1365 boréales. *Mat. Naturvidensk. Kl.*, KI(I), 1901.
- 1366 [6] J. P. Boris. A physically motivated solution of the Alfvén problem. *NRL Memo-*  
1367 *randum Report*, 2167, 1970.
- 1368 [7] A. Brekke, T. Feder, and S. Berger. Pc4 giant pulsations recorded in Tromsø,  
1369 1929-1985. *Journal of Atmospheric and Terrestrial Physics*, 49(10):1027–1032,  
1370 1987.
- 1371 [8] C. W. Carlson, R. F. Pfaff, and J. G. Watzin. The fast auroral Snapshot (FAST)  
1372 mission. *Geophys. Res. Lett.*, 25(12):2013–2016, 1998.

- 1373 [9] A. A. Chan, M. Xia, and L. Chen. Anisotropic alfvén-balloon modes in Earth's  
 1374 magnetosphere. *J. Geophys. Res. Space Physics*, 99(A9):17351–17366, 1994.
- 1375 [10] L. Chen and A. Hasegawa. A theory of long-period magnetic pulsations: 1. steady  
 1376 state excitation of field line resonance. *J. Geophys. Res.*, 79(7):1024–1032, 1974.
- 1377 [11] L. Chen and A. Hasegawa. Kinetic theory of geomagnetic pulsations: 1. internal  
 1378 excitations by energetic particles. *J. Geophys. Res.*, 96(A2):1503, 1991.
- 1379 [12] L. Chen, R. White, C. Cheng, F. Romanelli, J. Weiland, R. Hay, J. V. Dam,  
 1380 D. Barnes, M. Rosenbluth, and S. Tsai. Theory and simulation of fishbone-type  
 1381 instabilities in beam-heated tokamaks. Technical report, 1984.
- 1382 [13] C. Z. Cheng and Q. Qian. Theory of ballooning-mirror instabilities for anisotropic  
 1383 pressure plasmas in the magnetosphere. *J. Geophys. Res.*, 99(A6):11193, 1994.
- 1384 [14] G. Chisham and D. Orr. Statistical studies of giant pulsations (pgs): Harmonic  
 1385 mode. *Planetary and Space Science*, 39(7):999–1006, 1991.
- 1386 [15] W. D. Cummings, R. J. O'Sullivan, and P. J. Coleman. Standing Alfvén waves in  
 1387 the magnetosphere. *J. Geophys. Res.*, 74(3):778–793, 1969.
- 1388 [16] L. Dai. Collisionless magnetic reconnection via Alfvén eigenmodes. *Phys. Rev.*  
 1389 *Lett.*, 102(24), 2009.
- 1390 [17] L. Dai, K. Takahashi, R. Lysak, C. Wang, J. R. Wygant, C. Kletzing, J. Bonnell,  
 1391 C. A. Cattell, C. W. Smith, R. J. MacDowall, S. Thaller, A. Breneman, X. Tang,  
 1392 X. Tao, and L. Chen. Storm time occurrence and spatial distribution of Pc4  
 1393 poloidal ULF waves in the inner magnetosphere: A Van Allen Probes statistical  
 1394 study. *J. Geophys. Res. Space Physics*, 120:4748–4762, 2015.
- 1395 [18] L. Dai, K. Takahashi, J. R. Wygant, L. Chen, J. Bonnell, C. A. Cattell, S. Thaller,  
 1396 C. Kletzing, C. W. Smith, R. J. MacDowall, D. N. Baker, J. B. Blake, J. Fennell,  
 1397 S. Claudepierre, H. O. Funsten, G. D. Reeves, and H. E. Spence. Excitation of  
 1398 poloidal standing Alfvén waves through drift resonance wave-particle interaction.  
 1399 *Geophys. Res. Lett.*, 40:4127–4132, 2013.

- 1400 [19] A. W. Degeling, R. Rankin, and Q.-G. Zong. Modeling radiation belt electron  
1401 acceleration by ULF fast mode waves, launched by solar wind dynamic pressure  
1402 fluctuations. *J. Geophys. Res. Space Physics*, 119(11):8916–8928, 2014.
- 1403 [20] W. D. D’haeseleer, W. N. G. H. J. D. Callen, and J. L. Shohet. *Flux Coordinates*  
1404 and *Magnetic Field Structure*. Springer-Verlag, New York, 1991.
- 1405 [21] J. W. Dungey. The attenuation of Alfvén waves. *J. Geophys. Res.*, 59(3):323–328,  
1406 1954.
- 1407 [22] J. W. Dungey. Interplanetary magnetic field and the auroral zones. *Phys. Rev.*  
1408 *Lett.*, 6(2):47–48, 1961.
- 1409 [23] A. Einstein. Die grundlage der allgemeinen relativitätstheorie. *Ann. Phys.*,  
1410 354:769–822, 1916.
- 1411 [24] S. R. Elkington, M. K. Hudson, and A. A. Chan. Acceleration of relativistic  
1412 electrons via drift-resonant interaction with toroidal-mode Pc-5 ULF oscillations.  
1413 *Geophys. Res. Lett.*, 26(21):3273–3276, 1999.
- 1414 [25] M. J. Engebretson, D. L. Murr, K. N. Erickson, R. J. Strangeway, D. M. Klumpar,  
1415 S. A. Fuselier, L. J. Zanetti, and T. A. Potemra. The spatial extent of radial  
1416 magnetic pulsation events observed in the dayside near synchronous orbit. *J.*  
1417 *Geophys. Res.*, 97(A9):13741, 1992.
- 1418 [26] P. T. I. Eriksson, L. G. Blomberg, A. D. M. Walker, and K.-H. Glassmeier. Poloidal  
1419 ULF oscillations in the dayside magnetosphere: a Cluster study. *Ann. Geophys.*,  
1420 23(7):2679–2686, 2005.
- 1421 [27] S. Fujita and T. Tamao. Duct propagation of hydromagnetic waves in the upper  
1422 ionosphere, 1, electromagnetic field disturbances in high latitudes associated with  
1423 localized incidence of a shear Alfvén wave. *J. Geophys. Res.*, 93(A12):14665, 1988.
- 1424 [28] K.-H. Glassmeier. Magnetometer array observations of a giant pulsation event. *J.*  
1425 *Geophys.*, 48:127–138, 1980.
- 1426 [29] K.-H. Glassmeier. On the influence of ionospheres with non-uniform conductivity  
1427 distribution on hydromagnetic waves. *J. Geophys.*, 54(2):125–137, 1984.

- 1428 [30] K.-H. Glassmeier, S. Buchert, U. Motschmann, A. Korth, and A. Pedersen. Concerning the generation of geomagnetic giant pulsations by drift-bounce resonance  
1429 ring current instabilities. *Ann. Geophysicae*, 17:338–350, 1999.
- 1431 [31] K.-H. Glassmeier, D. Klimushkin, C. Othmer, and P. Mager. ULF waves at  
1432 mercury: Earth, the giants, and their little brother compared. *Advances in Space  
1433 Research*, 33(11):1875–1883, 2004.
- 1434 [32] C. Goertz. Kinetic alfvén waves on auroral field lines. *Planetary and Space Science*,  
1435 32(11):1387–1392, 1984.
- 1436 [33] C. K. Goertz and R. W. Boswell. Magnetosphere-ionosphere coupling. *J. Geophys.  
1437 Res.*, 84(A12):7239, 1979.
- 1438 [34] C. A. Green. Giant pulsations in the plasmasphere. *Planetary and Space Science*,  
1439 33(10):1155–1168, 1985.
- 1440 [35] J. L. Green and S. Boardsen. Duration and extent of the great auroral storm of  
1441 1859. *Advances in Space Research*, 38(2):130–135, 2006.
- 1442 [36] C. Greifinger and P. S. Greifinger. Theory of hydromagnetic propagation in the  
1443 ionospheric waveguide. *J. Geophys. Res.*, 73(23):7473–7490, 1968.
- 1444 [37] B. C. Hall. *Lie Groups, Lie Algebras, and Representations*. Graduate Texts in  
1445 Mathematics. Springer, New York, second edition, 2015.
- 1446 [38] Y. X. Hao, Q.-G. Zong, Y. F. Wang, X.-Z. Zhou, H. Zhang, S. Y. Fu, Z. Y.  
1447 Pu, H. E. Spence, J. B. Blake, J. Bonnell, J. R. Wygant, and C. A. Kletzing.  
1448 Interactions of energetic electrons with ULF waves triggered by interplanetary  
1449 shock: Van allen probes observations in the magnetotail. *J. Geophys. Res. Space  
1450 Physics*, 119(10):8262–8273, 2014.
- 1451 [39] L. Harang. *Pulsations in the terrestrial magnetic records at high latitude stations*.  
1452 Grondahl, 1942.
- 1453 [40] O. Hillebrand, J. Muench, and R. L. McPherron. Ground-satellite correlative  
1454 study of a giant pulsation event. *Journal of Geophysics Zeitschrift Geophysik*,  
1455 51:129–140, 1982.

- 1456 [41] W. J. Hughes. The effect of the atmosphere and ionosphere on long period mag-  
1457 netospheric micropulsations. *Planet. Space Sci.*, 22:1157–1172, 1974.
- 1458 [42] W. J. Hughes. Magnetospheric ULF waves: A tutorial with a historical perspec-  
1459 tive. In M. J. Engebretson, K. Takahashi, and M. Scholer, editors, *Solar Wind*  
1460 *Sources of Magnetospheric Ultra-Low-Frequency Waves*, volume 81 of *Geophys.*  
1461 *Monogr.*, pages 1–12. American Geophysical Union, Washington, DC, 1994.
- 1462 [43] W. J. Hughes and D. J. Southwood. The screening of micropulsation signals by  
1463 the atmosphere and ionosphere. *J. Geophys. Res.*, 81(19):3234–3240, 1976.
- 1464 [44] W. J. Hughes, D. J. Southwood, B. Mauk, R. L. McPherron, and J. N. Barfield.  
1465 Alfvén waves generated by an inverted plasma energy distribution. *Nature*,  
1466 275(5675):43–45, 1978.
- 1467 [45] J. A. Jacobs, Y. Kato, S. Matsushita, and V. A. Troitskaya. Classification of  
1468 geomagnetic micropulsations. *J. Geophys. Res.*, 69(1):180–181, 1964.
- 1469 [46] T. Karlsson and G. T. Marklund. A statistical study of intense low-altitude electric  
1470 fields observed by freja. *Geophys. Res. Lett.*, 23(9):1005–1008, 1996.
- 1471 [47] Y. Kato and T. Tsutomu. Hydromagnetic oscillations in a conducting medium  
1472 with hall couduct-ivity under the uniform magnetic field. *Science reports of the*  
1473 *Tohoku University. Ser. 5, Geophysics*, 7(3):147–164, 1956.
- 1474 [48] M. C. Kelley. *The Earth’s Ionosphere*. Academic Press, San Diego, second edition,  
1475 1989.
- 1476 [49] R. L. Kessel. Solar wind excitation of pc5 fluctuations in the magnetosphere and  
1477 on the ground. *J. Geophys. Res.*, 113(A4), 2008.
- 1478 [50] D. Y. Klimushkin, P. N. Mager, and K.-H. Glassmeier. Toroidal and poloidal  
1479 Alfvén waves with arbitrary azimuthal wavenumbers in a finite pressure plasma  
1480 in the earth’s magnetosphere. *Annales Geophysicae*, 22(1):267–287, 2004.
- 1481 [51] S. Kokubun. Observations of Pc pulsations in the magnetosphere: Satellite-ground  
1482 correlation. *J. Geomagn. Geoelec*, 32(Supplement2):SII17–SII39, 1980.

- 1483 [52] S. Kokubun, K. N. Erickson, T. A. Fritz, and R. L. McPherron. Local time asymmetry of Pc 4-5 pulsations and associated particle modulations at synchronous  
1484 orbit. *J. Geophys. Res.*, 94(A6):6607–6625, 1989.
- 1485
- 1486 [53] D.-H. Lee and K. Kim. Compressional MHD waves in the magnetosphere: A new  
1487 approach. *J. Geophys. Res.*, 104(A6):12379–12385, 1999.
- 1488
- 1489 [54] A. S. Leonovich and V. A. Mazur. Structure of magnetosonic eigenoscillations of  
an axisymmetric magnetosphere. *J. Geophys. Res.*, 105(A12):27707–27715, 2000.
- 1490
- 1491 [55] W. Liu, J. B. Cao, X. Li, T. E. Sarris, Q.-G. Zong, M. Hartinger, K. Takahashi,  
1492 H. Zhang, Q. Q. Shi, and V. Angelopoulos. Poloidal ULF wave observed in the  
plasmasphere boundary layer. *J. Geophys. Res. Space Physics*, 118(7):4298–4307,  
1493 2013.
- 1494
- 1495 [56] W. Liu, T. E. Sarris, X. Li, S. R. Elkington, R. Ergun, V. Angelopoulos, J. Bonnell,  
1496 and K. H. Glassmeier. Electric and magnetic field observations of Pc4 and Pc5  
1497 pulsations in the inner magnetosphere: A statistical study. *J. Geophys. Res.*,  
114(A12), 2009.
- 1498
- 1499 [57] W. Liu, T. E. Sarris, X. Li, Q.-G. Zong, R. Ergun, V. Angelopoulos, and K. H.  
1500 Glassmeier. Spatial structure and temporal evolution of a dayside poloidal ULF  
*Geophys. Res. Lett.*, 38(19), 2011.
- 1501
- 1502 [58] R. L. Lysak. Magnetosphere-ionosphere coupling by Alfvén waves at midlatitudes.  
*J. Geophys. Res.*, 109, 2004.
- 1503
- 1504 [59] R. L. Lysak and D. hun Lee. Response of the dipole magnetosphere to pressure  
pulses. *Geophys. Res. Lett.*, 19(9):937–940, 1992.
- 1505
- 1506 [60] R. L. Lysak and Y. Song. A three-dimensional model of the propagation of Alfvén  
1507 waves through the auroral ionosphere: first results. *Adv. Space Res.*, 28:813–822,  
2001.
- 1508
- 1509 [61] R. L. Lysak, C. L. Waters, and M. D. Sciffer. Modeling of the ionospheric Alfvén  
resonator in dipolar geometry. *J. Geophys. Res. Space Physics*, 118, 2013.

- 1510 [62] P. N. Mager and D. Y. Klimushkin. Giant pulsations as modes of a transverse  
1511 Alfvénic resonator on the plasmapause. *Earth, Planets and Space*, 65(5):397–409,  
1512 2013.
- 1513 [63] I. R. Mann, E. A. Lee, S. G. Claudepierre, J. F. Fennell, A. Degeling, I. J. Rae,  
1514 D. N. Baker, G. D. Reeves, H. E. Spence, L. G. Ozeke, R. Rankin, D. K. Milling,  
1515 A. Kale, R. H. W. Friedel, and F. Honary. Discovery of the action of a geophysical  
1516 synchrotron in the Earth’s Van Allen radiation belts. *Nature Communications*, 4,  
1517 2013.
- 1518 [64] I. R. Mann and A. N. Wright. Finite lifetimes of ideal poloidal Alfvén waves. *J.  
1519 Geophys. Res.*, 100:23677–23686, 1995.
- 1520 [65] I. R. Mann, A. N. Wright, and A. W. Hood. Multiple-timescales analysis of ideal  
1521 poloidal Alfvén waves. *J. Geophys. Res.*, 102(A2):2381–2390, 1997.
- 1522 [66] T. Maynard, N. Smith, S. Gonzalez, et al. Solar storm risk to the North American  
1523 electric grid. 2013.
- 1524 [67] K. McGuire, R. Goldston, M. Bell, M. Bitter, K. Bol, K. Brau, D. Buchenauer,  
1525 T. Crowley, S. Davis, F. Dylla, H. Eubank, H. Fishman, R. Fonck, B. Grek,  
1526 R. Grimm, R. Hawryluk, H. Hsuan, R. Hulse, R. Izzo, R. Kaita, S. Kaye, H. Kugel,  
1527 D. Johnson, J. Manickam, D. Manos, D. Mansfield, E. Mazzucato, R. McCann,  
1528 D. McCune, D. Monticello, R. Motley, D. Mueller, K. Oasa, M. Okabayashi,  
1529 K. Owens, W. Park, M. Reusch, N. Sauthoff, G. Schmidt, S. Sesnic, J. Strachan,  
1530 C. Surko, R. Slusher, H. Takahashi, F. Tenney, P. Thomas, H. Towner, J. Valley,  
1531 and R. White. Study of high-beta magnetohydrodynamic modes and fast-ion  
1532 losses in PDX. *Phys. Rev. Lett.*, 50(12):891–895, 1983.
- 1533 [68] R. L. McPherron. The role of substorms in the generation of magnetic storms.  
1534 *Washington DC American Geophysical Union Geophysical Monograph Series*,  
1535 98:131–147, 1997.
- 1536 [69] R. L. McPherron, G. K. Parks, D. S. Colburn, and M. D. Montgomery. Satellite  
1537 studies of magnetospheric substorms on august 15, 1968: 2. solar wind and outer  
1538 magnetosphere. *J. Geophys. Res.*, 78(16):3054–3061, 1973.

- 1539 [70] T. Motoba, K. Takahashi, J. V. Rodriguez, and C. T. Russell. Giant pulsations on  
1540 the afternoonside: Geostationary satellite and ground observations. *J. Geophys.*  
1541 *Res. Space Physics*, 120:8350–8367, 2015.
- 1542 [71] NASA. Coordinated data analysis (workshop) web.
- 1543 [72] NASA. Near miss: The solar superstorm of july 2012.
- 1544 [73] M. Nicolet. The collision frequency of electrons in the ionosphere. *Journal of*  
1545 *Atmospheric and Terrestrial Physics*, 3(4):200–211, 1953.
- 1546 [74] L. G. Ozeke and I. R. Mann. Energization of radiation belt electrons by ring  
1547 current ion driven ULF waves. *J. Geophys. Res.*, 113(A2), 2008.
- 1548 [75] E. M. Poulter, W. Allan, E. Nielsen, and K.-H. Glassmeier. Stare radar observa-  
1549 tions of a PG pulsation. *J. Geophys. Res.*, 88(A7):5668, 1983.
- 1550 [76] J. A. Proehl, W. Lotko, I. Kouznetsov, and S. D. Geimer. Ultralow-frequency  
1551 magnetohydrodynamics in boundary-constrained geomagnetic flux coordinates.  
1552 *J. Geophys. Res.*, 107(A9):1225, 2002.
- 1553 [77] H. R. Radoski. A note on oscillating field lines. *J. Geophys. Res.*, 72(1), 1967.
- 1554 [78] H. R. Radoski. A theory of latitude dependent geomagnetic micropulsations: The  
1555 asymptotic fields. *J. Geophys. Res.*, 79, 1974.
- 1556 [79] R. Rankin, J. C. Samson, and V. T. Tikhonchuk. Parallel electric fields in dis-  
1557 persive shear alfvén waves in the dipolar magnetosphere. *Geophys. Res. Lett.*,  
1558 26(24):3601–3604, 1999.
- 1559 [80] B. Rolf. Giant micropulsations at abisko. *J. Geophys. Res.*, 36(1):9, 1931.
- 1560 [81] G. Rostoker, H.-L. Lam, and J. V. Olson. PC 4 giant pulsations in the morning  
1561 sector. *J. Geophys. Res.*, 84(A9):5153, 1979.
- 1562 [82] J. C. Samson, L. L. Cogger, and Q. Pao. Observations of field line resonances,  
1563 auroral arcs, and auroral vortex structures. *J. Geophys. Res.*, 101(A8):17373–  
1564 17383, 1996.

- 1565 [83] H. J. Singer, W. J. Hughes, and C. T. Russell. Standing hydromagnetic waves  
1566 observed by ISEE 1 and 2: Radial extent and harmonic. *J. Geophys. Res.*,  
1567 87(A5):3519, 1982.
- 1568 [84] D. J. Southwood. Some features of field line resonances in the magnetosphere.  
1569 *Planetary and Space Science*, 22(3):483–491, 1974.
- 1570 [85] D. J. Southwood. A general approach to low-frequency instability in the ring  
1571 current plasma. *J. Geophys. Res.*, 81(19):3340–3348, 1976.
- 1572 [86] J. Stratton and N. J. Fox. Radiation belt storm probes (RBSP) mission overview.  
1573 In *2012 IEEE Aerospace Conference*. Institute of Electrical & Electronics Engi-  
1574 neers (IEEE), 2012.
- 1575 [87] E. Sucksdorff. Giant pulsations recorded at sodankyl during 19141938. *Terrestrial*  
1576 *Magnetism and Atmospheric Electricity*, 44(2):157–170, 1939.
- 1577 [88] K. Takahashi, J. Bonnell, K.-H. Glassmeier, V. Angelopoulos, H. J. Singer, P. J.  
1578 Chi, R. E. Denton, Y. Nishimura, D.-H. Lee, M. Nosé, and W. Liu. Multipoint  
1579 observation of fast mode waves trapped in the dayside plasmasphere. *J. Geophys.*  
1580 *Res.*, 115(A12), 2010.
- 1581 [89] K. Takahashi, K.-H. Glassmeier, V. Angelopoulos, J. Bonnell, Y. Nishimura, H. J.  
1582 Singer, and C. T. Russell. Multisatellite observations of a giant pulsation event.  
1583 *J. Geophys. Res.*, 116:A11223, 2011.
- 1584 [90] K. Takahashi, M. D. Hartinger, V. Angelopoulos, K.-H. Glassmeier, and H. J.  
1585 Singer. Multispacecraft observations of fundamental poloidal waves without  
1586 ground magnetic signatures. *J. Geophys. Res. Space Physics*, 118:4319–4334, 2013.
- 1587 [91] K. Takahashi, R. W. McEntire, A. T. Y. Lui, and T. A. Potemra. Ion flux oscilla-  
1588 tions associated with a radially polarized transverse Pc 5 magnetic pulsation. *J.*  
1589 *Geophys. Res.*, 95(A4):3717, 1990.
- 1590 [92] K. Takahashi, N. Sato, J. Warnecke, H. Lühr, H. E. Spence, and Y. Tonegawa.  
1591 On the standing wave mode of giant pulsations. *J. Geophys. Res. Space Physics*,  
1592 97(A7):10717–10732, 1992.

- 1593 [93] B. J. Thompson and R. L. Lysak. Electron acceleration by inertial alfvén waves.  
1594      *J. Geophys. Res.*, 101(A3):5359–5369, 1996.
- 1595 [94] S. M. Thompson and M. G. Kivelson. New evidence for the origin of giant pulsations.  
1596      *J. Geophys. Res.*, 106(A10):21237–21253, 2001.
- 1597 [95] V. T. Tikhonchuk and R. Rankin. Electron kinetic effects in standing shear alfveén  
1598      waves in the dipolar magnetosphere. *Physics of Plasmas*, 7(6):2630, 2000.
- 1599 [96] B. T. Tsurutani, W. D. Gonzalez, G. S. Lakhina, and S. Alex. The extreme  
1600      magnetic storm of 12 september 1859. *Journal of Geophysical Research: Space  
1601      Physics*, 108(A7), 2003. 1268.
- 1602 [97] A. Y. Ukhorskiy. Impact of toroidal ULF waves on the outer radiation belt elec-  
1603      trons. *J. Geophys. Res.*, 110(A10), 2005.
- 1604 [98] J. Veldkamp. A giant geomagnetic pulsation. *Journal of Atmospheric and Ter-  
1605     restrial Physics*, 17(4):320–324, 1960.
- 1606 [99] J. A. Wanliss and K. M. Showalter. High-resolution global storm index: Dst versus  
1607      sym-h. *Journal of Geophysical Research: Space Physics*, 111(A2):n/a–n/a, 2006.  
1608      A02202.
- 1609 [100] C. L. Waters, R. L. Lysak, and M. D. Sciffer. On the coupling of fast and shear  
1610      Alfvén wave modes by the ionospheric Hall conductance. *Earth Planets Space*,  
1611      65:385–396, 2013.
- 1612 [101] C. L. Waters and M. D. Sciffer. Field line resonant frequencies and ionospheric  
1613      conductance: Results from a 2-d MHD model. *J. Geophys. Res.*, 113(A5), 2008.
- 1614 [102] D. M. Wright and T. K. Yeoman. High-latitude HF doppler observations of ULF  
1615      waves: 2. waves with small spatial scale sizes. *Ann. Geophys.*, 17(7):868–876,  
1616      1999.
- 1617 [103] J. R. Wygant, A. Keiling, C. A. Cattell, R. L. Lysak, M. Temerin, F. S. Mozer,  
1618      C. A. Kletzing, J. D. Scudder, V. Streltsov, W. Lotko, and C. T. Russell. Evidence  
1619      for kinetic alfvn waves and parallel electron energization at 46 re altitudes in the

- 1620 plasma sheet boundary layer. *Journal of Geophysical Research: Space Physics*,  
1621 107(A8):SMP 24–1–SMP 24–15, 2002.
- 1622 [104] B. Yang, Q.-G. Zong, Y. F. Wang, S. Y. Fu, P. Song, H. S. Fu, A. Korth, T. Tian,  
1623 and H. Reme. Cluster observations of simultaneous resonant interactions of ULF  
1624 waves with energetic electrons and thermal ion species in the inner magnetosphere.  
1625 *J. Geophys. Res.*, 115(A2), 2010.
- 1626 [105] K. Yee. Numerical solution of initial boundary value problems involving maxwell's  
1627 equations in isotropic media. *IEEE Trans. Antennas Propagat.*, 14(3), 1966.
- 1628 [106] T. K. Yeoman and D. M. Wright. ULF waves with drift resonance and drift-bounce  
1629 resonance energy sources as observed in artificially-induced HF radar backscatter.  
1630 *Ann. Geophys.*, 19(2):159–170, 2001.
- 1631 [107] Q.-G. Zong, X.-Z. Zhou, X. Li, P. Song, S. Y. Fu, D. N. Baker, Z. Y. Pu, T. A.  
1632 Fritz, P. Daly, A. Balogh, and H. Réme. Ultralow frequency modulation of ener-  
1633 getic particles in the dayside magnetosphere. *Geophys. Res. Lett.*, 34(12), 2007.
- 1634 [108] Q.-G. Zong, X.-Z. Zhou, Y. F. Wang, X. Li, P. Song, D. N. Baker, T. A. Fritz,  
1635 P. W. Daly, M. Dunlop, and A. Pedersen. Energetic electron response to ULF  
1636 waves induced by interplanetary shocks in the outer radiation belt. *J. Geophys.  
1637 Res.*, 114(A10), 2009.